CRACK PROPAGATION IN QUASICRYSTALS AT DIFFERENT TEMPERATURES

Von der Fakultät Physik der Universität Stuttgart
zur Erlangung der Würde eines
Doktors der Naturwissenschaften (Dr. rer. nat.)
genehmigte Abhandlung

Vorgelegt von

Marco Claudio Pio Brunelli

aus Busto Arsizio (Italien)

Haupberichter: Prof. Dr. H.-R. Trebin
Mitberichter: Prof. Dr. H. J. Herrmann

Tag der mündlichen Prüfung: 18.12.2000

Institut für Theoretische und Angewandte Physik
Universität Stuttgart
2001

Contents

List of symbols

F	X-rays signal amplitude
$\rho(x)$	Dirac delta function
$\boldsymbol{\sigma}$	stress tensor
$\boldsymbol{\epsilon}$	strain tensor
$\mathbf{u}$	displacement field
λ, μ	isotropic elastic constants
K	stress intensity factor
$\mathbf{b}$	Burger's vector
ν	Poisson's module
γ	surface energy
H	Hamiltonian function
T	temperature
Q	heat
W	work
ω_E	Einstein frequency
S	entropy
A	free energy
V	potential function
m	mass
E	elastic energy

Abstract

Molecular dynamics of crack propagation in a quasicrystalline binary system derived from a Tübingen triangle tiling has been studied at different temperatures. An original model for the simulation of crack dynamics at constant temperature is proposed in Chapter 6, In Chapter 7 are reported original free energy calculations used to compute the surface energies, the elastic constants and the critical displacements involved in crack propagation. Simulations of fracture propagation at different temperatures have been performed in a sample of many atoms (74210). For each temperature, crack propagation has been investigated in detail at different loads, and the results of this study have been collected in Chapter 8. The influence of dislocation emission on crack propagation represents one of the crucial topics in the field which are to be tackled. In Chapter 8 by means of numerical elastic estimates based on the results of Chapter 7, for the first time an explanation of the mechanisms of dislocation emission and crack propagation in the range of low loads and low temperatures is being proposed. There are features of the crack propagation simulations collected in this chapter which qualitatively reproduce some of the characteristics of experimentally observed crack propagation in a three-dimensional quasicrystal.

Zusammenfassung

Diese Arbeit beschäftigt sich mit temperaturabhängigen Molekulardynamik-Simulationen der Rissausbreitung in einem idealen zwei dimensionalen Quasikristall.

Nach der Einleitung, werden im zweiten Kapitel die physikalischen Eigenschaften und die mathematische Modellierung eines Quasikristalls geschildert.

Im dritten und vierten Kapitel werden die theoretischen Grundlagen für die Elastizität des Bruches bzw. der statischen Mechanik erläutert.

Das fünfte Kapitel beschreibt das Wechselwirkungspotential, das in den Molekulardynamik-Simulationen verwendet wird. Das sechste Kapitel erklärt das Modell der Rissausbreitung mit Temperatur, das in den Simulationen angewandt wird.

Das siebte Kapitel enthält die Ergebnisse der Gleichgewichtsimulationen. Das achte bespricht die Ergebnisse der Rissausbreitungsimulationen, bevor im neunten die Arbeit zusammengefasst wird.

Modellsystem

Quasikristalle sind Festkörper mit einer wohldefinierten Anordnung der Atome, die sich aber nicht wie bei konventionellen Kristallen periodisch wiederholt. Sie kann beschrieben werden als Überlagerung von mehreren Massedichtewellen, deren räumliche Frequenzen in inkommensurablem Verhältnis zueinander stehen.

Den Quasikristall, in dem die Molekulardynamik-Simulationen durchgeführt werden, erhält man aus der Dekoration des Tübinger Dreiecksmusters mit zwei Sorten von Atomen, großen und kleinen. Das erzeugte binäre System ist in Abbildung 1 gezeigt. In diesem binären System sind einige große Atome erkennbar, die zehn kleine Atome um sich haben. Diese Struktur, die sich im System quasiperiodisch wiederholt, nennt man “Cluster”. Da ein Cluster eine

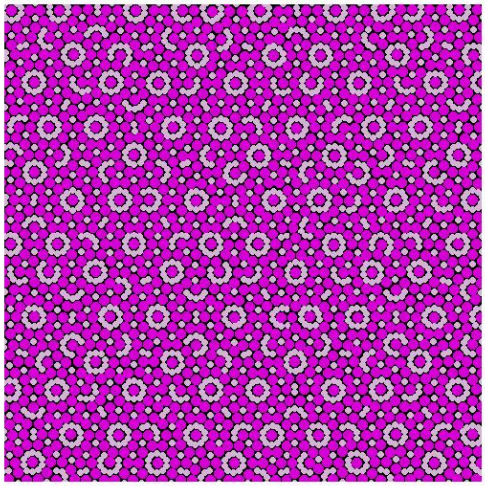

Figure 1: *Das binäre System, im die Simulationen durchgeführt werden.*

hoch symmetrische Struktur ist, ist zu erwarten, dass ein sich bewegender Riss die Cluster vermeidet, anstatt sie zu brechen.

Grundlagen des Bruchs

Nach der isotropen zweidimensionalen Theorie der Elastizität ist ein Riss ein Defekt des Spannungsfeldes. Das Spannungsfeld um die Rissspitze divergiert wie

$$\sigma(r) = \frac{k}{\sqrt{2\pi r}} \tag{1}$$

wobei r der Abstand zur Spitze ist. Die Konstante k heißt Spannungsintensitätsfaktor. Sie hängt nur von der Probengeometrie und von den am Rand angewandten Kräften oder Verschiebungen ab.

Da ein Riss ein Defekt im Spannungsfeld ist, wirkt eine Kraft auf die Rissspitze, die versucht, ihn weiter zu bewegen. Bei Rissen im Gleichgewicht wird die auf die Rissspitze wirkende Kraft von inneren Widerstand des Materials kompensiert. Der Wert des Spannungsintensitätsfaktors, bei dem der Riss sich bewegt, wird vom Griffith Kriterium geliefert, und lautet,

$$k_g = 2\sqrt{\gamma\mu(1-\nu)} \tag{2}$$

γ ist die Oberflächenenergie, d.h. die Energie, die notwendig ist, um eine neue Oberfläche zu erzeugen. μ ist eine elastische Konstante, ν der Poisson Modul.

Es gibt Risse, die durch die Emission einer Versetzung gestoppt werden. Der Wert des Spannungsintensitätsfaktors, bei dem der Riss spontan eine Versetzung emittiert, lässt sich mit der Theorie der Elastizität schreiben,

$$k_e = \frac{\mu}{\sqrt{2\pi r_c}} \frac{b(1-\nu)}{\sin(\theta)\cos(\theta/2)} \tag{3}$$

wobei b der Modul des Burgers Vektors der vom Riss emittierten Versetzung und r_c der Radius des Versetzungkerns sind. Die Versetzungsrichtung bildet den Winkel θ mit der Horizontalen.

Wenn, bei gegebenen Randbedingungen,

$$k_g < k_e \tag{4}$$

gilt, breitet sich der Riss aus, ohne Versetzungen zu emittieren. Wenn andererseits

$$k_g > k_e \tag{5}$$

ist, wird der Riss Versetzungen emittieren, die den weiteren Lauf des Risses behindern.

Der Nosé-Hoover Thermostat

Ein hamiltonisches System mit N Freiheitsgraden wird durch N Positionen $q_1, \cdots, q_N$ und N Impulse $p_1, \cdots p_N$ beschrieben. Das System durchläuft die Punkte $\tilde{x}$ des Phasenraums,

$$\tilde{x} = (q_1, \cdots, q_N, p_1, \cdots p_N) = (\tilde{q}, \tilde{p}). \tag{6}$$

gemäß der mikrokanonischen Verteilung.

Ein System bei einer konstanten Temperatur T durchläuft die Punkte $\tilde{x}$ des Phasenraums gemäß der kanonischen Verteilung

$$\rho(\tilde{q},\tilde{p}) = \frac{\exp(-H(\tilde{q},\tilde{p})/KT)}{\int \exp(-H(\tilde{q},\tilde{p})/KT) d\tilde{q}d\tilde{p}}. \tag{7}$$

Der Nosé-Hoover Thermostat ist ein System von Differenzialgleichungen, deren Dynamik die kanonische Verteilung liefert. Die Nosé-Hoover Dynamik lautet:

$$\begin{cases} \dot{q}_i &= \dfrac{p_i}{m_i} \\ \dot{p}_i &= -\dfrac{\partial V}{\partial q_i} - \nu\eta p_i \\ \dot{\eta} &= \nu\left[\dfrac{T(t)}{T} - 1\right] \end{cases} \tag{8}$$

Man erhält sie durch eine Änderung der hamiltonischen Bewegungsgleichungen, im ein neuer Freiheitsgrad η eingefügt wird, dessen Funktion es ist, im Gleichgewicht die Temperatur gleich T zu setzen. In (8) ist ν eine Konstante, die *Thermostatenmasse* heißt, und deren Wert gleich der Einstein Frequenz gesetzt wird.

Wechselwirkungspotenziale

Die Wechselwirkungskraft zwischen den Atomen im binären System leitet sich aus dem Lennard-Jones Potenzial ab. In Abbildung 2 werden die Potenziale zwischen gleichen (A-A und B-B) und verschiedenen Atomsorten gezeigt.

Molekulardynamik der Rissausbreitung mit Temperatur

Der Thermostat wird durch einen Reibungsterm in den Newtonschen Bewegungsgleichungen realisiert und greift damit an jedem einzelnen Atom an. Er

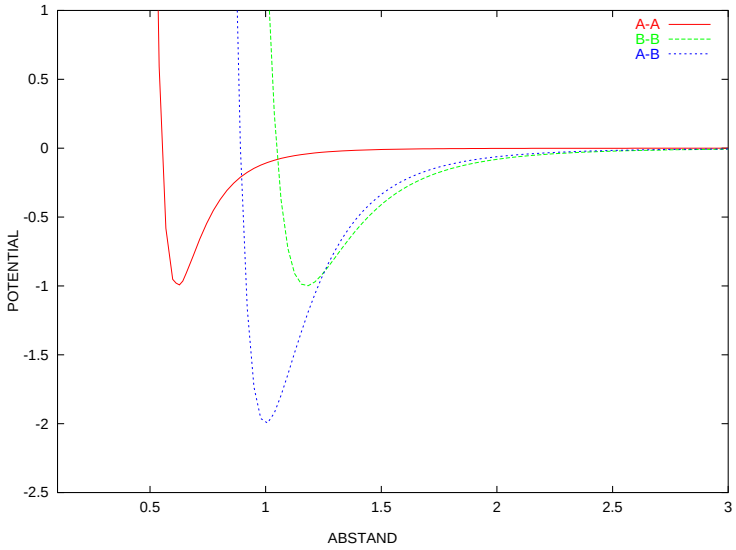

Figure 2: Wechselwirkungspotentiale.

tut dies auch unmittelbar an der Rissspitze, wo sich durch das Brechen der Bindungen eine extreme Nichtgleichgewichtssituation ergibt. Eine solche situation ist unrealistisch. Daher wurde eine neue Geometrie des Nosé-Hoover-Thermostaten eingeführt. Thermostatisiert wird nun nur noch außerhalb eines elliptischen Stadions, das die Rissspitze einschließt.

Numerische Ergebnisse

Die Rissausbreitung wurde bei verschiedenen Temperaturen und Lasten untersucht. Bei jeder Temperatur wurden ein Schnitt in der Probe gemacht und die Ränder um Δ verschoben (Abbildung), bis die kritische Last Δ_c gefunden war. Bei der kritischen Last wurde Die Probe relaxiert, und anschliessend weiter um Δ_c verschoben.

Das Rissausbreitungsverhalten unterscheidet sich in drei Temperaturbereiche.

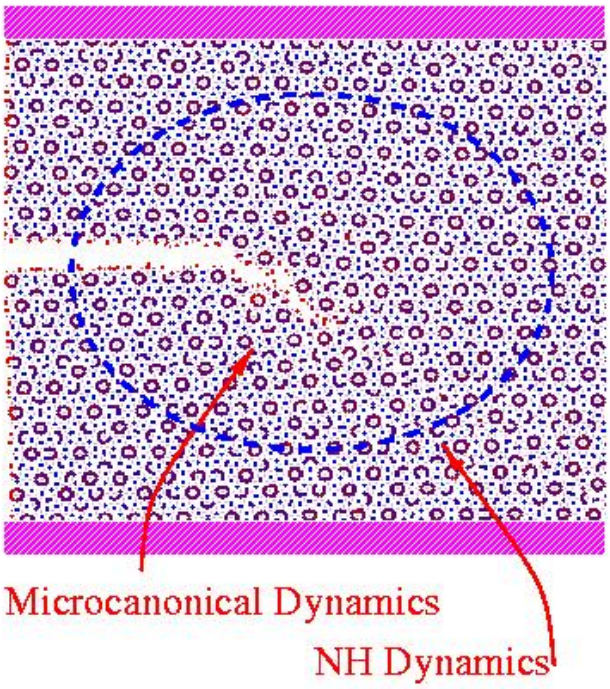

(a) Molekulardynamik der Rissausbreitung mit Temperatur.

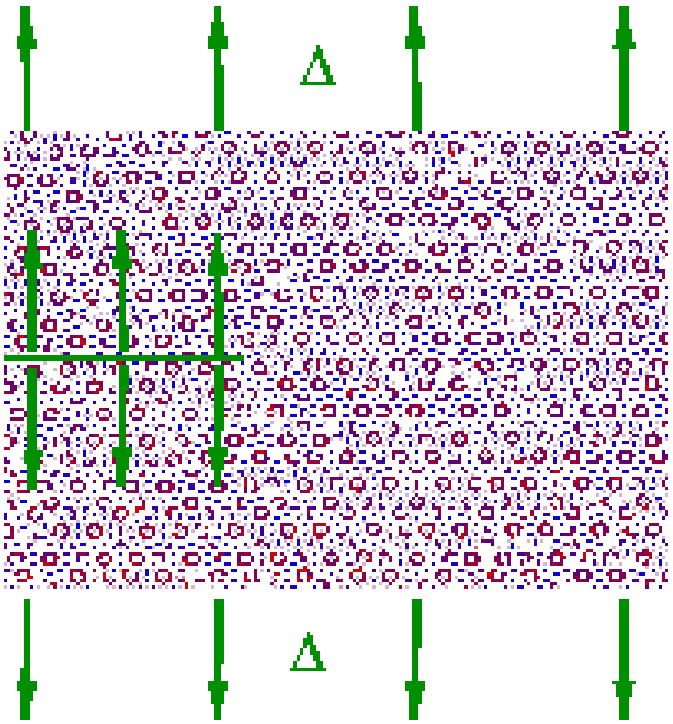

(b) Probenpräparation

Niedrige Temperatur

Niedrige Versetzungsemissionsrate Bei niedrigen Temperaturen $T < 31\%T_M$, wobei T_M die Schmelztemperatur ist, und niedrigen Lasten $\Delta > \Delta_c$, wird aus der Rissspitze nur eine Versetzung emittiert (Abbildung 3). Die Versetzungsemission ist in diesem Fall ähnlich wie bei $T = 0$. Die emittierte Versetzung hinterlässt eine *Phasonenwand*, auf der die Oberflächenergie minimal ist. Der Riss stoppt eine Zeit lang und folgt dann der Versetzung. Die Versetzungsemission kann anhand des Verhältnis von k_e zu k_g erklärt werden, weil die Rissspitze während ihres Laufs eine Ebene trifft, auf der plötzlich k_e kleiner als k_g ist.

Hohe Versetzungsemissionsrate Wenn die Last größer wird, werden aus der Rissspitze viele Versetzungen emittiert, die den Riss stoppen. In diesem Bereich ist die Rissausbreitung durch hohe nicht lineäre Effekte charakterisiert (Abbildung 4).

Mittlere Temperatur

Wenn die Temperatur um $41\%T_M$ liegt, bilden sich vor der Rissspitze Löcher, die hier die Rolle der Versetzungen spielen (Abbildung 5).

Hohe Temperatur

Bei $T = 52\%T_M$ findet keine Rissausbreitung mehr statt. Eine Versetzung wird aus der Rissspitze emittiert, die den weiteren Lauf des Risses stoppt. In diesem Temperaturbereich zeigt das Material ein duktiles Verhalten.

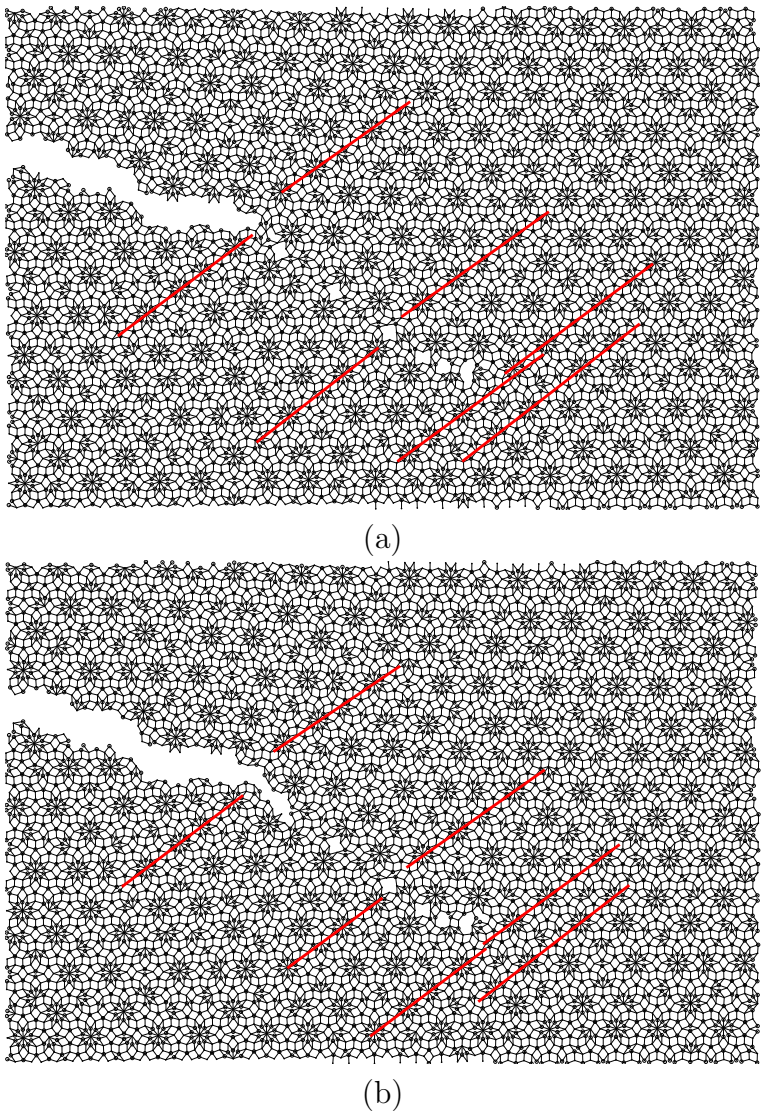

(a)

(b)

Figure 3: Versetzungsemission. (a) Eine Versetzung wird emittiert. (b) Der Riss folgt der Versetzung.

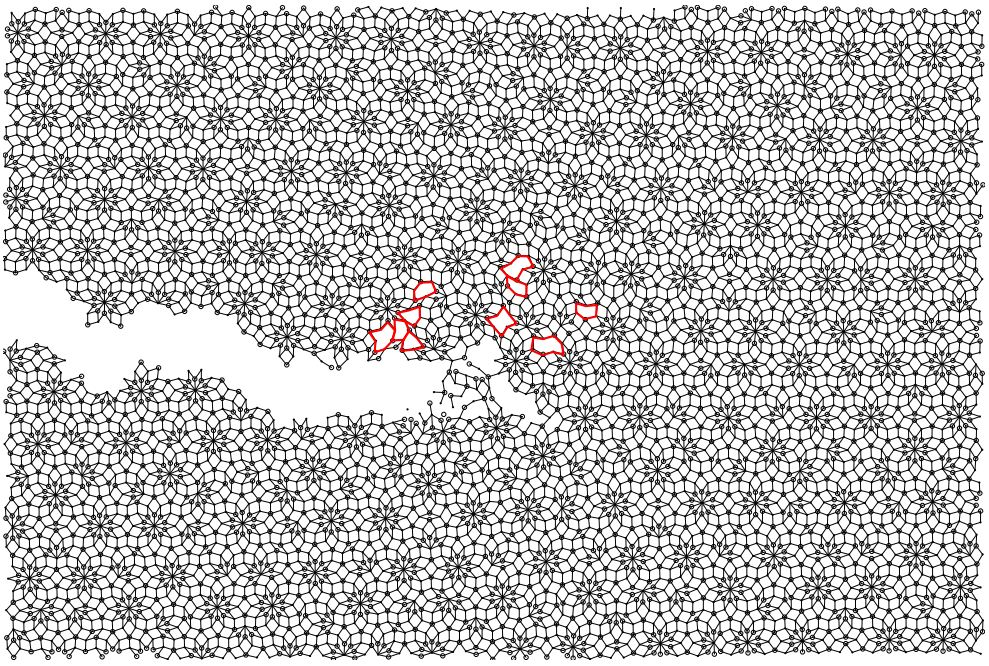

Figure 4: Hohe Versetzungsemissionsrate. Aus der Rissspitze und der Rissoberfläche werden viele Versetzungen emittiert.

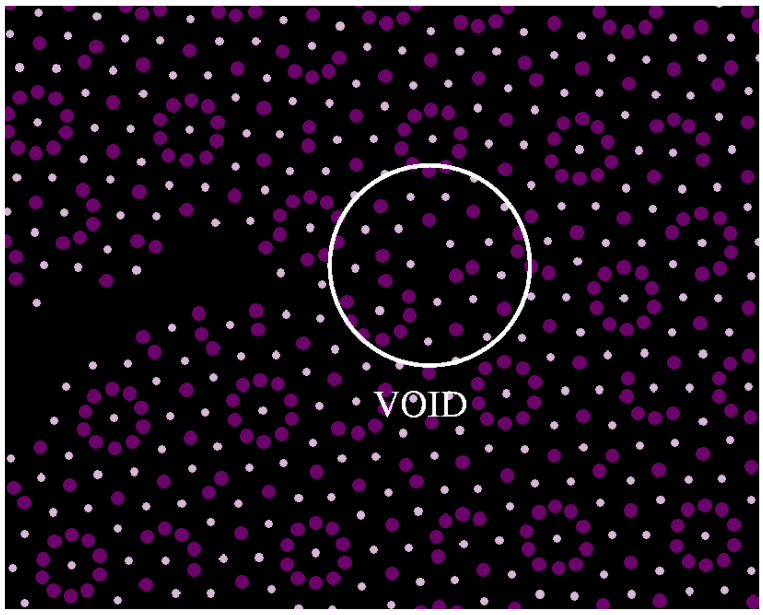

Figure 5: Bei mittleren Temperaturen bildet sich ein Loch vor der Rissspitze.

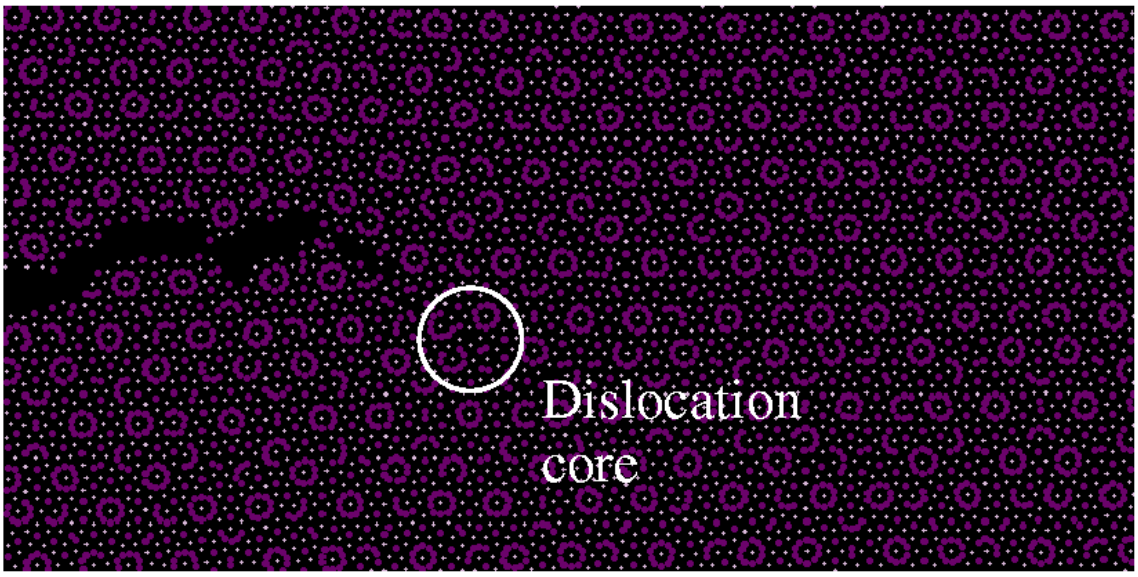

Figure 6: Bei $T = 52\%T_m$ wird eine Versetzung aus der Rissspitze emittiert, die den weiteren Lauf des Risses stoppt.

Chapter 1

Introduction

Things break. This is the everyday experience of everyone of us. Fracture affects our life much deeper than we realize. It is obviously not relevant in our life if a glass in the kitchen falling from our hands breaks. And the little cracks on the walls of our apartment have in the most cases no consequences on the stability of our house. Completely different is the case in which an airplane fuselage tears mid-flight, like an Aloha Airlines Boeing 737 did, or if, like during World War II, a fracture suddenly and unexpectedly destroys a ship (see Fig. 1.1) cutting it in two pieces. Even worse are the consequences of an earthquake, which often generates fractures at a very big size scale. The economical interests involved in fracture problems are enormous. In 1983 the US National Bureau of Standards placed an annual price tag of a quarter of a trillion dollars on fracture-induced structural failures. With the advent of the microelectronic revolution the investment increased substantially: the impact of the development of cracks in multi-layered integrated circuits on the rate of advance of this technology is enormous. From an engineering point of view it would be extremely important to be able to design microstructures of increased *toughness*, which is the resistance of a material to the opening of a crack.

Apart from the interest coming from technological applications the study of fracture and of the physical basis of material strength is a fundamental question of condensed-matter physics.

Historically continuum theory has been the first tool used to tackle the fracture problem. The continuum theory of fracture is a difficult task because the stress field in the vicinity of the crack tip is highly nonlinear and decays slowly far from the tip. Moreover the model is complicated by the presence of

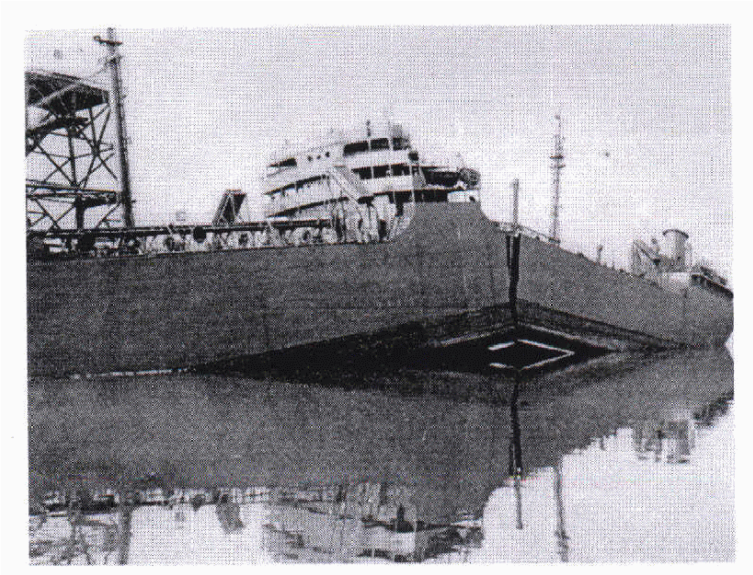

Figure 1.1: *Photograph of the T-2 tanker that failed at its pier: "On January 16, 1943, a T-2 tanker lying quietly at her fitting-out pier at Portland, Oregon, suddenly cracked in a brittle manner 'without warning and with a report that was heard for at least a mile'."*

dislocations, which are defects often induced in the material by the fracture. The interaction of dislocations and cracks plays a crucial role in determining the overall toughness of the material and the dynamics of fracture. The classical theory of elasticity treats cracks as mathematical cuts which begin to move when an infinitesimal extension of the crack releases more energy than is needed to create a fracture surface [64, 31, 74]. This idea, very successful in practice, is incomplete. In a lattice there are some velocities for which crack solutions do not exist at all, others where cracks are unstable and accelerate to higher velocities, and yet others for which crack tips are unstable and break apart altogether [71]. While these conclusions are compatible with continuum mechanics, they were not predicted by it. There are also some experimental observations which are somewhat surprising.

- Cracks in amorphous brittle material such as glass or Plexiglas pass almost instantaneously from quasi-static motion to motion at about

15% of the Rayleigh wave speed[1] [54, 98, 59].

- Cracks travel seldom faster than 60% of the Raleigh wave speed, although according to continuum theory this is the limiting velocity [4, 58].

- At about 40% of the Rayleigh wave speed the acceleration of cracks slows down [49, 50].

Continuum mechanics does not explain satisfactorily these characteristics of crack dynamics, while an atomistic model does [71]. The simulations of crack propagation at low temperatures contained in the second part of this work have shown, like in real experiments, both a velocity gap and a limiting value of the crack velocity (see Chapter 8). Continuum mechanics is not well suited to take into account microscopic processes where elastic energy is converted to broken bonds, but nevertheless can give a useful guideline to understand qualitatively even at the atomistic scale the phenomena observed. And this is the reason why a big part of Chapter 3 of this work has been devoted to the exposition of the classical results of the theory of elasticity applied to fracture problems.

One of the tools used at the atomistic scale to investigate fracture propagation is molecular dynamics (MD). MD makes it possible for the first time to follow in great detail the dynamics of fracture in realistic and very complicated situations where both elastic and plastic effects, like dislocation emission, are present. The price to be payed for using such a powerful tool is high. On one hand the great amount of data generated in a single MD experiment may require a big investment in the development of the analysis tools. On the other hand the lack of a "supporting" theory makes the work often very specialized. Even if some guide lines have been outlined in years of experience in the field, MD of crack propagation may produce effects which are completely different and peculiar from system to system in which the simulations are done.

Quasicrystals have been discovered in 1984 [93], and in all these years the physics of quasicrystals has been explored in detail both from a theoretical and an experimental point of view [29, 86, 51, 24]. All these efforts yield the required knowledge for tailoring the properties of the known quasicrystalline

[1]The Rayleigh wave speed of a material is the mean velocity of the longitudinal and transverse waves traveling on the surface of the material

alloys for technological purposes, and in the frame of the development of a competitive technology based on the properties of quasicrystals, the initiation and propagation of fracture in these materials represents one of the most important questions in the field which are to be addressed. Moreover, aside from the industrial interest, crack propagation in quasicrystals opens a completely new and interesting insight into the physics of fracture. There are deformations of a quasicrystalline structure which correspond to a degree of freedom, the so-called *phasonic* one (see Section 2.4.2 on page 35), absent in common crystals, which plays a crucial role in the dynamics of fracture in these materials.

Molecular dynamics of crack propagation in a quasicrystalline binary system derived from a Tübingen triangle tiling (see Section 2.5.2 on page 39) has been intensively studied at zero temperature [77]. The present work deals with a molecular dynamics study of fracture propagation in the same system at different temperatures.

The work is divided into two parts.

The first part contains the preliminaries.

Chapter 2 describes briefly the quasicrystals in general and the quasicrystalline binary system out of the Tübingen triangle tiling in which the numerical results of the second part have been computed.

Chapter 3 deals with the physics of fracture. Even if the aim of this work is primarily to give an atomistic description of crack propagation, the results of the continuum theory of fracture have shown to be very useful for the qualitative understanding of the effects observed in the simulations. The classical results of fracture continuum mechanics are the content of the first part of the chapter. The second part exposes a didactic description of a simple atomistic model for crack propagation, useful for introducing the characteristics of fracture dynamics common to all the atomistic models. The last part contains the experimental results of crack propagation in an icosahedral three-dimensional quasicrystal.

The standard approach of continuum theory to crack propagation involves elastic energies, which, in a system at constant temperature, are equal to free energy differences. The techniques used for simulating a system at constant temperature and for computing free energy differences, which have become standard tools in the field of computational statistical mechanics at equilibrium, are the topics of Chapter 4.

In Chapter 5 the interaction potential and the model system used in the simulations are described in detail.

An original model for the simulation of crack dynamics at constant temperature is proposed in Chapter 6.

The second part contains the numerical results of the simulations performed in the quasicrystalline binary system derived from the Tübingen triangle tiling.

In Chapter 7 are reported original free energy calculations used to compute the surface energies, the elastic constants and the critical displacements involved in crack propagation. The numerical reliability of the calculations, performed in a medium size system of 4134 atoms, has been tested with two different methods, the classical umbrella sampling (Section 4.6.3 on page 86) and a less known method based on the phase space compressibility of the Nosé-Hoover equation of motions (Section 4.6.1 on page 81).

Simulations of fracture propagation at different temperatures have been performed in a sample of many atoms (74210). For each temperature, crack propagation has been investigated in detail at different loads, and the results of this study have been collected in Chapter 8. The influence of dislocation emission on crack propagation represents one of the crucial topics in the field which are to be tackled. In Chapter 8 by means of numerical elastic estimates based on the results of Chapter 7, for the first time an explanation of the mechanisms of dislocation emission and crack propagation in the range of low loads and low temperatures is being proposed. There are features of the crack propagation simulations collected in this chapter which qualitatively reproduce some of the characteristics of experimentally observed crack propagation in a three-dimensional quasicrystal. A detailed comparison is contained in the conclusion of the chapter.

Part I

PRELIMINARIES

Chapter 2

QUASICRYSTALS

2.1 Introduction

For many years the physics of solid state has been intended to be the physics of crystalline substances, which exhibit perfect translational symmetry. The translational symmetry induces important selection rules which can be used in the interpretation of the experiment and in the theoretical modeling.

In the last years interest has grown considerably in "non-crystalline" materials, which is a category of state of matter ranging from liquids or amorphous solids to incommensurate structures. Amorphous solids and liquids can possess some kind of local order, typically restricted to a short arrangement of atoms. The atoms of an incommensurate structure are displaced from the periodic positions of a lattice by an amount which is itself periodic in space, but that period and that of the underlying lattice are not in a rational ratio.

Quasicrystals are non-crystalline materials showing a perfect long-range order, but with no periodic ingredients [51].

2.2 The discovery of quasicrystals

In 1984 Schechtman, Blech, Gratias, and Cahn [93] discovered, by quench from the melt of AlMn alloys, a new state of condensed matter from their transmission electron microscopy experiments. They observed relatively sharp Bragg peaks at positions related successively by ten, six, and twofold symmetries. The Bragg peaks are not reproduced by translation, and the intensity

of the diffracted beams does not decrease in a monotonic way with the scattering angle, as it should happen for a crystal (Fig. 2.1).

All these features are characteristic of long range order, which cannot be periodic, while the diffraction patterns show rotation axes of order forbidden symmetry for a periodic structure. The term "quasicrystal" has been given to such structures [65].

As time went by more and more materials were discovered which did not possess crystallographic symmetries. Ishima [46] and Bendersky [16] discovered an important class of quasicrystals, the *T-phases*. A quasicrystalline T-phase is made of two-dimensional quasicrystalline layers, which are packed periodically in the z-axis perpendicular to the slide, because out of such a quasicrystalline phase it is possible to build a quasicrystal of some millimeters, and thus this quasicrystalline phase is experimentally intensively studied.

2.3 Potential applications of quasicrystals

The physical, chemical and mechanical properties of quasicrystals might have important technological applications [29].

Transport properties Quasicrystals have peculiar electron transport properties which have been described in many books [52]. The resistivity of many quasicrystalline alloys is typically 10-100 times bigger than that of the amorphous metal [17]. Moreover the resistivity decreases much with temperature. The ratio of the resistances $\rho(4\text{K})/\rho(300\text{K})$ is about 2 to 10, for crystalline substances the same ratio is about 10^{-3}. Thus quasicrystals have a large negative temperature coefficient of the resistivity, in addition to high resistivity values, and might be used as temperature sensors with high sensitivity in a broad range of temperatures.

Another use of transport properties of quasicrystals, namely heat isolation is in pre-industrial development [27]. In this case the advantage of quasicrystals is twofold. They are very efficient heat insulators in a temperature range extending from room temperature to their melting point. Furthermore they become plastic over 600° so that the interfacial stresses born at the contact with metallic substrates are canceled out, making them interesting as very efficient thermal barriers.

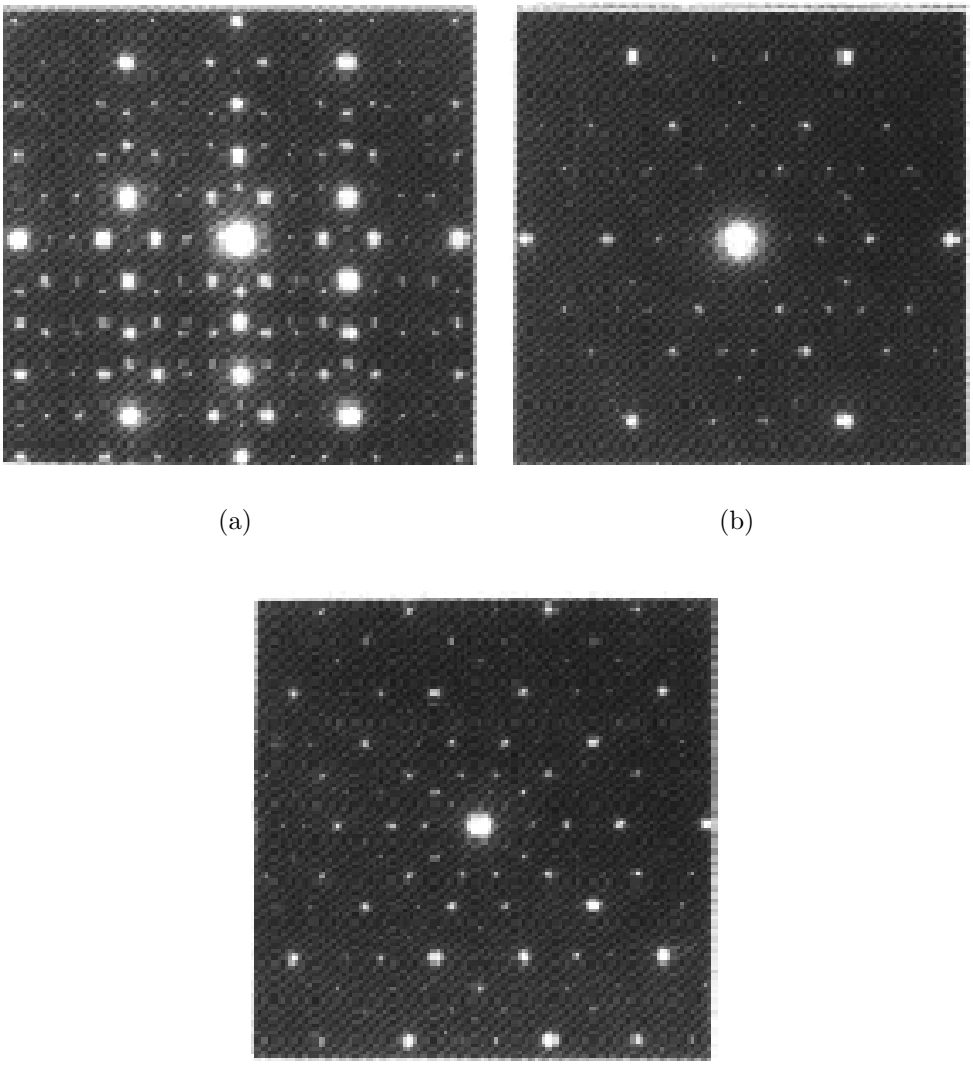

(a) (b)

(c)

Figure 2.1: *Quasicrystalline* $Al_{86}Mn_{14}$ *alloy: bright field of the icosahedral phase. Diffraction patterns of the alloy with a zone axis parallel to a five (a), three (b) and twofold axis (c). From [68].*

Surface properties The surface energy γ_S of a material is often estimated with the help of wetting experiments. It suffices to deposit a droplet of water on the surface and to measure the contact angle between liquid and solid. Many quasicrystalline samples, approximant and amorphous alloys exhibit a wetting behavior to water comparable to Teflon whereas crystalline metallic specimens do not. Application is straightforward to coatings of polymer moulds, cooking utensils, etc., which require to keep the adherence of the reactants to the container surface as weak as possible.

Strengthening of metallic matrices A quasicrystalline powder incorporated in soft metallic alloys increases their yield strength and hardness. The tensile yield strength obtained with bulk samples is quite comparable to that of the best aeronautic alloys whereas the deformation at rupture is much larger. Since the specific weight is the same, these alloys form a new competitive family of light, high strength materials.

Hydrogen storage Absorption and storage of hydrogen is of great importance for the availability of a non polluent fuel which, when combined with oxygen, delivers energy in combustion engines. The first example of a quasicrystal suitable for hydrogen storage is $\mathrm{I} - \mathrm{Ti_{45}Ni_{17}Zr_{38}}$. Another example of hydrogen storage material was found in Zr-Cu-Ni-Al glasses which transform upon annealing into nanosized quasicrystals. This later material is able of store hydrogen in large amounts, leading to a ratio of hydrogen to matrix atoms larger than 1.6. This density is higher than in liquid hydrogen.

2.4 Modeling a quasicrystal

2.4.1 Quasiperiodicity

In a periodic structure the atomic positions are described by lattice points:

$$\mathbf{r} = n_1\mathbf{e}_1 + n_2\mathbf{e}_2 + n_3\mathbf{e}_3 \tag{2.1}$$

where n_1, n_2, n_3 are integers and $\mathbf{e}_1, \mathbf{e}_2, \mathbf{e}_3$ are three linearly independent vectors.

Crystal structures are determined by diffraction of electrons, X-rays, or neutrons. Each atom in the sample may be considered as a source of secondary spherical waves whose strength is controlled by the scattering power f_i of the atom. The sample is irradiated with a monochromatic beam of rays with wave vector $\mathbf{k}$, and the intensity of scattered rays is observed along different wave vectors $\mathbf{k}_1$. The rays are considered to be elastically scattered, and therefore $|\mathbf{k}| = |\mathbf{k}_1|$. The signal amplitude in the direction $\mathbf{k}_1$ is given by :

$$F(\mathbf{Q}) = \sum_j f_j \exp(i\ \mathbf{r}_j \cdot \mathbf{Q}) \tag{2.2}$$

where the sum runs over all the lattice points, and $\mathbf{Q} = \mathbf{k}_1 - \mathbf{k}$. Absolute maxima of Eq. 2.2 can be measured in the directions $\mathbf{Q}$ of the reciprocal lattice where [8]:

$$\exp(i\ \mathbf{r}_j \cdot \mathbf{Q}) = 1 \tag{2.3}$$

The diffraction patterns give an exact information on the underlying lattice structure.

Periodicity is not the only condition under which a system may show long range order. Let us consider for example a single one dimensional lattice whose points density is given by:

$$\rho(x) = \sum_n \delta(x - na) \tag{2.4}$$

where a is the lattice spacing. If we superimpose to the density ρ another density with a different periodicity:

$$\rho = \sum_n \delta(x - na) + \sum_m \delta(x - \alpha ma) \tag{2.5}$$

and if the ratio of the two periods α is not a rational number, the system is still long-range ordered, but not anymore periodic. A very interesting example of long-range ordered structure is the Fibonacci chain. One considers two

segments S, the short one, and L, the large one, and builds a quasiperiodic system using an iterative procedure. At every iteration every segment L or S is replaced by the segment LS or L respectively. For an appropriate "initial condition", for example L, the produced sequence of segments is:

L
LS
LSL
LSLLS
LSLLSLSL
LSLLSLSLLSLLS

The ratio of L/S converges to the irrational number $\tau = (1 + \sqrt{5})/2$, and thus the sequence has no repetition distance and builds the canonical Fibonacci chain. In this case if an atom is placed at every junction of two segments, the system would possess a perfect long-range order, because every atomic position can be uniquely determined, but no periodicity at all. If the atoms are all of the same type, the structure factor Eq. 2.2 for a Fibonacci chain is labeled by two integers h, h', even if the structure is one dimensional, and it can be demonstrated to be:

$$F(\mathbf{Q}) = \sum_{h,h'} F_{h,h'} \delta(\mathbf{Q} - \mathbf{Q}_{h,h'}) \tag{2.6}$$

where:

$$\mathbf{Q}_{h,h'} = \frac{2\pi\tau^2}{\tau^2 + 1}(h + h') \tag{2.7}$$

The peaks are still very sharp, like for a periodic structure, but they form a dense pattern. The brightest intensity spots are the maxima of $F_{h,h'}$, for which no analytical expression is given here [51], and they are reached at the values of h/h' close to τ, that is, when h and h' are the Fibonacci integers (1,1),(2,1),(3,2),(5,3). Outside this sequence the intensities decrease strongly. A system possessing such a structure factor is called a **quasicrystal**.

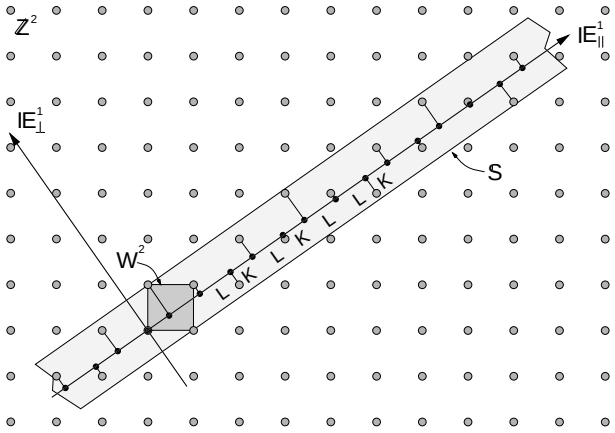

Figure 2.2: *Cut and projection method for a one dimensional quasicrystal. The points of a two dimensional cubic lattice are projected on the $E_{||}$ line. The width of the strip defining the acceptance domain is chosen so to have a cross section in $E^{\perp}$ equal to that of the unit cell W^2.*

2.4.2 Quasiperiodicity by projection from a higher dimensional space

As mentioned, the characteristics of a quasiperiodic structure arise from the fact that their symmetries are not compatible with the space groups accepted in the physical space, but these symmetries could be accepted at the cost of increasing the dimension of the space.

In a simple square lattice in two dimensions, whose mass density is the function:

$$\rho(x,y) = \sum_{n,m} \delta(x - na)\delta(y - ma) \tag{2.8}$$

let us consider two straight lines perpendicular to each other, $E^{||}$ and $E^{\perp}$ (see Fig. 2.2). The line $E^{||}$ is called the *parallel space* and $E^{\perp}$ the *orthogonal space*. If we project the lattice points on $E^{||}$ two situations can arise.

When the slope of $E^{||}$ is rational, the projected one dimensional structure is a discrete periodic set of points. The better α approximates an irrational number, the longer becomes the repetition length of the periodic set of points, which takes the name of *periodic approximant*.

When the slope is irrational, the projected structure is not anymore periodic, and it is dense in $E^{||}$. The set of projected points becomes discrete if one restricts the points of the lattice which can be projected to those belonging to an *acceptance* strip. The width of the strip is chosen so as to have a cross section in $E^{\perp}$ equal to that of the unit cell. The projected structure is now made of two segments of length $a\cos\alpha = L$ and $a\sin\alpha = S$, where α is the value of the slope of $E^{||}$. If $\alpha = \tau$ the distribution of the segment (L, S) is the Fibonacci sequence.

By means of the cut and project procedure deformations of a quasicrystalline material may be defined which are unusual in a crystalline structure. Generally a deformation of the higher dimensional space has two components:

- When the deformation in the higher dimensional space has only components parallel to the physical space, the sequence of the projected points remains the same, but their relative length may change. The degree of freedom of such a movement of the projected structure is called *phononic*.

- When the deformation has a component in the perpendicular space a completely new situation can take place. Some points could leave the acceptance strip and new ones could enter, and as a result the sequence of the projected points may change. For example in Fig. 2.3 the point labeled 1 leaves the strip and the point labelled 2 enters it, if the lattice is shifted in the direction of the vector $\mathbf{b}$. As a result we would observe locally a change of the sequence SL to LS. Such a sudden change is called *flip*, and the degree of freedom associated to such a change of the quasicrystalline structure is called *phasonic*.

2.5 Examples of two dimensional quasicrystals

2.5.1 The Penrose and Tübingen tilings

In this section two important 2-dimensional tilings are presented: the Penrose tiling and the *Tübingen triangular* tiling. From the Tübingen triangular tiling, by means of a decoration procedure, the binary system is obtained in which all the simulations of this work have been done.

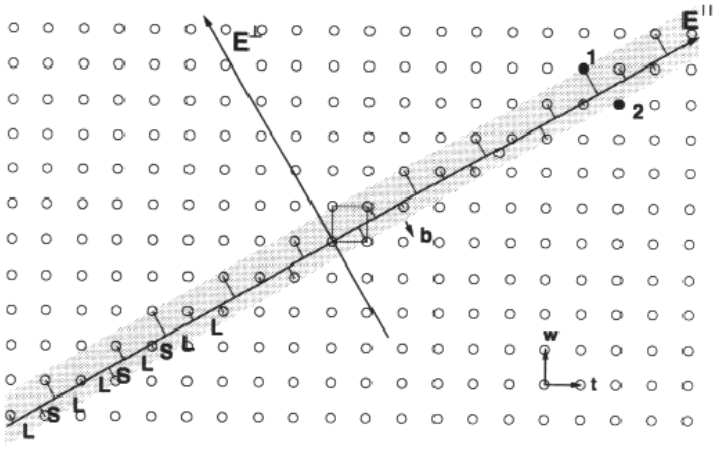

Figure 2.3: *The flip of an atom with the cut and projection method. The point labeled 1 leaves the strip and the 2 enters it, if the lattice is shifted in the direction of the vector* $\boldsymbol{b}$.

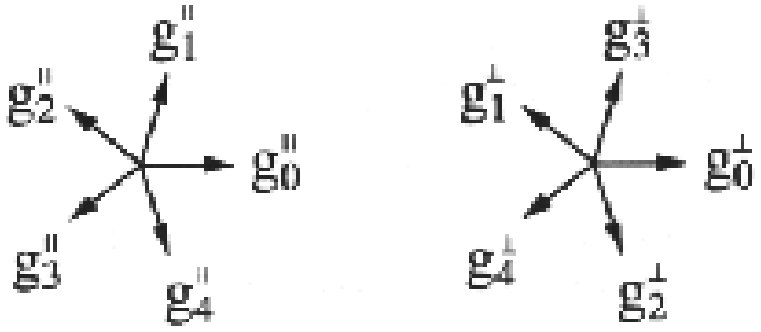

Figure 2.4: *Projection of the canonical basis of the cubic lattice in 5 dimensions on the physical space (left) and on the orthogonal (right).*

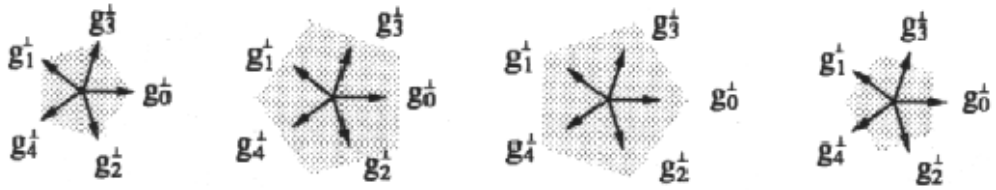

Figure 2.5: *Acceptance domains of the Penrose tiling.*

The tilings are built using the cut and projection procedure. The higher dimensional space is a five dimensional cubic lattice E^5, which is spanned by the five basis vectors $\mathbf{k}_i$, $i = 1, .., 5$. E^5 can be decomposed into three disjoint subsets, which are invariant under the action of the cyclic permutation group C_5: two two dimensional subsets and one one dimensional [33, 99].

A rotation of 72^o in one of the two dimensional subspaces is seen as one of 144^o in the other. The basis vectors $\mathbf{k}_i$ are projected onto the two 2-dimensional subspaces, and the physical subspace is the one in which the transformation of $\mathbf{k}_i$ into $\mathbf{k}_{i+1}$ is seen as a rotation of 72^o. In Fig. 2.4 are represented the vectors $\mathbf{g}_i^\perp$ of the perpendicular space and $\mathbf{g}^{||}$ of the physical one from the projection of the basis vectors $\mathbf{k}_i$. Not all the points of E^5 are projected, but only those belonging to the root lattice A^4. A^4 is the subset of the points E^5 for which the sum of the coordinates is equal to 0. The acceptance domain for the projection method is built using the *Voronoi* cell of A^4 . The Voronoi cell of a point p in A^4 is made out of all the points whose distance from p is the smallest.

The acceptance domain of the *Penrose tiling* is the projection onto the perpendicular space of the dual of the the Voronoi cell of A^4, the Delaunay domain. The projection gives four pentagons lying on the *coordination classes T=1,2,3,4*. A coordination class $T = n$ is the subset of E^5 made out of all the points for which the sum of the coordinates is equal to n. In Fig. 2.5 the acceptance domains of the Penrose tiling are represented. The vertices of the tiling are the projection of the points whose projection to the perpendicular space is in the acceptance domain (see Fig. 2.8).

The acceptance domain in the perpendicular space for the *Tübingen* tiling is represented in Fig. 2.6. A particular procedure described in [13] is needed

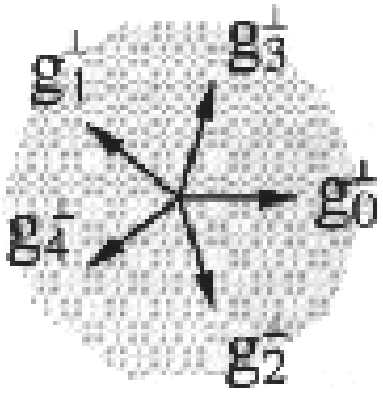

Figure 2.6: *Acceptance domain for the Tübingen triangular tiling.*

to build the vertices of the tiling (Fig. 2.7).

2.5.2 The decoration of the Tübingen tiling

A binary system can be obtained by decorating the Tübingen triangular lattice with two types of atoms, one big and the other small. The big atoms are placed on the vertices of the tiling, and the small ones are to the center of the isosceles triangles. Fig. 2.9 shows the bond representation of the Tübingen triangular tiling decoration. The bond representation is obtained by connecting each atom of the binary tiling with its nearest neighbors. The bond representation gives useful information about the structure of the Tübingen tiling (see Section 5.2 on page 93). In this binary tiling there are *clusters* of one atom surrounded by two concentric rings of ten atoms. A cluster is a highly symmetric structure, and its toughness may be very high. A fracture propagating in such a material is expected to move between the clusters instead of trying to break one of them. The cluster centers are situated on five families of parallel lines, mutually rotated by 36° with a large and small separation within each family, arranged in a Fibonacci sequence [77].

The next chapter deals with the physics of fracture and it is divided into two parts. The first part exposes the essential classical results of continuum theory of fracture, which are relevant in the qualitative analysis of the results of the simulations. The second part contains a didactic description of

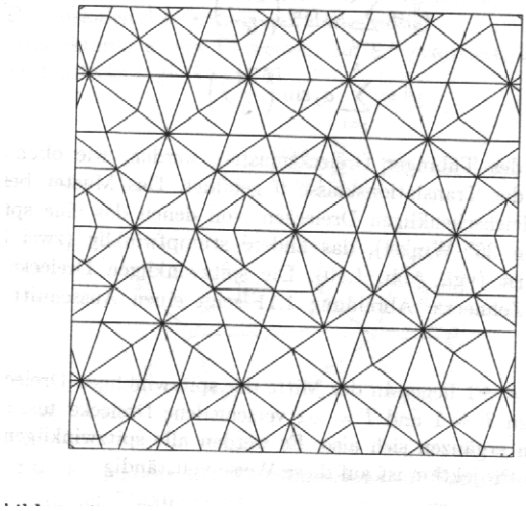

Figure 2.7: *Tübingen triangular tiling.*

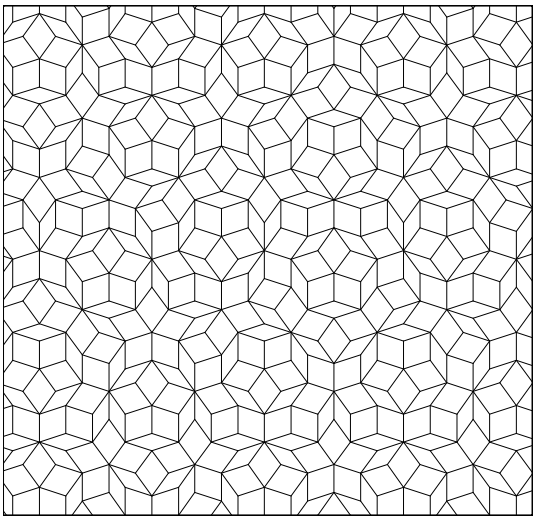

Figure 2.8: *Penrose tiling.*

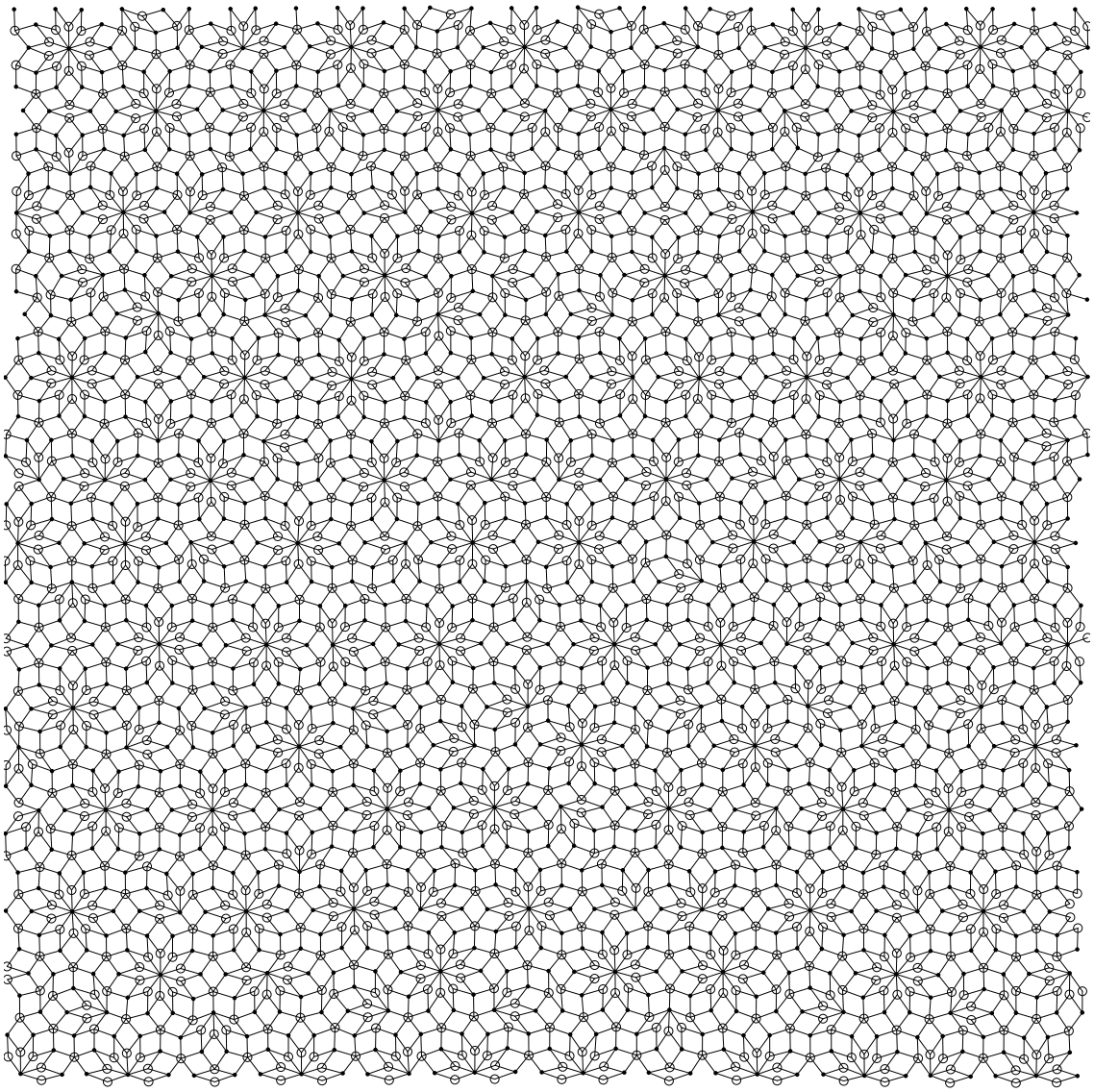

Figure 2.9: *Bond representation of the Tübingen triangular tiling decoration. The bond representation is obtained by connecting each atom of the binary tiling with its nearest neighbors.*

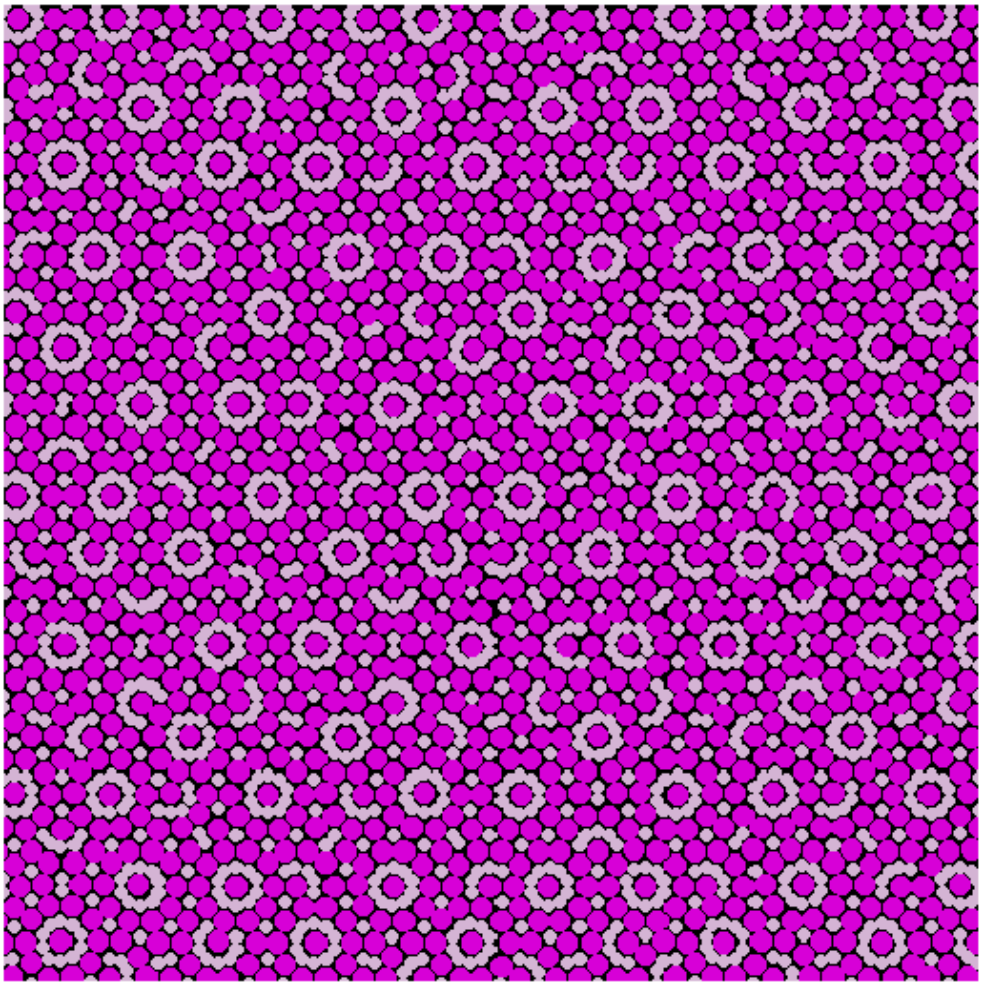

Figure 2.10: *Binary system obtained by decorating the Tübingen triangular tiling.*

a simple atomistic model for crack propagation, useful for introducing the characteristics of fracture dynamics common to all the atomistic models.

Chapter 3

THEORY OF FRACTURE

In the first part of this chapter the ideal modeling of the three basic modes for the opening of a crack is presented. The second part is devoted to an introduction of the basic notions of the continuum theory of cracks and dislocations and of their mutual interaction [96]. The third part is a brief review of the atomistic models for crack propagation.

The reader is supposed to be familiar with the linear theory of elasticity, and with the concept of *dislocation*.

An excellent treatise of the physics of dislocations in crystals can be found in [81, 55], and dislocations in quasicrystals have been intensively studied in [76, 75, 69, 62, 20, 47].

Quasicrystals are non-crystalline materials showing a perfect long-range order, but with no periodic ingredients [51]. The physics of crack propagation in non-crystalline materials will not be treated in this work. The reader can find an interesting treatise of statistical models for disordered media in [38].

3.1 Fracture modes

A crack is a three-dimensional defect whose fracture plane may be a very rough surface. Nevertheless for analytical purposes a crack is always modeled as a one-dimensional line defect on a flat cleavage plane. There are three basic modes of loading a crack, corresponding to the orientation of the stress with respect to the cleavage plane (see Fig. 3.1). The combination of these modes describes any ideal opening mode of a crack. In Mode I the force acting on the crack is perpendicular to the cleavage plane. Mode II is characterized

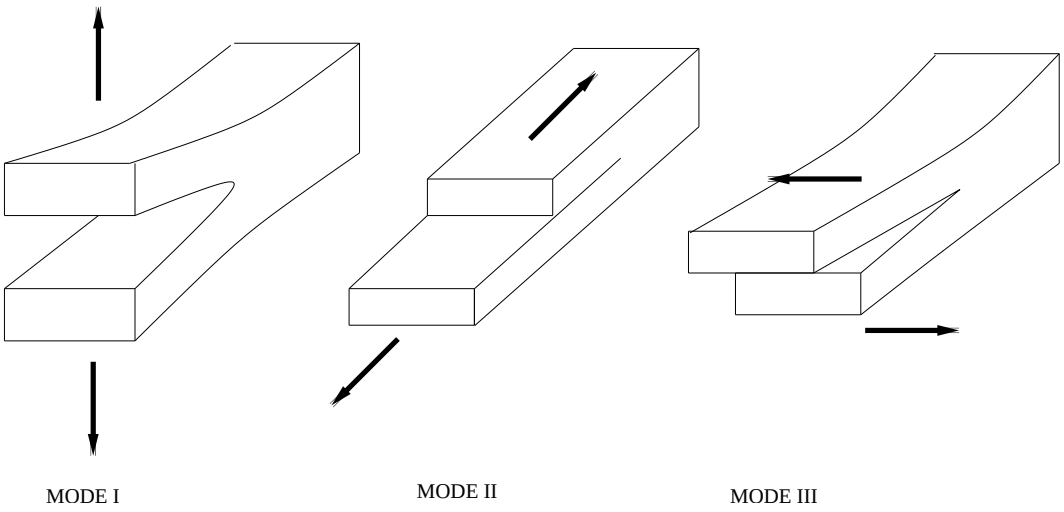

Figure 3.1: *The three modes of a fracture. In Mode I the force is exerted normal to the cleavage plane. In Mode II the force lies in the cleavage plane and is normal to the crack line. In Mode III the force is again in the cleavage plane but is parallel to the crack line.*

by a force which lies on the cleavage plane and is perpendicular to the crack line. The force acting on the crack for Mode III is again in the cleavage plane and is parallel to the crack line.

3.2 The elastic fields of cracks and dislocations

3.2.1 Introduction

The continuum theory of cracks and dislocations is a high specialized and very difficult field. A detailed derivation of the analytical expression of the force fields of cracks and dislocations would require for the reader the knowledge of complex potentials, conformal mappings and singular integral equations which are out the scope of this work and must be addressed by specialized books [14, 89, 15, 34, 64]. The aim of this section is just to highlight the contents and the results of the theory in the very simple case of the penny

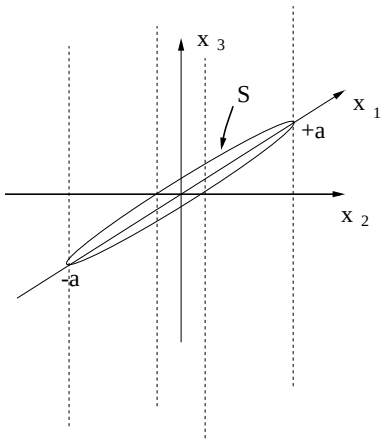

Figure 3.2: *Geometry of the crack. A three dimensional infinite isotropic medium is cut from $-a \leq x_1 \leq +a$ on the axis x_1 of a system (x_1, x_2, x_3) of Cartesian coordinates.The lips of the free surface S are represented in figure separated for sake of clearness, but they are to be intended to be initially one touching the other.*

crack, skipping all the calculations which the interested reader can find in [79]. Moreover the basic equations of theory of elasticity are restricted here to the isotropic case, and no anisotropic effects will be taken into account even if in real applications they cannot be neglected [25, 48].

3.2.2 General equations

The geometry of the crack we are interested in is depicted in Fig. 3.2, the so called *penny crack*. A three dimensional indefinite isotropic medium is cut from $-a \leq x_1 \leq +a$ on the axis x_1 of a system (x_1, x_2, x_3) of Cartesian coordinates. The lips of the free surface S are represented in the figure separated for sake of clearness, but they are not: they are initially one beside the other, and only when a load is applied they may separate. The crack cleavage plane is contained in the $x_1 - x_2$ plane.

The equilibrium of the elastic medium requires that at every point inside the material:

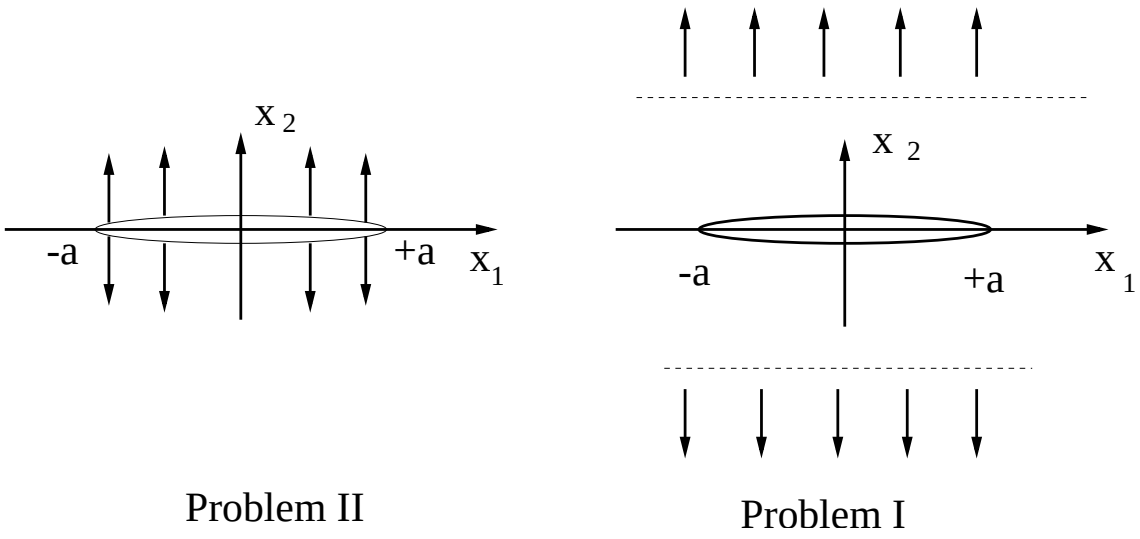

Figure 3.3: *Two load systems for a penny crack. In Problem II the load is applied on the crack surface. In Problem I the crack is loaded very far away from the crack.*

$$\frac{\partial \sigma_{ij}}{\partial x_j} = 0 \tag{3.1}$$

where σ_{ij} is the stress tensor and the summation convention over repeated indices is assumed.

There are two ways a crack can be loaded. In the so-called *Problem I* the load is applied at *infinity* far away from the crack, and in the *Problem II* the forces are exerted on the lips of the cut surface (see Fig. 3.3). For Problem I the crack surface S is free and the boundary condition of Eq. 3.1 for σ on S reads:

$$\sigma_{ij} n_j = 0 \tag{3.2}$$

where n_j are the components of the outer normal to S. For Problem II the values of σ on S must satisfy the condition:

$$\sigma_{ij} n_j = F_i \tag{3.3}$$

where F_i are the components of the loads applied on S.

In the linear theory of elasticity the components of σ are connected with the derivative of the displacement through Hooke's law:

$$\sigma_{ij} = \lambda \frac{\partial u_l}{\partial x_l} \delta_{ij} + \mu \left(\frac{\partial u_i}{\partial x_j} + \frac{\partial u_j}{\partial x_i} \right) \tag{3.4}$$

λ and μ are the elastic coefficients, δ is the Kronecker function, and $u_i(x_1, x_2, x_3)$ are the components of the displacement field $\mathbf{u}$. It is nearly impossible to solve analytically the full three-dimensional problem for general three-dimensional boundary conditions. We will make the hypothesis that the external loads applied on the system do not depend on the coordinate x_3. This does not mean that the external forces have no component on x_3, but simply that the load assumes the same values at different heights. In such a simplified situation one can make the reasonable hypothesis that the stress tensor σ and the components of the displacement field $\mathbf{u}$ are independent on x_3 too. Under this hypothesis Eq. 3.4 inserted into Eq. 3.1 splits into two separate equations:

$$\frac{\partial^2 u_3}{\partial^2 x_1} + \frac{\partial^2 u_3}{\partial^2 x_2} = 0 \tag{3.5}$$

$$(\lambda + \mu) \frac{\partial^2 u_j}{\partial x_i \partial x_j} + \mu \frac{\partial^2 u_j}{\partial^2 x_j} = 0 \quad i, j = 1, 2. \tag{3.6}$$

The strain given by the solutions u_3 of the first equation is called *anti-plane strain*, and that of the second equation is called *plane strain*.

3.2.3 The elastic field of a single crack

The Mode III crack

In Mode III the only applied force is in the x_3 direction. In this case it is reasonable to assume that the only non zero component of the displacement field is u_3. This non zero component does not depend on the coordinate x_3, because the load is independent from the height. Thus the only non zero

components of σ are σ_{31} and σ_{32}. It can be shown using Eq. 3.1 that the complex function $\sigma(z)$, where $z = x_1 + ix_2$:

$$\sigma(z) = \sigma_{32} + i\sigma_{31} \tag{3.7}$$

is holomorphic in the complex plane with the cut. The solution of Problem II is found to be:

$$\sigma(z) = \frac{1}{\sqrt{z^2 - a^2}} \int_{-a}^{a} F_{III}(t) \sqrt{\frac{a^2 - t^2}{t - z}} dt \tag{3.8}$$

where $F_{III}(t)$ is the force applied along the contour of the penny crack. Eq. 3.8 is singular at $z = \pm a$, and the expansion of $\sigma(z)$ around the crack tip $z = a$ is:

$$\sigma(z) = \frac{1}{\sqrt{2\pi}} \frac{K_{III}}{\sqrt{(z-a)}} + O\left(\frac{z-a}{a}\right)^{\frac{1}{2}} \tag{3.9}$$

where K_{III} is a factor giving the intensity of the stress field around the crack tip. The general expression for K_{III} is:

$$K_{III} = \frac{1}{\sqrt{\pi a}} \int_{-a}^{a} F_{III} \left(\frac{a+t}{a-t}\right)^{\frac{1}{2}} dt \tag{3.10}$$

and becomes in the case of a constant force F_{III}:

$$K_{III} = F_{III}\sqrt{\pi a}. \tag{3.11}$$

Eq. 3.11 gives a central result in the linear elastic theory of fracture. Around the crack tip the stress distribution is singular and diverges like $1/\sqrt{z}$. The strength K_{III} of the singularity is called the *stress intensity factor*, and depends upon both the crack geometry and the applied load.

The solution for the Problem I is the same as for Problem II provided F_{III} is intended to be the component of the load at infinity.

The Mode I and Mode II crack

The component along x_3 of the forces loading a crack in Mode I and Mode II is always zero. Thus it is reasonable to assume that the sample will not be strained in the x_3 direction, and that u_3 and σ_{32},σ_{33} are identically zero. The non zero components of the stress tensor σ can be expressed in terms of two holomorphic functions $\Phi(z)$ and $\Omega(z)$:

$$\begin{array}{rcl} \sigma_{11}+\sigma_{22} & = & 2[\Phi(z)+\bar{\Phi}(z)] \\ \sigma_{22}-\sigma_{11}+2i\sigma_{12} & = & 2[\bar{z}\Phi'(z)+\Omega(z)] \end{array} \tag{3.12}$$

defined on the complex plane $z = x_1 + ix_2$ with the cut. The explicit expression of $\Phi(z)$ and $\Omega(z)$ is complicated and not important for the scope of this brief review. It will be sufficient to say that, in analogy with Mode III, both $\Phi(z)$ and $\Omega(z)$ diverge like $1/\sqrt{z}$ when z approaches a and $-a$. The expansion of $\Phi(z)$ around a reads for both Problem I and Problem II :

$$\begin{array}{rcl} \Phi(z) & = & \dfrac{\bar{K}}{2\sqrt{2\pi(z-a)}} + O\left(\sqrt{(z-a)/a}\right) \\ K & = & K_1 + iK_2 \end{array} \tag{3.13}$$

and is used to define the stress intensity factors K_1 and $K_2$for Mode I and II. The complex constant K in Problem I depends on the load applied on the crack surface through the formula:

$$\begin{array}{rcl} K & = & \dfrac{1}{\sqrt{\pi a}} \displaystyle\int_{-a}^{a} F(t) \left(\frac{a+t}{a-t}\right) dt \\ F(t) & = & F_I(t) + iF_{II}(t) \end{array} \tag{3.14}$$

where $F_I(t)$ and $F_{II}(t)$ are respectively the x_1 and x_2 components of the load for Mode I and Mode II. When the applied load is constant Eq. 3.14 reads:

$$K = F\sqrt{\pi a}. \tag{3.15}$$

The real and imaginary part of K in Eq. 3.15 define the stress intensity factors for Mode I and Mode II. In complete analogy with Mode III the stress intensity factors for Mode I and Mode II depend linearly on the applied load.

Eq. 3.15 defines the stress intensity factors for Problem II as well, provided that F is intended to be the stress applied at infinity.

3.2.4 The stress intensity factor of a crack with a dislocation distribution

The presence of a dislocation distribution changes the stress field of a crack, and therefore changes its stress intensity factor [53, 56, 57]. We consider a distribution of screw dislocations with dislocation line parallel to the axis x_3. The position of each dislocation is defined by a point in the plane $x_3 = 0$ or equivalently by a complex number ζ in the complex plane $z = x_1 + ix_2$.

Mode III crack

The stress field around the tip of a crack loaded in Mode III in presence of a dislocation distribution has the usual form:

$$\sigma(z)_{z\to 0} = \frac{k_{III}}{\sqrt{2\pi z}} \tag{3.16}$$

but the stress intensity factor reads now:

$$k_{III} = K_{III} - \frac{\mu}{2}\sum_j \left(\frac{b_j}{\sqrt{2\pi\zeta_j}} + \frac{b_j}{\sqrt{2\pi\bar{\zeta}_j}} \right) \tag{3.17}$$

where K_{III} is the stress intensity factor of the crack with no dislocation and b_j is the Burgers vector of the dislocation at the position ζ_j.

Mode I and Mode II crack

In Mode I and II the stress field diverges around the crack tip like Eq. 3.13:

$$\Phi(z)_{z\to 0} = \frac{\bar{k}}{2\sqrt{2\pi z}} \tag{3.18}$$

but the stress intensity factor is modified by the presence of the dislocation as:

$$\bar{k} = \bar{K} - \frac{\mu}{2i(1-\nu)}\sum_j \left(\frac{b_j}{\sqrt{2\pi\zeta_j}} + \frac{b_j}{\sqrt{2\pi\bar{\zeta}_j}} + \frac{\pi\bar{b}_j(\zeta_j - \bar{\zeta}_j)}{(2\pi\bar{\zeta})^{3/2}} \right) \tag{3.19}$$

where K is the complex stress intensity factor defined for the crack with no dislocation in Eq. 3.13. The real part of the complex number b_j is the Burgers vector of the dislocation j interacting with a crack in Mode I. The imaginary part of b_j is the Burgers vector of the dislocation j interacting with a crack in Mode II.

3.2.5 Final remarks

In the previous sections the expressions of the stress intensity factors for constant loads applied to a crack with no dislocations, and the character of the divergence of the stress tensor around the crack tip, have found to be the same for all the modes and for both Problem I and Problem II (cf. Eq. 3.11 and Eq. 3.15). This might seem to be a coincidence but it is not. The stress intensity factors and the stress distribution around the crack tip obey very general principles independently on how the crack is loaded (Mode I,II,II) and where (Problem I and Problem II).

For a distribution of finite cuts in the plane under an uniform (constant) load:

- the stress tensor around the crack tip diverges like $1/\sqrt{r}$, where r is the distance from the tip
- the strength of the divergence is called the *stress intensity factor* and depends linearly on the applied load.

Concerning the interaction of crack and dislocations, two important considerations can be made looking at Eq. 3.17 and Eq. 3.19.

The stress intensity factor of a crack interacting with dislocations having positive Burgers vector is smaller than that of the crack with no dislocation. Dislocations with positive Burgers vector are said to be *shielding* dislocations because their presence weakens the influence of the external field on the crack. On the contrary dislocations with negative Burgers vector enhance the influence of the external field on the crack, and therefore they are said to be *anti shielding* dislocations.

Not only the term ζ_j but also the term $\bar{\zeta}_j$ is present in the expression of the stress intensity factor of a crack interacting with a dislocation. The term $\bar{\zeta}_j$ corresponds to an *image* of the dislocation at ζ_j. The canceling effect of image dislocations makes the dislocation part of stress field decay stronger than the normal $1/z$ field.

3.3 The elastic forces on cracks and dislocations

3.3.1 Introduction

In the linear theory of elasticity the total force $\mathbf{F}_V$ exerted on a closed volume V *inside* an elastic body is:

$$\mathbf{F}_V = \int_S \sigma \cdot \mathbf{n} ds \tag{3.20}$$

where S is the surface of the volume and $\mathbf{n}$ is the outer normal of the surface. The total force $\mathbf{F}_V$ can be written using Stokes theorem as:

$$\mathbf{F}_V = \int_S \sigma \cdot \mathbf{n} ds = \int_V \mathrm{div}\sigma dv \tag{3.21}$$

and in absence of external body forces is zero because $\mathrm{div}\sigma = 0$. If the volume includes *singularities* of the elastic field Stokes theorem does not hold in the form of Eq. 3.21 and thus $\mathbf{F}_V$ might not be zero anymore. An important analog can be found in electromagnetism. The flux of the electric field $\mathbf{E}$ is zero over any closed surface containing no electric charge. But as soon as the volume includes electric charges, which are singularities of the electric field, the flux of $\mathbf{E}$ is not zero anymore.

Cracks and dislocations are singularities of the elastic field. For that reason there is a net force acting on them. Historically the elastic force on a dislocation was worked out for the first time by Peach and Kohler, who found that this force is zero [78]. Irwin derived a similarly classic result for the force on a crack loaded in Mode I in two-dimensional elasticity [45]. Later Eshelby enunciated for the first time a general theorem giving the force on an elastic singularity in terms of the energy momentum tensor of the elastic field [28]. This second approach opened the way to the treatise of the force on an elastic singularity in terms of complex potentials [88, 44]. Some years later Eshelby Rice developed an alternative way to solve the problem based on the the continuum plasticity theory [89, 90, 91], which has become the standard continuum-mechanics approach to cracks in a deformation field.

In the language of the complex potentials the force on a elastic singularity depends on the residue of the singularity in $\sigma(z)^2$. The stress field of a

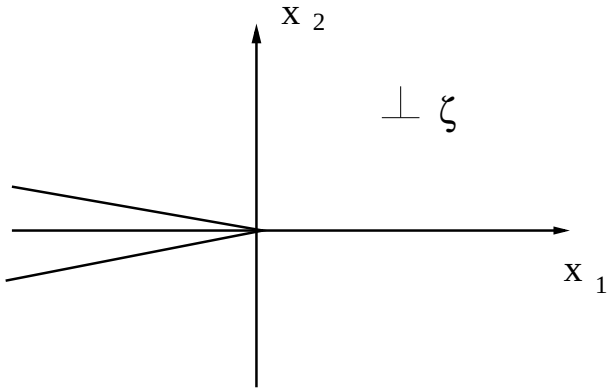

Figure 3.4: *Crack geometry used for calculating the interaction force of a crack with a dislocation. The crack extends indefinitely along the negative x_1 axis and interacts with a dislocation placed at ζ.*

crack around the crack tip is of the form $1/\sqrt{z}$, and the square of such a singularity has a residue which is not zero, and therefore the force on a crack with no dislocations is not zero. The stress field of a dislocation with no crack around the dislocation core has the form $1/z$, and the square of such a singularity contributes no residue. For that reason the force on a dislocation with no crack is zero. In any other mixed situation, crack with dislocation and dislocation with dislocation, the netto force on the singularities is not zero. The goal of this section is that of giving the expression of the such a force.

The geometry considered here is different from that of the other sections. The crack tip is in the origin and the crack surface extends infinitely along the negative x_1 axis (see Fig. 3.4). The crack interacts with a distribution of dislocations intersecting the plane at ζ_j.

3.3.2 Mode III crack

Force on a crack with no dislocation

Let us consider a crack with no dislocation loaded in Mode III. The net force acting on the crack has only a component in the positive x_1 direction whose expression is [94, 95]:

$$f_c = \frac{K_{III}^2}{2\mu} \tag{3.22}$$

and therefore the crack can only open in the positive x_1 direction. The intensity of the force depends quadratically on the stress intensity factor.

Force on a crack with a dislocation distribution

If the crack coexists with a distribution of dislocations at ζ_j the force on the crack tip has again only a component in the positive x_1 direction, and reads [96]:

$$\begin{aligned} f_c &= k_{III}^2/2\mu \\ k_{III} &= K_{III} - \frac{\mu}{2}\sum_j \left(\frac{b_j}{\sqrt{2\pi\zeta_j}} + \frac{b_j}{\sqrt{2\pi\bar{\zeta}_j}} \right) \end{aligned} \tag{3.23}$$

where k_{III} is the modified stress intensity factor of Eq. 3.17.

Force on a dislocation distribution with a crack

The force f_d on the dislocation at ζ_i due to the interaction with the others dislocations and with the crack is[1] [96]:

$$\begin{aligned} f_d = {} & \frac{K_{III} b_i}{\sqrt{2\pi\zeta_i}} - \frac{\mu b_i^2}{4\pi}\left[\frac{1}{2\zeta_i} + \frac{1}{\zeta_i - \bar{\zeta}_i} - \left(\frac{\bar{\zeta}_i}{\zeta_i}\right)^{1/2} \frac{1}{\zeta_i - \bar{\zeta}_i} \right] + \\ \sum_{j\neq i} \frac{\mu b b_j}{4\pi} & \left[\frac{1}{\zeta_i - \zeta_j} - \frac{1}{\zeta_i - \bar{\zeta}_j} + \left(\frac{\zeta_j}{\zeta_i}\right)^{1/2} \frac{1}{\zeta_i - \zeta_j} + \left(\frac{\bar{\zeta}_j}{\zeta_i}\right)^{1/2} \frac{1}{\zeta_i - \bar{\zeta}_j} \right] \end{aligned} \tag{3.24}$$

Three types of terms are contained in Eq. 3.24.

The first term is the direct crack-dislocation interaction. This term may be attractive or repulsive, depending on the sign of the Burgers vector, and

[1] It is worth to remember that f_d is in general a complex number and the force on the dislocation has two non zero components in (x_1, x_2)

goes like $1/\sqrt{r}$, where r is the distance between the crack tip and the dislocation core.

The second term contains expressions like $\bar{\zeta}$ and is relative to the self-image interaction. The force due to the interaction of the dislocation with its self-image depends only on the Burgers vector b_i, and varies with the distance from the crack tip as $1/r$.

The third group of terms describes the dislocation-dislocation interaction. In addition to the terms like $1/(\zeta_i - \zeta_j)$, which give the pure direct interaction of the dislocations, there are contributions from dislocations at the image points $\bar{\zeta}_j$ caused by the open surfaces. The sign of the force is linear in b_i in the first term, bilinear in the second and quadratic in the last. The force can thus be attractive or repulsive in the first or third term, but is always attractive for the self-image term.

3.3.3 Mode I and Mode II crack

The expressions for Mode I and Mode II cracks are much more complicated than for Mode III. The force on the crack and on a dislocation in the general case of a dislocation distribution is very complicated. The reader can find a detailed treatise of such a case in [96].
Here some simplifying assumptions are made:

- Only the interaction of a crack with a *single edge* dislocation is considered.
- The slip plane of the dislocation intersects the crack tip (case of the *emitted* dislocation -see Fig. 3.5).

Force on a crack with no dislocation

For the crack with no dislocation the force f_c on the crack tip is [9, 21, 22]:

$$\begin{aligned} f_c &= \frac{1-\nu}{2\mu}\left(K\bar{K} + \frac{K^2 - \bar{K}^2}{2}\right) \\ K &= K_I + iK_{II} \end{aligned} \tag{3.25}$$

in components:

$$\begin{aligned}(f_c)_1 &= \frac{1-\nu}{2\mu}(K_I^2 + K_{II}^2) \\ (f_c)_2 &= -\left(\frac{1-\nu}{\mu}\right) K_I K_{II}\end{aligned} \tag{3.26}$$

where ν is the Poisson module. For pure Mode I and Mode II the only non zero component of f_c in Eq. 3.25 is on x_1, and in this case the crack can propagate only in the x_1 direction. For a mixed situation the force on the crack has a component in the x_2 direction which might account for a branching of the crack away from the cleavage plain.[2]

Force on a crack with a dislocation

When the crack coexists with a dislocation placed at ζ with Burgers vector b, the force on the crack is the same as the one in Eq. 3.25 and Eq. 3.26, provided that the stress intensity factor K is replaced by the expression k [96]:

$$\bar{k} = \bar{K} + \frac{\mu}{2i(1-\nu)}\left(\frac{b}{\sqrt{2\pi\zeta}} + \frac{b}{\sqrt{2\pi\bar{\zeta}}} + \frac{\pi\bar{b}(\zeta-\bar{\zeta})}{(2\pi\bar{\zeta})^{3/2}}\right) \tag{3.27}$$

General form of the force on a dislocation

The force on the dislocation is the sum of two contributions: the direct crack-dislocation interaction, and the interaction of the dislocation with its self image [96].

The slip plane of the dislocation intersects the crack tip forming an angle θ with the x_1 axis. The force on the dislocation interacting both the with the crack and with its self-image, can be decomposed into two components f_{slip} and f_{climb} (see Fig. 3.5). The component f_{slip} is in the direction of the slip plane, and is the force changing the relative distance between the crack tip and the dislocation core. The component f_{climb} is perpendicular to the slip plane, and this force tries to let the dislocation leave the slip plane.

[2] A more careful analysis of the branching force made in [22] shows that the expression of Eq. 3.26 is only an approximated form of the force needed to let a crack branch.

Force on a dislocation with a crack

The direct crack-dislocation force has only a component f_{slip} on the slip plane which reads [96]:

$$f_{slip} = \frac{b}{2\sqrt{2\pi r}} \left[K_I \sin(\theta) \cos(\theta/2) + K_{II} (2 \cos(3\theta/2 + \sin(\theta) \sin(\theta/2))) \right] \tag{3.28}$$

The force of Eq. 3.28 is repulsive for positive Burgers vectors and attractive for negative values of b, and goes like $1/\sqrt{r}$, where r is the distance between the crack tip and the dislocation core.

The self-image force on a dislocation

The force exerted on the dislocation by its self image has both the components f_{slip} and f_{climb}, whose explicit expressions are:

$$\begin{aligned} f_{slip} &= -\mu |b^2| / 4\pi(1-\nu) r \\ f_{climb} &= \frac{\mu b^2 \tan(\theta/2)(5 + 3\cos(\theta))}{16\pi(1-\nu) r^2} \end{aligned} \tag{3.29}$$

3.3.4 The Griffith criterion

Linear theory of elasticity is a quite straightforward working tool. For any given value of the applied load all the expressions of the previous sections give the force applied on the crack and on the dislocations present in the material. In the limit of applicability of the theory, the material is supposed to be in equilibrium, and it is implicitly assumed that the forces on the crack and on the dislocations are balanced by the resistance of the material, and therefore no crack can propagate and no dislocation can move. But this is far from being true. Even in the limit of applicability of the theory, i.e. that the system undergoes small strains, there are values of the load beyond which the crack starts to propagate and the dislocations move, i.e. the system breaks. A.A. Griffith has given in 1920 a criterion for the equilibrium of cracks in brittle materials [5].

Let us consider a crack loaded in Mode I in a material with no dislocations. The elastic force on the crack is:

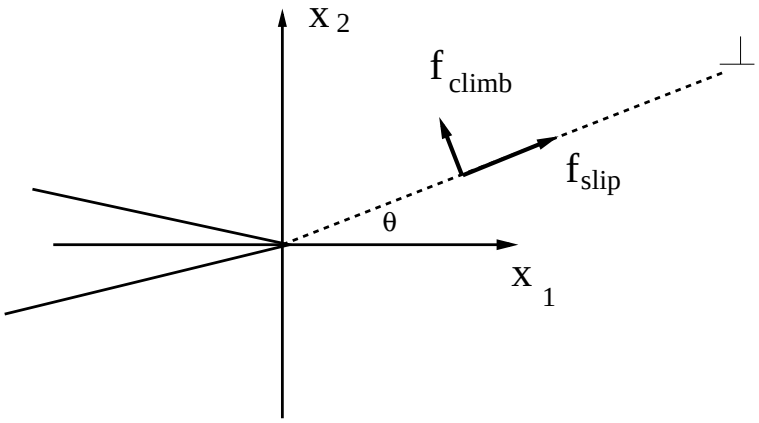

Figure 3.5: *Dislocation emitted from the crack tip. The slip plane forms an angle θ with the x_1 axis. The force on the dislocation has two components f_{slip} and f_{climb}. The components f_{slip} is in the direction of the slip plane, whereas f_{climb} is perpendicular to the slip plane.*

$$f_c = \frac{(1-\nu)}{2\mu} K_I^2 \tag{3.30}$$

and it is balanced by the resistance of the material as long as f_c is smaller than the force f_s needed to open a new surface. The value of the surface force depends on the surface tension γ like[3]:

$$f_s = -2\gamma. \tag{3.31}$$

Equilibrium is realized when the elastic force and the surface tension are in balance:

$$K_I = 2\sqrt{\gamma\mu(1-\nu)}. \tag{3.32}$$

Eq. 3.32 is called the *Griffith relation*. In general the Griffith point is unstable, but there are some loading conditions and particular crack geometries for which the Griffith point is stable.

[3]The crack must open two new surfaces when it starts to propagate, and then f_s must be two times the surface tension.

The instability at the Griffith value is the reason why fracture is often a catastrophic event. When the load applied to the system goes beyond the Griffith value nothing can be done to stop the crack. The instability in the other direction, the closure of the crack, is normally not observed in experiments. When a new surface is formed oxide formation or irreversible deformations are effects which change the morphology of the material and hinder the closure of the crack.

3.3.5 Elastic estimates for dislocation emission

When a crack is loaded enough to initiate cleavage it is often in the regime of spontaneous dislocation emission from the crack tip [3, 66]. Which event occurs first depends on the strength of the material against shear or fracture. By elastic means it is possible to give a rough criterion for dislocation emission or fracture cleavage.

Let us consider a crack loaded in Mode I, and a dislocation emitted from the crack tip. It is supposed that the total force f_d on the dislocation has only a component in the slip plane[4], and is the sum of the direct interaction with the crack and with the self-image dislocation:

$$f_d = \frac{b}{2\sqrt{2\pi r}} K_I \sin(\theta)\cos(\theta/2) - \frac{\mu}{4\pi r}\frac{b^2}{1-\nu} \tag{3.33}$$

According to Eq. 3.33 f_d is attractive for values of r smaller than r_0, and repulsive for values of the distance bigger then r_0, where r_0 is the radius at which the force is zero (see Fig. 3.6). In the approach of the continuum theory the dislocation core has no finite dimension, and thus a crack will always be stable against dislocation emission. As soon as a dislocation is forming closed to the crack tip it would feel a very strong attractive force which brings the dislocation back to tip. In reality a dislocation has a core of finite size. The core of a dislocation is the region where the elastic approximation breaks down. If the size of the dislocation core is equal or bigger then r_0 dislocation emission will always take place spontaneously. When the emitted dislocation is well formed it will already be outside the attractive region and it will feel only the repulsive force. If the core dimension r_c of the dislocation is known

[4]This is actually the case in quasicrystals, where the emitted dislocation cannot leave the slip plane, and therefore in this case f_{climb} must be considered as zero.

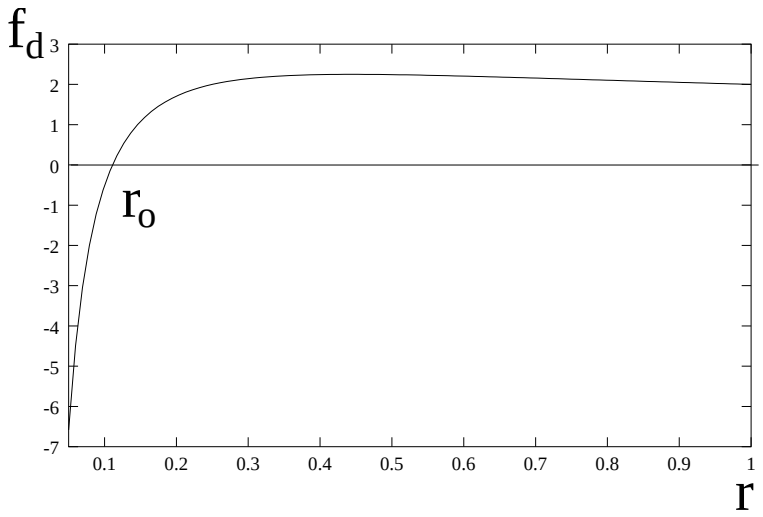

Figure 3.6: *Force exerted on a dislocation emitted from the crack tip. r_o is the distance at which the force is zero.*
.

Eq. 3.33 can give the value K_{IE} of the stress intensity factor, and thus indirectly of the external load, at which spontaneous dislocation emission takes place:

$$K_{IE} = \frac{\mu}{\sqrt{2\pi r_c}} \frac{b(1-\nu)}{\sin(\theta)\cos(\theta/2)}. \tag{3.34}$$

The Griffith criterion for cleavage gives a value K_{IC} of the stress intensity factor:

$$K_{IC} = 2\sqrt{\mu\gamma(1-\nu)} \tag{3.35}$$

and the combined criterion for cleavage/emission in pure Mode I then becomes [72]:

$$\begin{array}{rcll} K_{IE} & < & K_{IC} & emission \\ K_{IE} & > & K_{IC} & cleavage \end{array} . \tag{3.36}$$

If the external load necessary for dislocation emission to take place is smaller than that for cleavage, no fracture propagates and only dislocation emission will take place. In contrast if $K_{IE} > K_{IC}$ as soon as a dislocation is formed it is immediately absorbed and fracture propagates without emitting dislocations.

3.3.6 Final remarks

The elastic force f_c on a crack depends always quadratically on the stress intensity factor K:

$$f_c \approx K^2 \tag{3.37}$$

both for a crack with no dislocation and in the presence of a dislocation distribution, provided that in the latter case the expression of the stress intensity factor is replaced by the shielded or anti-shielded expression of Eq. 3.17 and Eq. 3.27.

The force on a dislocation with a crack and a dislocation distribution is the sum of two terms. The force f_{dc} due to the interaction with the crack is:

$$f_{dc} \approx \frac{Kb}{\sqrt{r}} \tag{3.38}$$

where K is the stress intensity factor of the crack with no dislocation, b is the Burgers vector and r is the distance of the crack tip from the dislocation core. The interaction f_{dd} of the dislocation with both other dislocations and the self-images goes like:

$$f_{dd} \approx \frac{b_1\, b_2}{r} \tag{3.39}$$

where b_1 and b_2 are the two Burgers vectors and r is the distance between the dislocation cores.

A criterion has been proposed by Griffith under which it is possible to estimate the load beyond which a crack start to propagate. The critical load f_{crit} is found to be:

$$f_{crit} \approx \sqrt{\gamma} \tag{3.40}$$

where γ is the surface tension. The constant of proportionality depends only on the elastic constants of the material.

3.4 Atomistic models for crack propagation

3.4.1 Introduction

An atomistic model for crack propagation describes the propagation of a crack at the level of the atomic motion [35, 36, 37]. In the end a crack can move forward only by breaking atomic bonds, and a macroscopic theory like the theory of elasticity is not well suited to account for such a process, which takes place at a time and space scale far beyond the limit of applicability of the continuum model.

The simplest atomistic model of crack is shown in Fig. 3.7 [71]. Two lines of N equally spaced atoms each, are placed at a distance equal to the separation between the atoms. Elastic springs of identical elastic constants of value one tie each atom with its three nearest neighbors. If the distance between two atoms exceeds a certain limit the bond breaks. Unbreakable weak elastic springs whose elastic constant is $1/N$ tie each atom of the line to the floor and the ceiling. The distance between the ceiling and the floor is δ. Increasing δ beyond the critical value δ_c the crack should theoretically start to propagate.

In such a very simplified model two important effects, observed in any atomistic model regardless of its complexity, can be explained: the lattice trapping and the velocity gap.

3.4.2 Lattice trapping

For every value of the distance between the ceiling and the floor greater than critical value δ_c the crack should be in an unstable situation and should start to propagate. This is not the case. There is a range of values of δ beyond but close to the critical one, at which the crack does not propagate. The crack is said to be *trapped* [87]. To understand the origin of the lattice trapping let us imagine to set δ exactly equal to the critical value. The crack is in principle

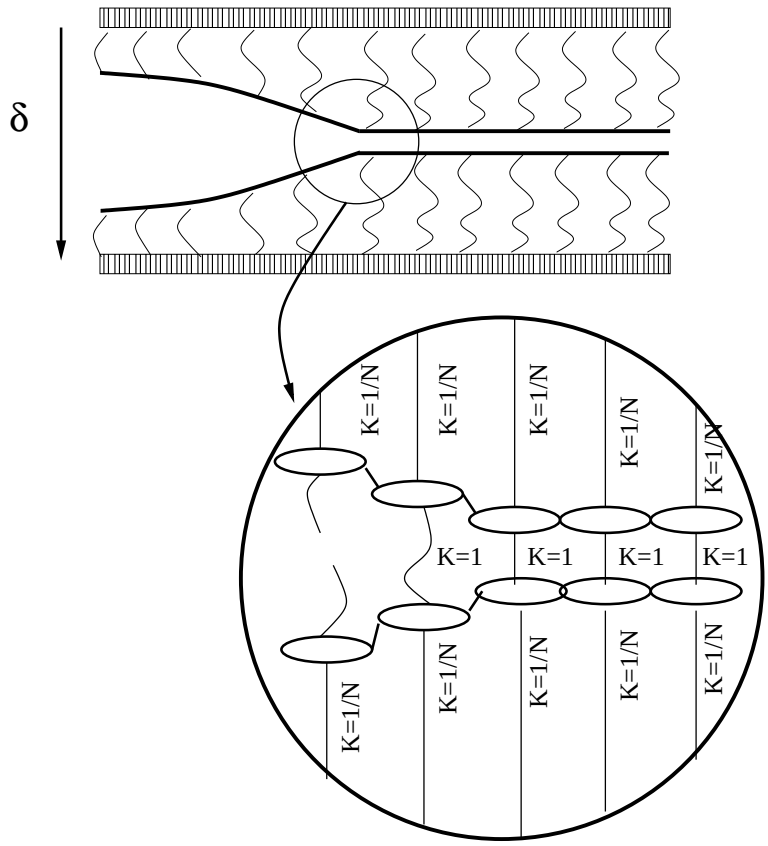

Figure 3.7: *Two lines of N equally spaced atoms each, are placed at a distance equal to the separation between the atoms. Elastic springs of identical elastic constants of value one tie each atom with its three nearest neighbors. Unbreakable weak elastic springs whose elastic constant is $1/N$ tie each atom of the line to the floor and the ceiling. The distance between the ceiling and the floor is δ.*

in an unstable equilibrium situation. Let us imagine to increase δ just a little. Some bonds may break and during the breaking process the atoms forming the just broken bonds move up and down generating high frequency waves. These high frequency waves carry energy away much faster than the next bond can break, and at the crack tip there is no more available elastic energy for the crack to propagate further. One has to slowly keep pulling the ceiling and the floor apart, until the needed energy becomes available and the bond at the tip reaches its breaking point again. Scaling δ by δ_c and defining the variable:

$$\Delta = \frac{\delta}{\delta_c} \tag{3.41}$$

it has been found that even in the limit $N >> 1$, lattice trapping persists until $\Delta = (\sqrt{3}+1)/\sqrt{2} = 1.9$.

3.4.3 Velocity gap

The velocity gap is a consequence of the rapid bonds snapping and it is the dynamical counterpart of the lattice trapping [71].

Dynamic fracture is a cascade of bonds breaking, one giving way after another. The atom which has just broken a bond has an energy excess. This energy excess can be lost in two ways. One possibility is just to disperse this energy in phonons, which are lattice vibrations. Another possibility is to pass this energy to a nearest neighbor atom, which uses this energy excess to break another bond and to form another crack surface. Which possibility takes place depends on the ratio of the time τ_{bond} needed to break a bond, which is the period for the forces between nearest neighbors to fall to zero, and the vibrational period τ_{vibr}. The bigger τ_{bond}/τ_{vibr} the longer the atom vibrates increasing the probability that the energy excess is dispersed in phonons. To quantify this idea let K_{eff} be the effective spring constant of the force acting on an atom which has just broken a bond. The oscillatory period of the atom is:

$$\tau_{vibr} = 2\pi\sqrt{m/K_{eff}} \tag{3.42}$$

where m is the atom mass. If the next bond at a distance a breaks after some fraction α of τ_{vibr}, the crack velocity is:

$$v = (a/\alpha\pi)\sqrt{K_{eff}/m}. \tag{3.43}$$

It is impossible to change K_{eff} by increasing the load applied to the boundary and thus the velocity of Eq. 3.43 represents a lower bound for the crack velocity.

3.4.4 Crack tip instabilities

Smooth and steady state crack motion is limited to a finite range of loads [71]. Once the load becomes too large the vibrations needed to dissipate the energy excess become so big that they can break bonds off the main crack line. What is observed is in general new crack formation, dislocation emission, void formation, and in this case the crack velocity reaches a limiting value. In the second part of this work a big part is devoted to crack tip instabilities of fracture propagation in quasicrystals.

3.5 Experimental results of crack propagation in an icosahedral quasicrystal

This section deals with the experimental results of crack propagation in an icosahedral three-dimensional quasicrystal, and it might be the appropriate end of a chapter about theory of fracture. In Section 8.6 on page 169 some of the results outlined here will be discussed and compared with the numerical results of the molecular dynamics propagation simulations performed in a binary system derived from a Tübingen triangle tiling.

Crack propagation near microhardness indentations on surfaces of an icosahedral $Al_{70}Pd_{23}Mn_7$ single quasicrystal exhibiting fivefold and twofold symmetry has been studied under ambient conditions at room temperature [23, 11, 12].

From an Al-Pd-Mn single quasicrystal a cube-shaped sample of edge length about 5mm was cut. Surfaces perpendicular to fivefold as well as twofold directions have been investigated varying both the rotation angle of the indenter around the surface normal and the force applied perpendicular to the surface. For inspection of the hardness impressions an optical, an atomic force microscope and a laser scan microscope were used.

Microcracks originating from the hardness impressions have been observed at all applied load levels. The number of cracks and their final direction seem to be stable for a given indenter-to-sample orientation but vary considerably if this orientation is changed, because the indenter tip is not isotropic. In order to overcome the indenter anisotropy many experiments have been performed at the same load but with a different indenter orientation around the sample surface normal. With this procedure a series of indentations at a constant load value with *isotropic* indenter orientation distribution has been performed. The resulting crack orientation distribution will now be sample specific rather than indenter induced.

According to atomic force microscopy (AFM) studies the surface near the crack tip appears to be strained in a shear like mode parallel to a cleavage plane, meaning that the cracks propagate in Mode III. The distribution of the cracks directions at a constant load shows that both on a fivefold and twofold surface the cracks tend to propagate parallel to planes of crystallographic symmetry. That means for example that when a crack propagates on a surface of fivefold symmetry strong meandering with angles of $n \times 36^o$ between the parts of the crack is found.

When applying high indentation forces (20 N Rockwell indentation) hundreds of craters nucleate along a crack path and partially grow together, finally causing the sample to break into pieces for forces higher than 50 N.

The approach of the continuum theory to the statics and dynamics of a crack involves elastic energies, which are equal to free energy differences in a system at constant temperature. In Chapter 7 are reported original free energy calculations used to compute the surface energies, the elastic constants and the critical displacements involved in crack propagation. The next chapter gives a short review of the basic notions of classical statistical mechanics, and introduces the theory of the techniques for simulating a system at constant temperature and for computing free energy differences, which have been used to compute the numerical results of Chapter 8.

Chapter 4

EQUILIBRIUM MOLECULAR DYNAMICS

4.1 Introduction

Equilibrium statistical mechanics is a very well known and developed theory. This theory links the macroscopic thermodynamic observables of a system to its microscopic properties. Molecular dynamics simulations may nowadays well describe the microscopic behavior of even very complex systems, becoming therefore more and more an "indispensable" tool of statistical mechanics in many cases of practical interest.

In Section 4.2 of this chapter we will give a short review of the basic notions of statistical mechanics. We will summarize some aspects which are of interest for the molecular dynamics simulations. In sections 4.3 and 4.4 a brief report of the most popular molecular dynamics technique for systems at statistical equilibrium will be presented. The Nosé and the Nosé-Hoover thermostat will be described in detail. Section 4.5 describes how to optimize the mass of the Nosé-Hoover thermostat, which is a free parameter of the Nosé-Hoover dynamics. Section 4.6 contains some methods for free energy calculations via a molecular dynamics simulation. Section 4.7 gives a short explanation of the numerical methods used to solve the Hamiltonian and Nosé-Hoover equations of motion.

4.2 Basic notions of statistical mechanics

Let us consider a classical system of N particles. Of every particle the position $\tilde{q}_i$ and the momentum $\tilde{p}_i$ are known, where $i = 1, \ldots, N$.

The motion of the system as a whole takes place in a *phase space*, whose points $\tilde{x}$ are:

$$\tilde{x} = (q_1, \cdots, q_N, p_1, \cdots p_N) = (\tilde{q}, \tilde{p}). \tag{4.1}$$

Even if N is small, in the cases of practical interest it is almost always impossible to solve analytically the equations of motion of the system. We can only *observe* the evolution of $\tilde{x}$, and this is the starting point of statistical mechanics.

Let us consider the motion of the system over a time T and focus our attention on a neighborhood of a point $(\tilde{q}, \tilde{p})$, where we can find the system for a time ΔT.
If the system during the motion

- is sufficiently chaotic to be able of forgetting its initial condition
- is able to visit *every accessible* point of the phase space

it is said to be *ergodic*[1][60]. Under such circumstances the ratio $\Delta T/T$ for longer and longer time T becomes more and more independent of the initial conditions. We can thus define a density of probability ρ of finding the system in a neighborhood of a point like [39]:

$$\rho(\tilde{q}, \tilde{p}) d\tilde{q} d\tilde{p} = \lim_{T \to \infty} \frac{\Delta T}{T}, \tag{4.2}$$

and in this formalism the mean value $\langle f \rangle$ of an observable $f(\tilde{q}, \tilde{p})$:

$$\langle f \rangle = \int f(\tilde{q}, \tilde{p}) \rho(\tilde{q}, \tilde{p}) d\tilde{q} d\tilde{p} \tag{4.3}$$

can be evaluated over the trajectory of the system as:

[1] Ergodicity is a synonym for statistical equilibrium.

$$\langle f \rangle = \lim_{T\to\infty} \frac{1}{T} \int_0^T f(\tilde{q}(t), \tilde{p}(t))dt. \tag{4.4}$$

Let us now consider a dynamical system with a time-independent Hamiltonian $H(\tilde{q}, \tilde{p})$.

We say that the system realizes a *microcanonical* distribution in the phase space if its motion takes place on a manifold of the phase space having a given energy E. In this case ρ can be written as:

$$\rho(\tilde{q}, \tilde{p}) = \delta(H(\tilde{q}, \tilde{p}) - E) \tag{4.5}$$

For a dynamical system whose Hamiltonian is time independent the solution of the Hamiltonian equations of motion:

$$\begin{cases} \frac{dq_i}{dt} &= \frac{\partial H}{\partial p_i} \\ \frac{dp_i}{dt} &= -\frac{\partial H}{\partial q_i} \end{cases} \tag{4.6}$$

forces the system to stay on the manifold $H(\tilde{q}, \tilde{p}) = H_0$, where H_0 is the initial energy, and thus during its motion the system realizes the microcanonical distribution.

A system at a given temperature T is at thermodynamical equilibrium if during its motion it spans the phase space according to the *canonical* Boltzmann distribution:

$$\rho(\tilde{q}, \tilde{p}) = \frac{\exp(-H(\tilde{q}, \tilde{p})/KT)}{\int \exp(-H(\tilde{q}, \tilde{p})/KT) d\tilde{q}d\tilde{p}}. \tag{4.7}$$

where K is the Boltzmann constant. In analogy with the microcanonical case, the question is now whether it is possible to find a dynamics of the system such that the probability defined in Eq. 4.2 is the canonical one. The Hamiltonian dynamics of Eq. 4.6 describes an isolated system, which thus +can not posses a constant thermodynamic temperature. If we want a *single* system to visit the accessible points of the phase space according

to the Boltzmann distribution, we must couple the system to some external force being able to change the total energy. Historically many attempts have been proposed [30, 40, 7], but only Nosé and Hoover have proposed two modifications of the Hamiltonian equations of motion which reproduce the canonical distribution.

4.3 The Nosé thermostat

The approach of Nosé in his seminal paper [83, 85] is to extend the canonical system of the $\tilde{q}, \tilde{p}$ with two other conjugated degrees of freedom. In the extended system a new Hamiltonian H' is written:

$$H' = \sum_{i=1}^{N} \frac{p_i^2}{2m_i s^2} + V(\tilde{q}) + \frac{p_s^2}{2Q} + (f+1)KT \log s \tag{4.8}$$

where:

- p_s and s are the two new conjugated variables. s plays the role of a position and p_s that of a momentum.
- V is the potential of the system.
- Q is a free parameter
- f is the number of degrees of freedom of the system.

The Hamiltonian equations of motion of the system are:

$$\begin{cases} \dot{q}_i &= & p_i/m_i s^2 \\ \dot{p}_i &= & \partial V/\partial q_i \\ \dot{p}_s &= & \sum_{i=1}^{N} p_i^2/m_i s^3 - KT(f+1)/s \\ \dot{s} &= & p_s/Q \end{cases} \tag{4.9}$$

On a trajectory solution of Eq. 4.9 for given initial conditions, the mean value of a quantity $A(\tilde{p}/s, \tilde{q})$ can be written as:

$$\langle A(\frac{\tilde{p}}{s},\tilde{q})\rangle = \frac{\int A(\tilde{p}/s,\tilde{q})\delta(H'-E)d\tilde{q}d\tilde{p}dp_s ds}{\int \delta(H'-E)d\tilde{q}d\tilde{p}dp_s ds}. \tag{4.10}$$

Using the transformation:

$$p_i' = \frac{p_i}{s} \tag{4.11}$$

and the properties of the δ:

$$\delta(g(x)) = \frac{\delta(x-x_0)}{g'(x)} \qquad g(x_0)=0 \tag{4.12}$$

for the function:

$$g(s) = \sum_{i=1}^{N} \frac{{p_i'}^2}{2m_i s^2} + V(\tilde{q}) + \frac{p_s^2}{2Q} + (f+1)KT\log s - E, \tag{4.13}$$

the mean value of A can be rewritten as:

$$\langle A(\frac{\tilde{p}}{s},\tilde{q})\rangle = \frac{\int A(\tilde{p}',\tilde{q})\exp\left(-\frac{1}{KT}\left[\sum \frac{p_i'}{2m} + V(\tilde{q})\right]\right)d\tilde{p}'d\tilde{q}}{\int \exp\left(-\frac{1}{KT}\left[\sum \frac{p_i'}{2m} + V(\tilde{q})\right]\right)d\tilde{p}'d\tilde{q}}. \tag{4.14}$$

The right side of Eq. 4.14 is the mean value of $A(\tilde{p}',\tilde{q})$ over the canonical ensemble. The Nosé dynamics in the extended space may then be used to compute static canonical mean values in the space of the $\tilde{q},\tilde{p}$. It is important to notice that the only dependence on E is the left side of Eq. 4.14. This means that the canonical mean value of an observables can be calculated on every trajectory solution of the Nosé equations of motion, independently of the initial condition.

4.4 The Nosé-Hoover thermostat

Under the *non canonical* change of variables:

$$\begin{cases} t' & = & \int^t \frac{d\nu}{s} \\ p'(t') & = & \frac{p(t)}{s(t)} \\ s'(t')) & = & s(t) \\ \dot{p}'_s & = & \frac{p_s(t)}{s(t)} \end{cases} \tag{4.15}$$

applied to Eq. 4.8 where f is replaced with $f - 1$[2], Hoover obtained the equations of motion [43, 26, 84]:

$$\begin{cases} \dot{q}_i & = & \frac{\dot{p}_i}{m_i} \\ \dot{p}_i & = & -\frac{\partial V}{\partial q_i} - p_i\eta \\ \dot{\eta} & = & \frac{1}{Q}\left[\sum_{i=1}^{N} \frac{p_i^2}{m_i} - fKT\right] \end{cases} \tag{4.16}$$

In Eq. 4.16 the variables p_s and s disappeared, replaced by η, where:

$$\begin{cases} \eta & = & \frac{ps}{Q} \\ \frac{1}{s}\frac{ds}{dt} & = & \eta \end{cases} \tag{4.17}$$

In the literature the equations 4.16 may appear under a slightly different form:

[2]There is no reason a priori why f should be replaced with $f-1$. It is just a trick with which everything works.

$$\begin{cases} \dot{q}_i &= \dfrac{p_i}{m_i} \\ \dot{p}_i &= -\dfrac{\partial V}{\partial q_i} - \nu\eta p_i \\ \dot{\eta} &= \nu\left[\dfrac{T(t)}{T} - 1\right] \end{cases} \tag{4.18}$$

where $T(t)$ is the instantaneous temperature, defined in a system with d spatial dimensions as:

$$T(t) = \frac{1}{dNKT}\sum_{i=1}^{N}\frac{p_i^2}{m_i}. \tag{4.19}$$

The equations 4.18 are known as the *Nosé-Hoover equations of motions*.

It is important to stress that the Nosé-Hoover dynamics is not Hamiltonian. There is no total energy which is conserved during the motion. Nevertheless, there is an integral of motion which is of importance in the applications. The Nosé-Hoover dynamics conserves the quantity $\mathcal{H}$:

$$\mathcal{H} = \frac{1}{N}\sum_{i=1}^{N}\frac{p_i^2}{2m_i} + V(q) + T\eta^2 + 2\nu\int_0^t \eta(\tau)d\tau \tag{4.20}$$

which is the sum of the total energy H of the system, of the work and of the heat the system exchanges during its motion[3].

[3]This can be seen from the differential form of the first principle of thermodynamics applied to Eq. 4.20:

$$dU = \delta Q + \delta W$$

where U is the total energy of the system and W and Q are respectively the work and the heat. Using the time t as parametrisation of the manifold over which the motion takes place, i.e. pulling back the 1-forms dU, δW and δQ, the first principle of thermodynamics reads:

$$\frac{dU}{dt}dt = \frac{\delta Q}{dt}dt + \frac{\delta W}{dt}dt$$

The physical idea behind the Nosé-Hoover equations of motion is quite straightforward and it is based on a *feed-back* mechanism. The system is perturbed by a viscous term ηp_i, and the viscosity coefficient η is time-dependent. If the punctual temperature $T(t)$ is bigger than the equilibrium value T, the viscosity increases, brakes the system and reduces $T(t)$. If $T(t)$ is smaller than T the viscosity decreases, the system is accelerated and the punctual temperature increases. More formally under the reasonable hypothesis that η remains bounded, the Nosé-Hoover equations of motion guarantee that the mean value of $T(t)$ is T. In this case the mean value of $\dot{\eta}$ is zero[4]:

$$\langle \dot{\eta} \rangle = \nu \left(\frac{\langle T(t) \rangle}{T} - 1 \right) = 0 \tag{4.21}$$

and thus $\langle T(t) \rangle = T$.

But this is not yet the solution of the problem. Eq. 4.21 only proves that the *first momentum* of the temperature distribution out of a Nosé-Hoover dynamics equals the theoretical one, but nothing more is said about all the others. To prove that a Nosé-Hoover dynamics reproduces the Boltzmann

The differential $d\mathcal{H}$ is:

$$\frac{d\mathcal{H}}{dt}dt = \frac{d}{dt}(U + T\eta^2 + 2\nu \int_0^t \nu dx)dt = (\frac{dU}{dt} + 2T\dot{\eta}\eta + 2\nu\eta)dt$$

and the condition $d\mathcal{H} = 0$ imposes that:

$$\frac{dU}{dt}dt = -2T\dot{\eta}\eta dt - 2\nu\eta dt$$

which can be integrated to give:

$$W + Q = T(\eta^2(t_2) - \eta^2(t_1)) + 2\nu \int_{t_1}^{t_2} \nu dv$$

[4]The mean value of the derivative of a quantity $\eta(t)$ which remains bounded is always zero. This can be readily seen form the definition of the mean value of $\dot{\eta}$:

$$\langle \dot{\eta} \rangle = \lim_{t\to\infty} \frac{1}{t} \int_0^t \dot{\eta} = \lim_{t\to\infty} \frac{1}{t}(\eta(t) - \eta_0) = 0$$

distribution, more sophisticated tools must be used. The dynamics of Eq. 4.18 leads to a distribution ρ in the phase space which is a solution of the Liouville equation:

$$\frac{\partial \rho}{\partial t} = -(\nabla \cdot \dot{x})\rho \tag{4.22}$$

where in this extended phase space:

$$\begin{cases} \nabla \cdot & = & \sum \dfrac{\partial}{\partial p_i} + \dfrac{\partial}{\partial q_i} + \dfrac{\partial}{\partial \eta} \\ \dot{x} & = & (\dot{p}_1, \cdots, \dot{p}_N, \dot{q}_1, \cdots, \dot{q}_N, \dot{\eta}) \end{cases} \tag{4.23}$$

In the steady-state case, which is the state in which the system is at the statistical equilibrium, the Liouville equation for the Nosé-Hoover equations can be written as:

$$\nu \left[\frac{T(t)}{T} - 1 \right] \frac{\partial \rho}{\partial \eta} + (-dN\nu\eta)\rho + \sum_{i=1}^{N} \left[-\frac{\partial V}{\partial q_i} - \nu\eta p_i \right] \frac{\partial \rho}{\partial p_i} + \frac{p_i}{m} \frac{\partial \rho}{\partial q_i} = 0 \tag{4.24}$$

which is readily solved by the canonical distribution function in the extended phase space:

$$\rho(\tilde{q}, \tilde{p}, \eta) = const \ \exp\left(-\frac{1}{KT} \left[\sum_{i=1}^{N} \frac{p_i^2}{2m_i} + V + \frac{d}{2} NKT\eta^2 \right] \right). \tag{4.25}$$

The solution Eq. 4.25 of the Liouville equation in Eq. 4.24 proves that a Nosé-Hoover dynamics may lead to a sampling of the phase space which is the Boltzmann distribution in the $(\tilde{q}, \tilde{p})$ variables.

So far it is has been proved that a Nosé-Hoover trajectory satisfies the necessary conditions to reproduce a canonical distribution in the phase space. But these conditions are not sufficient yet, because nothing has been said about ergodicity. There are no analytical tools by means of which is it possible to prove that a dynamics whatsoever is ergodic. The ergodicity of

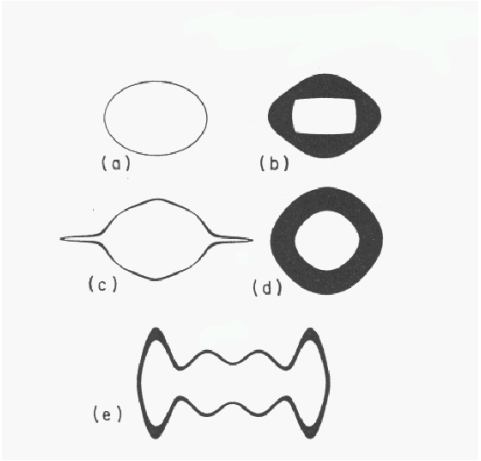

Figure 4.1: *(a) Hamiltonian orbit for a harmonic oscillator. The abscissa is q and the ordinate is p. (b) Long time qp trajectory for the Nosé dynamics with $q = 1, p = 1, s = 1, p_s = 0$ and $Q = 1$. (c) Same as (b) with $Q = 0.1$. (d) Long time qp trajectory for the Nosé-Hoover dynamics with initial values $q = 1, p = 1, \eta = 0$ and $\nu = 1$. (e) Same as (d) with $\nu = 0.1$.*

a Nosé-Hoover dynamics depends essentially on the potential V and on the free parameter ν .

A situation in which the potential plays a central role in the non-ergodicity of the dynamics, is represented in Fig. 4.1, where the Nosé and the Nosé-Hoover dynamics of a one dimensional harmonic oscillator are depicted in the pq phase space. In this simple case $\rho(p, q)$ is Gaussian both in p and in q. The origin should thus be the point around which the probability of findig the system is at the biggest. This is not the case: independent of the value of Q and ν both the Nosé and the Nosé-Hoover dynamics fails to sample correctly the phase space. In this simple case the system remains confined in a small region containing the initial conditions and the system is not ergodic at all. This pathological behavior is typical of situations where the potential V is harmonic. The system is in this case very little mixing, and cannot forget its initial conditions, whatever the value of ν is.

The influence of ν on the ergodicity of the dynamics is more delicate. There are values of ν for which a Nosé-Hoover dynamics is trivially non-ergodic. If ν is given a value close to zero, the term $\nu\eta p_i$ can only weakly

influence the system, or it even disappears. Therefore the Nosé-Hoover equations of motion become the Hamiltonian ones, the system remains close to the manifold of constant energy, and ergodicity is not realized. In the case where ν is given a very large value, η oscillates very fast, because its time derivative is very large. The system of the $(\tilde{q}, \tilde{p})$ has a frequency much smaller than the frequency of η, and cannot react in time to the very fast change of η. The original system can therefore only follow the mean value of η which is zero, and once more the Nosé-Hoover equations of motion become the Hamiltonian ones again. In these two limiting cases the two degrees of freedom η and $(\tilde{q}, \tilde{p})$ split and do not interact with each other. In the language of mechanics the degrees of freedom of the system are said to be *separable*. Separability is a very nice working condition if one aims to find the analytical solution to given equations of motion, but in the case of the Nosé-Hoover dynamics it is the condition under which the system is not ergodic.

The question how to find the best value of ν in practical applications is discussed in the next section.

4.5 Optimizing the mass of the Nosé-Hoover thermostat

In the Nosé-Hoover equations of motion there is always a Toda-demon [97] hidden in the dynamics, which may strongly hinder the system to realize ergodicity over a wide range of ν values. The value of ν at which the influence of the demon is at the smallest is, in systems with periodic boundary conditions, the Einstein frequency w_e [18]. The Einstein frequency w_e is the mean frequency with which an atom of the system oscillates as it were alone under the influence of the mean force of the other atoms. In this model the equation of motion of a single atom is:

$$\ddot{\mathbf{x}} = -\omega_E^2 \mathbf{x} \tag{4.26}$$

where $\mathbf{x}$ is the vector of the coordinates. A straightforward integration of Eq. 4.26 gives as solution:

$$\mathbf{x}(t) = \mathbf{a}\sin(\omega_E t) + \mathbf{b}\cos(\omega_E t) \tag{4.27}$$

where **a** and **b** are two vectors depending on the initial conditions. The mean values of $\dot{\mathbf{x}} \cdot \dot{\mathbf{x}}$ and $\ddot{\mathbf{x}} \cdot \ddot{\mathbf{x}}$ from Eq. 4.27 are:

$$\begin{aligned} \langle \dot{\mathbf{x}}^2 \rangle &= (\mathbf{a}^2 + \mathbf{b}^2)\omega_E^2 \\ \langle \ddot{\mathbf{x}}^2 \rangle &= (\mathbf{a}^2 + \mathbf{b}^2)\omega_E^4 \end{aligned} \tag{4.28}$$

From the theorem of equipartition of the energy the mean value of the velocity is:

$$\frac{1}{2} m \langle \dot{\mathbf{x}}^2 \rangle = \frac{f}{2} KT \tag{4.29}$$

where f is the number of the spatial dimensions, m is the mass of the atom, K is the Boltzmann constant and T is the temperature. From Eq. 4.28 and Eq. 4.29 the Einstein frequency is found to be:

$$\omega_E^2 = \frac{\langle \mathbf{F}^2 \rangle}{fKT} \tag{4.30}$$

where $\langle \mathbf{F}^2 \rangle = m^2(\mathbf{a}^2 + \mathbf{b}^2)\omega_E^4$ is the square of the mean force acting on an atom.

4.6 Free energy calculation

In this section some methods are presented for computing the free energy of a system via molecular dynamics simulations.

Free energy differences, like all the other thermodynamic quantities, can be defined only along a *reversible transformation*. In molecular dynamics a transformation is realized by time-varying some parameters of the system, and the reversibility can be realized under quasi-static working conditions. Typical examples of transformations are dynamics with time varying boundary conditions or time varying potentials. Generally speaking, in a transformation the Hamiltonian $H(t)$ of the system contains an explicit time dependence, and varies from the value H_0 at time t_0 to the value $H_1 = H(t_1)$ at time t_1. The conventional description of such a process uses a time dependent coupling parameter $\lambda(t)$, which varies from 0 at t_0 to 1 at time t_1 [61]. The Hamiltonian $H(t)$ between t_0 and t_1 is formally decomposed as:

$$H(t) = (1 - \lambda(t))H_0 + \lambda(t)H_1 \tag{4.31}$$

If λ varies between t_0 and t_1 sufficiently smooth and slow compared to the characteristic time of the system, the dynamics of the system is quasi-static, and a *reversible* transformation is realized.

4.6.1 Free energy via Nosé-Hoover dynamics .

Let us consider a Nosé-Hoover dynamics where the potential depends explicitly on time. In contrast to the preceding sections we do not consider a single trajectory in phase space but an *ensemble* of trajectories. An ensemble of trajectories is a set of independent Nosé-Hoover dynamics all with different initial conditions. The density of trajectories $\rho(\tilde{q}, \tilde{p}, t)$ in phase space gives the probability of finding a system in a neighborhood of point $(\tilde{q}, \tilde{p})$ at the time t, and when the system is not at equilibrium, i.e. when it undergoes a transformation, $\rho(\tilde{q}, \tilde{p}, t)$ depends explicitly on time .

In a system at thermodynamic equilibrium the entropy is defined as:

$$S = -K \int \log(\rho(\tilde{q}, \tilde{p}))\rho(\tilde{q}, \tilde{p}) d\tilde{q} d\tilde{p} \tag{4.32}$$

where K is the Boltzmann constant and $\rho(\tilde{q}, \tilde{p})$ does not depend on time.

On a transformation we can define formally a quantity $\mathcal{S}$ resembling somehow an "entropy" like [19, 41, 2, 1, 42]:

$$\mathcal{S}(t) = -K \int \rho(\tilde{q}, \tilde{p}, t) \log(\rho(\tilde{q}, \tilde{p}, t)) d\tilde{q} d\tilde{p} \tag{4.33}$$

The quantity $\mathcal{S}(t)$ has in general nothing to do with the thermodynamic entropy of Eq. 4.32: the entropy of a system is a state function intrinsically defined under equilibrium conditions. Nonetheless, on a quasi-static transformation $\mathcal{S}(t)$ of Eq. 4.33 can become a good approximation of the punctual value of the entropy S at time t in Eq. 4.32.

The time derivate of $\mathcal{S}$ is:

$$\dot{\mathcal{S}} = -K \int \frac{\partial}{\partial t} \rho(\tilde{q}, \tilde{p}, t) \log(\rho(\tilde{q}, \tilde{p}, t)) d\tilde{q} d\tilde{p} = -K \int (1 + \log \rho) \frac{\partial \rho}{\partial t} d\tilde{q} d\tilde{p} \tag{4.34}$$

the normalization condition on ρ:

$$1 = \int \rho(\tilde{q}, \tilde{p}, t) d\tilde{q} d\tilde{p} \quad \rightarrow \quad 0 = \int \frac{\partial \rho}{\partial t} d\tilde{q} d\tilde{p} \tag{4.35}$$

and the Liouville theorem applied to Eq. 4.34 give:

$$\dot{\mathcal{S}} = -K \int \log \rho \frac{\partial \rho}{\partial t} d\tilde{q} d\tilde{p} = K \int \log(\rho) \nabla \cdot (\rho \tilde{u}) d\tilde{q} d\tilde{p} \tag{4.36}$$

where $\tilde{u} = d\tilde{x}/dt$ and $\tilde{x} = (\tilde{q}, \tilde{p})$. Integrating by parts two times[5], the time derivative of $\mathcal{S}(t)$ becomes:

$$\dot{\mathcal{S}} = -K \int \tilde{u} \cdot \nabla \rho \, d\tilde{q} d\tilde{p} = K \int \rho \nabla \cdot \tilde{u} \, d\tilde{q} d\tilde{p} \tag{4.37}$$

[5] The identity:

$$\nabla \cdot (\log(\rho) \rho \tilde{u}) = \log(\rho) \nabla \cdot \rho \tilde{u} + \tilde{u} \cdot \nabla \rho$$

can be integrated over a finite closed volume V to give, making use of Stokes's theorem:

$$\int_S \rho \log(\rho) \tilde{u} \cdot \tilde{n} \; ds = \int_V \log(\rho) \nabla \cdot \rho \tilde{u} \; dv + \int_V \tilde{u} \cdot \nabla \rho \; dv.$$

where S is the surface of V and $\tilde{n}$ is the outer normal. Because of the normalization condition on ρ, when V goes to infinity ρ goes to zero on the surface. The integral over S disappears, and we obtain the final formula:

$$\int \log(\rho) \nabla \cdot \rho \tilde{u} \, dv = - \int \tilde{u} \cdot \nabla \rho \, dv.$$

where the integration is now performed on the entire phase space.

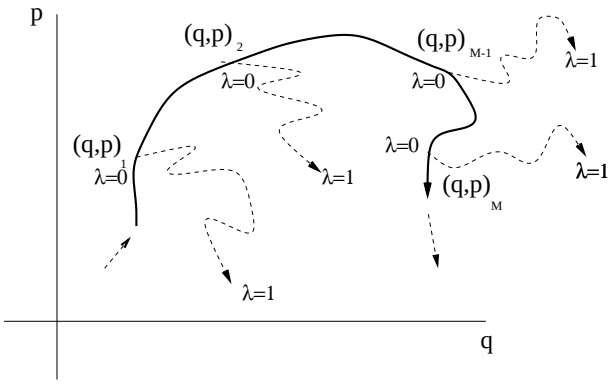

Figure 4.2: *Sketch of the procedure to estimate the time derivative of the entropy via Nosé-Hoover dynamics. The thick line represents a Nosé-Hoover equilibrium dynamics. The points* $(\tilde{q},\tilde{p})_1,\cdots,(\tilde{q},\tilde{p})_M$ *are the initial conditions of a new Nosé-Hoover dynamics, represented by the dashed lines, where at the beginning the parameter* λ *of Eq. 4.31 takes the value 0. On the dashed lines* λ *must change sufficiently smooth and slow. The new dynamics ends when* λ *reaches 1.*

and using Eq. 4.18 on page 75, we obtain finally:

$$\dot{\mathcal{S}} = -dNK\nu \int \eta\, \rho(\tilde{q},\tilde{p},t)\, d\tilde{q}d\tilde{p} = -dNK\langle\eta\rangle_{ens} \tag{4.38}$$

where the mean value $\langle\eta\rangle_{ens}$ is an *ensemble* average, i.e. Eq. 4.38 can give the value of $\dot{\mathcal{S}}$ at time t *if* the value of η at time t can be averaged over the entire phase space. The procedure to estimate the time derivative of the entropy in a molecular dynamics simulation can then be summarized as follow (see Fig. 4.2):

- The first point of every thermodynamic transformation must be at equilibrium. Therefore a set M of points $(\tilde{q},\tilde{p},\eta)_i$, $i = 1, M$ is sampled out of a equilibrium Nosé-Hoover dynamics where $\lambda = 0$.

- The M points are used as initial conditions of M new independent Nosé-Hoover dynamics. The Hamiltonian of the system changes quasi-statically during the motion. The M trajectories of $\eta_i(t)$ are collected.

At every time t the positions of the $\eta_i(t)$ are distributed in the phase space according to the solution $\rho(\tilde{q}, \tilde{p}, t)$ of the time dependent Liouville equation.

- An approximation of Eq. 4.38 on the page before can be given as:

$$\dot{S}(t) \approx \dot{\mathcal{S}}(t) \approx dNK \frac{1}{M} \sum_{i=1}^{M} \eta_i(t) \tag{4.39}$$

and $\dot{S}$ can be integrated in time to give the free energy [6]:

$$F = \langle U \rangle - TS \tag{4.42}$$

where U is the mean value of the internal energy.

4.6.2 Dynamics coupling-parameter methods

The free energy of a system whose Hamiltonian is time-dependent like in Eq. 4.31, can be written as:

[6] The numerical integration of Eq. 4.39 may give a big numerical error if made on the $\eta_i(t)$ *after* the dynamics. It is much better to introduce an additional degree of freedom ξ which slightly modifies the Nosé-Hoover equations of motion as follows:

$$\begin{cases} \dot{q}_i &= \dfrac{p_i}{m_i} \\ \dot{p}_i &= -\dfrac{\partial V}{\partial q_i} - \nu\eta p_i \\ \dot{\eta} &= \nu \left[\dfrac{T(t)}{T} - 1 \right] \\ \dot{\xi} &= \nu\eta \end{cases} \tag{4.40}$$

The entropy can now be immediately expressed as the mean value of ξ:

$$S(t) \approx \mathcal{S}(t) \approx dNK \frac{1}{M} \sum_{i=1}^{M} \xi_i(t) \tag{4.41}$$

The advantage of such an approach is that η is integrated using the same numerical scheme implemented to solve the equations of motion, reducing considerably the numerical errors on S.

$$F = -KT \log \left(\int \exp \left(-\frac{1}{KT} \left[(1-\lambda) H_0 + \lambda H_1 \right] \right) d\tilde{q} d\tilde{p} \right) \tag{4.43}$$

where the integration in Eq. 4.43 is performed over the entire phase space at a *given fixed time*, i.e. for a given value of λ. Formally Eq. 4.43 can be derived with respect to time to give:

$$\frac{dF}{dt} = \frac{\int (H_1 - H_0) \exp \left(-\frac{H(t)}{KT} \right) \frac{d\lambda}{dt} \, d\tilde{q} d\tilde{p}}{\int \exp \left(-\frac{H(t)}{KT} \right) d\tilde{q} d\tilde{p}} = \langle (H_1 - H_0) \rangle_\lambda \frac{d\lambda}{dt} \tag{4.44}$$

where $\langle \rangle_\lambda$ means a mean value for a given *fixed* value of λ. Eq. 4.44 can be time-integrated to give the final formula:

$$F(t) - F(0) = \int_0^t \langle H_1 - H_0 \rangle_\lambda \frac{d\lambda}{d\tau} \, d\tau. \tag{4.45}$$

Often it is not possible to separate in a simple way the time-dependent contribution H_1 in $H(t)$ like in Eq. 4.31 on page 81, and it is only possible to calculate numerically the value of the Hamiltonian $H(\tilde{q}, \tilde{p}, \lambda)$ for a given parameter λ. The derivative of the free energy with respect to λ is now more concisely written as:

$$\frac{dF}{d\lambda} = \frac{\int \frac{\partial H}{\partial \lambda} \exp \left(\frac{-H(\lambda)}{KT} \right) d\tilde{q} d\tilde{p}}{\int \exp \left(\frac{-H(\lambda)}{KT} \right) d\tilde{q} d\tilde{p}} = \langle \frac{\partial H}{\partial \lambda} \rangle_\lambda \tag{4.46}$$

and can be formally integrated to give:

$$F(\lambda) - F(0) = \int_0^\lambda \langle \frac{\partial H}{\partial \lambda'} \rangle_{\lambda'} d\lambda'. \tag{4.47}$$

Free energy differences by means of a dynamic coupling-parameter method may be calculated via a Nosé-Hoover dynamics as follows:

- A value of $\lambda = \hat{\lambda}$ is chosen.
- A set M of points $(\tilde{q}, \tilde{p})_i$, $i = 1, M$ is sampled out of a equilibrium Nosé-Hoover dynamics at $\hat{\lambda}$.
- For each of the $(\tilde{q}, \tilde{p})_i$ λ is varied in a neighborhood of $\hat{\lambda}$, and $\frac{\partial H}{\partial \hat{\lambda}}(\tilde{q}, \tilde{p}_i, \hat{\lambda})$ is estimated.
- Eq. 4.46 may now be computed like:

$$\frac{dF}{d\lambda}|_{\hat{\lambda}} = \frac{1}{M} \sum_{i=1}^{M} \frac{\partial H}{\partial \hat{\lambda}}(\tilde{q}, \tilde{p}_i, \hat{\lambda})) \tag{4.48}$$

Eq. 4.48 can now be numerically integrated on an interval of interest to give the free energy of Eq. 4.47.

4.6.3 Umbrella sampling

Sometimes it may be difficult to calculate even numerically the derivative of the Hamiltonian in Eq. 4.46. The umbrella sampling is a numerically cheaper method, which can be used alternatively to a dynamics coupling parameter method [6].

The definition of the free energy for a given value λ_b of λ:

$$A(\lambda_b) = -KT \log(\int \exp\left(-\frac{1}{KT}\ H(\lambda_b)\right) d\tilde{q}d\tilde{p}) \tag{4.49}$$

can be identically written as:

$$\frac{A(\lambda_b)}{-KT} = \log\left(\frac{\int \exp(-\frac{1}{KT}(\overbrace{H(\lambda_b) - H(\lambda_a)}^{\Delta H} + H(\lambda_a)))d\tilde{q}d\tilde{p}}{\int \exp(-\frac{1}{KT}H(\lambda_a))d\tilde{q}d\tilde{p}} \int \exp(-\frac{1}{KT}H(\lambda_a))d\tilde{q}d\tilde{p}\right) \tag{4.50}$$

where λ_a is a different value of λ, and $\Delta H = H(\lambda_b) - H(\lambda_a)$. Eq. 4.50 is:

$$\frac{A(\lambda_b)}{-KT} = \log \overbrace{\left(\frac{\int \exp(-\frac{1}{KT}\Delta H) \exp(-\frac{1}{KT}H(\lambda_a))d\tilde{q}d\tilde{p}}{\int \exp(-\frac{1}{KT}H(\lambda_a))d\tilde{q}d\tilde{p}} \right)}^{\langle \exp(-\frac{1}{KT}\Delta H)\rangle_{\lambda_a}} + \underbrace{\log \left(\int \exp(-\frac{1}{KT}H(\lambda_a))d\tilde{q}d\tilde{p} \right)}_{A(\lambda_a)/(-KT)} \tag{4.51}$$

and gives the final formula:

$$A(\lambda_b) - A(\lambda_a) = -KT \log(\langle \exp -\frac{1}{KT}\Delta H\rangle_{\lambda_a}) \tag{4.52}$$

Eq. 4.52 might seem to be a fantastic formula for computing free energy differences. The mean value of the energy difference $\Delta H = H(\lambda_b) - H(\lambda_a)$ computed on the canonical ensemble for $\lambda = \lambda_a$, gives the free energy difference of two states of the system for whatsoever given values λ_b and λ_a of λ. Unfortunately Eq. 4.52 numerically does not work when the difference of λ_b and λ_a is too large. In this case the energy difference ΔH might be so large that the zones of the phase space $(\tilde{q}, \tilde{p})$ which give the biggest contribution to the term $\exp(-H(\lambda_a)/KT)$ may only slightly overlap, or even be disjoint, from those where $\exp(-\Delta H/KT)$ is not zero, and the integral of Eq. 4.52 would be underestimated. The umbrella sampling works fine only if the energy difference ΔH relative to the variation of λ is small. Nevertheless, using a step-by-step procedure, it is possible to compute energy differences even for values λ_a and λ_b of λ corresponding to very different states of the system. The step-by-step procedure may be as follows:

- The interval $[\lambda_a, \lambda_b]$ is divided into N sub intervals $[\lambda_i, \lambda_{i+1}]$, where:

$$\lambda_{i=1} = \lambda_a \qquad \lambda_{i=N} = \lambda_b \qquad \lambda_i \langle \lambda_{i+1} \tag{4.53}$$

- The free energy difference $\Delta A_{i+1,i} = A(\lambda_{i+1}) - A(\lambda_i)$ is computed using the umbrella sampling of Eq. 4.52.

- The sum of all the $\Delta A_{i+1,i}$ gives the free energy difference $A(\lambda_b) - A(\lambda_b)$:

$$A(\lambda_b) - A(\lambda_a) = \sum_{i=2}^{N} \Delta A_{i+1,i} \tag{4.54}$$

4.7 Numerical methods

The solution of the Hamiltonian and of the Nosé-Hoover equations of motion for given initial conditions can be obtained numerically using standard methods for solution of ordinary differential equations [6]. Given the position $(\tilde{q}(t), \tilde{p}(t))$ of the system in the phase space at a certain time t, it is attempted to obtain the position $(\tilde{q}(t+\delta t), \tilde{p}(t+\delta))$ at a later time $t+\delta t$ to a sufficient degree of accuracy:

$$\begin{array}{rcl} \tilde{q}(t+\delta t) & = & \Gamma_q(\tilde{q}(t), \tilde{p}(t)) \\ \tilde{p}(t+\delta t) & = & \Gamma_p(\tilde{q}(t), \tilde{p}(t)) \end{array} \tag{4.55}$$

where Γ_q nd Γ_p are the discrete representations of the evolutor in the phase space and depend on the particular choice of the algorithm. The choice of δt, which is called the time step of the simulation, will depend somewhat on the method of solution, but is typically much smaller than the typical time of the system. There are many possible algorithms which could be used for solving the Hamiltonian and the Nosé-Hoover equations of motion. A list of the features a successful simulation algorithm should possess could be as follows:

(a) It should be fast.

(b) It should permit the use of a long time step δt.

(c) It should approximate the classical trajectory as close as possible.

(d) It should satisfy the known conservation laws for energy.

Point (a) is not so important. In a typical simulation of condensed matter the time spent for the calculation of the atomic forces is much bigger than the time used to integrate the equations of motion.

Point (b) is of crucial importance. The bigger δt is, the longer the trajectory can be followed and the more accurate the calculation of all the observables is. Obviously δt cannot be increased without a loss in accuracy at reproducing the classical trajectory.

Point (c) is very delicate and contains a request which in principle cannot be satisfied. Under very general assumptions on the atomic forces two trajectories of the same classical system, whose initial conditions are very close to each other, diverge exponentially with time. In the same way any very little perturbation, even associated with the tiny error due to the finite arithmetic, will let any computer-generated trajectory diverge from the classical one, even if they have the same initial condition. No integration algorithm will provide an exact solution for a long time.

But it is not needed to reproduce the classical trajectory over an infinite time. In doing molecular dynamics simulations we are interested in calculating mean values of observables on statistical ensembles. These mean values are computed by averaging dynamical quantities over a trajectory which essentially must only reproduce the statistics of interest. If one is interested in computing averages in the microcanonical ensemble, the first requirement which must be fulfilled is that the trajectory of system remains on the manifold of constant energy, which is the requirement of point (d). Even for the Nosé-Hoover dynamics the most important requirement which must be fulfilled is that the energy of Eq. 4.20 on page 75 is conserved. In this case all the points of the computer generated dynamics belong generally to different exact Nosé-Hoover dynamics, because the manifold $\mathcal{H} = const$ contains all the possible Nosé-Hoover trajectories. Therefore if our algorithm satisfies the condition of (d), but fails to reproduce a single classical trajectory, the statistic of the dynamic will be the right one (see Fig. 4.3).

The interaction potential and the model system in which the simulations have been performed is contained in the next chapter.

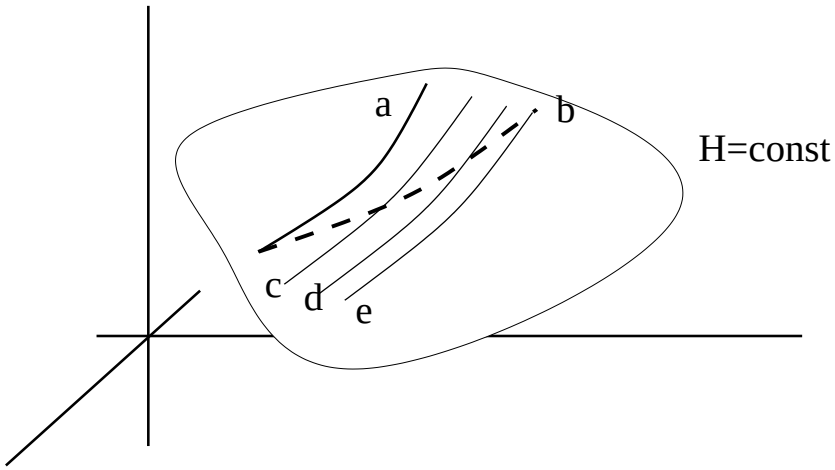

Figure 4.3: *Nosé-Hoover dynamics on the manifold $\mathcal{H} = const$ of Eq. 4.20. The classical trajectory (a) and the computer-generated (b) have the same initial condition, and diverge for long time. If the trajectory (b) remains on the manifold, it will meet other Nosé-Hoover dynamics, different from the initial one ((c) (d) and (e) in the figure), and the statistics of the system will nonetheless be the canonical one.*

Chapter 5

INTERACTION POTENTIAL AND MODEL SYSTEM

In this chapter the model system of the simulations which are discussed in the next chapters is presented. In the first part the potential used in the numerical calculations is defined. In the second part it will be discussed how the parameters of the potential are tuned for the atomic system obtained by decorating the Tübingen triangle tiling.

5.1 Interaction potential

In a system containing N atoms the potential energy V can be divided into terms depending on the coordinates of individual atoms, pairs, triplets, etc.:

$$V = \sum_i v_1(q_i) + \sum_i \sum_{j>i} v_2(q_i, q_j) + \sum_i \sum_{j>i} \sum_{k>j} v_3(q_i, q_j, q_k) + ... \qquad (5.1)$$

where q_i is the coordinate of the atom i. The potential used in our simulations is the *Lennard-Jones* potential (LJ). The LJ potential contains only the pair potential terms, which depend on the magnitude of the pair separation $|r_i - r_j| = r_{ij}$. Even if the LJ potential was developed for describing crystals of noble gases [8], it is widely used also in molecular dynamics simulations of condensed matter. The analytical form of the LJ potential V_{LJ}:

$$V_{LJ} = \epsilon[(\frac{\sigma}{r_{ij}})^{12} - 2(\frac{\sigma}{r_{ij}})^{6}] \qquad (5.2)$$

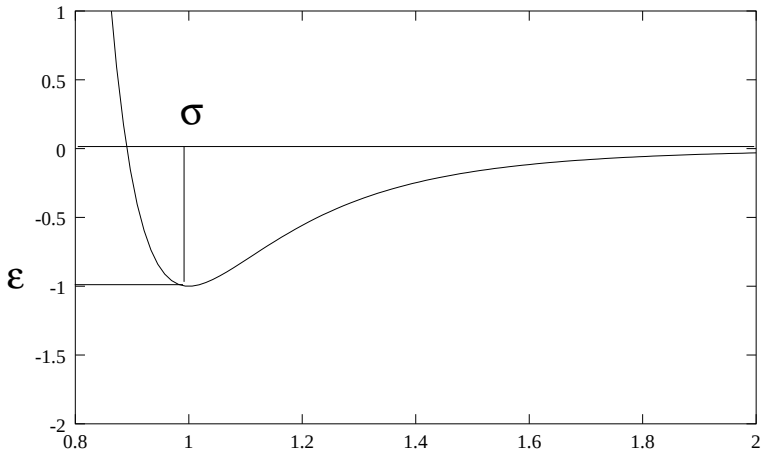

Figure 5.1: *Lennard-Jones potential for* $\epsilon = \sigma = 1$.

depends on two parameters ϵ and σ, which give, respectively, the depth and the position of the minimum of the potential energy (see Fig. 5.1).

The LJ potential is not a long-range potential. The interaction between atoms at a distance bigger than 3σ is almost zero. Thus, in computing the potential energy and forces, only pairs are considered whose distance is smaller than a *cut-off* radius r_c, which is normally set to $2.5\sigma - 3.0\sigma$. This procedure reduces the number of interactions to be computed and speeds up significantly the forces and potential energy calculation.

The truncation of the potential at a cut-off distance can introduce some difficulties in the calculation of the potential energy and of the forces. The potential energy and the force on a particle, which leaves or enters the cut-off interaction sphere of another, suffer a discontinuity. The discontinuities of the potential energy and of the force are due respectively to the discontinuity of the values and of the first derivative of the potential at r_c. Both these problems can be avoided by adding a small linear term and a constant one to the potential, whose analytical form is modified as follows [6]:

$$\hat{V}_{LJ} = \begin{cases} V_{LJ}(r_{ij}) - v_c - (r_{ij} - r_c) \left(\dfrac{dV_{LJ}(r_{ij})}{dr_{ij}} \right)_{r_{ij}=r_c} & r_{ij} \leq r_c \\ 0 & r_{ij} > r_c \end{cases} \tag{5.3}$$

Interaction	A-A	A-B	B-B
σ	1.1755	1.0	0.6180
ϵ	1.0	2.0	1.0

Table 5.1: *Values of σ and ϵ for the system obtained by decorating the Tübingen triangle system.*

5.2 Model system

All the simulations whose results are contained in the next chapters have been performed in the system obtained by decorating the Tübingen triangle tiling (see Section 2.5.2 on page 39). The decoration is made with two atom types. The big ones (atoms A) are placed on the vertices of the tiling, and the small ones (atoms B) at the center of the isosceles triangles. The potential of the system is the sum of three terms:

$$V_{LJ} = V_{AA} + V_{AB} + V_{BB} \tag{5.4}$$

accounting for the interaction of the atoms of the same kind (V_{AA}, V_{AB}), and of different kind (V_{AB}). To avoid that an atom A could change its place with one of type B, the minimum potential energy ϵ is set to 1 for the interaction between atoms of the same kind, and to 2 for atoms of different kind. The value of σ is set to the geometric distance of neighboring atoms in the decoration (see values reported in Table 5.1).

The atomic system which is obtained with such a choice of the potential parameters has some mechanical properties, which can be qualitatively easily understood.

In the decoration of the tiling there are *clusters* of one atom A (the big one) surrounded by two concentric rings of ten atoms. The inner ring is of atoms of type B, and the outer of atoms of type A (see Fig. 5.2). A cluster is a highly symmetric structure and its toughness may be very high. A fracture propagating in such a material is expected to move between the clusters instead of trying to break one of them.

The cluster centers are situated on five families of parallel lines, mutually rotated by 36^0 with a large and small separation within each family, arranged in a Fibonacci sequence [77].

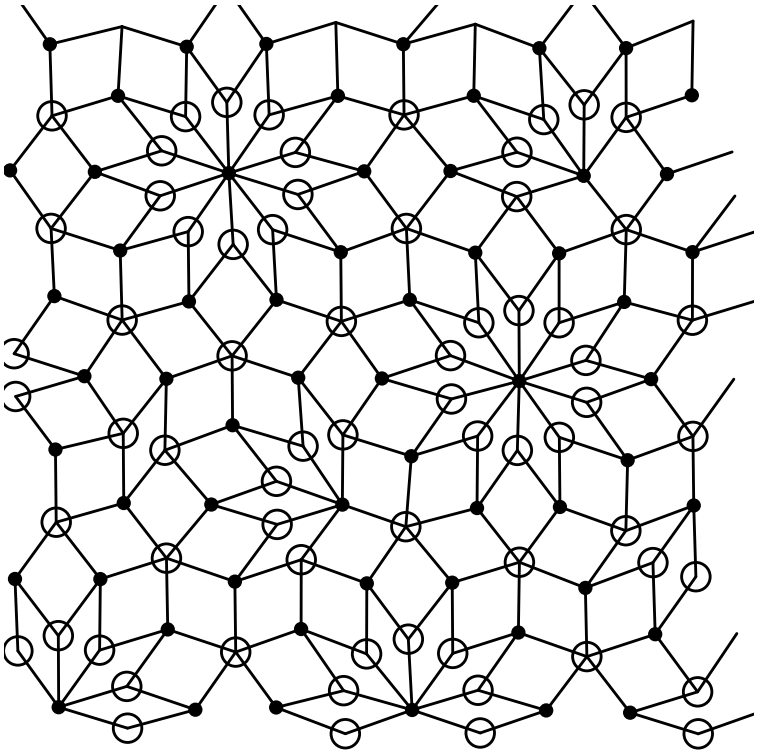

Figure 5.2: *Clusters formed by a big atom (in the center) surrounded by ten little ones.*

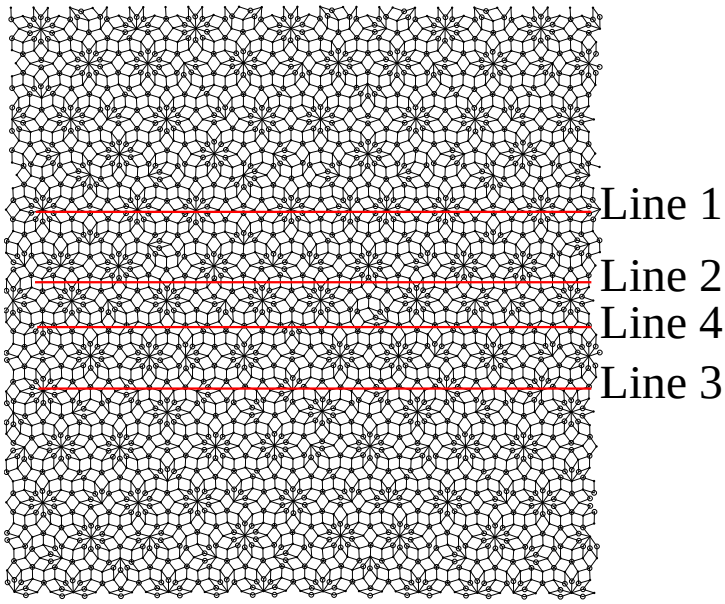

Figure 5.3: *The four lines on which the surface energies have been computed*

In the tiling there are other four families of parallel lines which are important for the scopes of this work (see Fig. (5.3)).

Line 1 The lines 1 connect the centers of the clusters, and the distances between two consecutive lines form a Fibonacci sequence.

Line 2 The line 2 is between two lines 1, which lie at the small separation of the Fibonacci sequence.

Line 3 The line 3 is between two lines 1, which lie at the big separation of the Fibonacci sequence. On line 3 there is a high concentration of partially broken clusters.

Line 4 The line 4, like line 3, is between two lines 1, which lie at the big separation of the Fibonacci sequence. Contrary to line 3, on line 4 there is a low concentration of partially broken clusters.

Preferred cleavage planes, the "easy lines" for fracture, are the lines 2,3 and 4, because the fracture can propagate along this direction without breaking any cluster. The surface energy is not the same for each of these lines.

The lines possessing the lowest surface energy are those in between the clusters separated by the biggest distance (see Fig. 5.3) [77].

Furthermore these lines have the lowest "unstable stacking fault energy", which is the increase when the two half are shifted relative to each other, and therefore these directions are preferred for dislocation emission.

The next chapter is divided into two parts. The first part describes the procedure used to prepare the initial condition of the crack propagation dynamics. The second part presents an original model for crack propagation with temperature.

Chapter 6

MOLECULAR DYNAMICS OF FRACTURE

In this chapter the molecular dynamics model of crack propagation in the presence of temperature is presented.

6.1 Definition of the system and preparation of the simulation

The system in which all the simulations are performed is a rectangular configuration of atoms, with a single edge crack inside loaded in Mode I by applying a constant displacement on the long side of the rectangle.

Any molecular dynamics simulation needs an initial configuration for the dynamics. In the molecular dynamics study of crack propagation a dynamics starting from an initial configuration which is not carefully prepared, may produce effects which are not due to the physics of crack propagation, but are originating by the badly posed initial conditions.

The operating procedure to prepare a good initial condition for the molecular dynamics of crack propagation at a given temperature T is divided in two steps.

The first step consists in equilibrating the configuration with the edge crack at the critical value of the displacement, using the following procedure:

1. A cut is made in a stress free rectangular configuration along a **line 4** in the sample.

2. The atoms of the configuration are linearly displaced in the direction of the small side of the rectangle, so that the atoms lying on the long side are moved to the critical displacement Δ_c (see Fig. (6.1).(a)).

3. The configuration so obtained (see Fig. 6.1.(b)) is given as initial condition of an equilibrium Nosé-Hoover dynamics, where the atoms of two strips lying along the longest side of the rectangle are not allowed to move. During the dynamics no crack propagation takes place and the system relaxes towards a minimum of the free energy.

   In the second step a configuration of a crack displaced at a value of Δ beyond the critical one can be obtained with the following procedure:

4. The displacement field $\mathbf{u}_c$ of the relaxed configuration at the critical value of Δ_c with respect to the stress free configuration is computed.

5. The initial condition for the dynamics of crack propagation is obtained by applying a new displacement field $\mathbf{u} = (1 + \epsilon)\mathbf{u}_c$, where $\epsilon > 0$, to the initial stress free reference configuration with no cut.

6.2 Modeling crack propagation with temperature

In reality it would be conceptually straightforward to prepare an experiment of crack propagation in the presence of temperature. The sample is put in a oven for a sufficiently long time to equilibrate at the given temperature, afterwards a load beyond the critical one is applied to the system, and crack propagation is observed. During crack propagation the temperature may not be uniform in the sample. A crack may loose energy in form of shock waves, which are typically emitted from the crack tip, and which may induce a temperature gradient in the material when the crack reaches a steady state of propagation. The velocity of these waves, and therefore the influence they have on crack propagation by taking energy away from the crack tip, may depend on the temperature of the system. In the material only the atoms close to the surface have the possibility of exchanging a surplus of heat with the surroundings, eventually coming from the crack tip in form of shock waves, and thus only these atoms in the sample are at constant temperature.

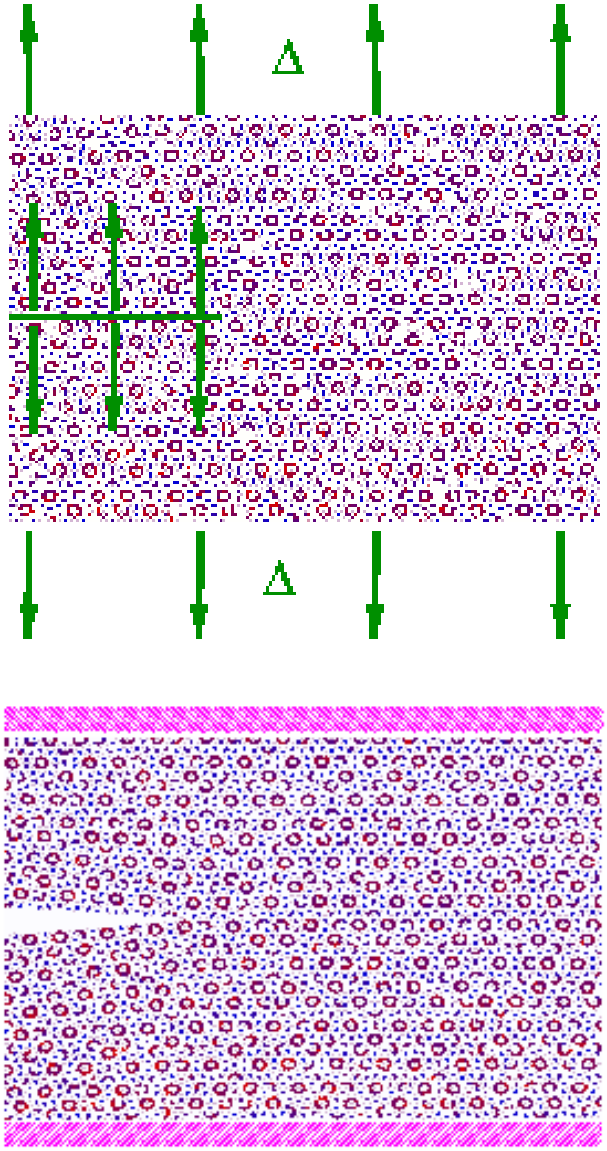

Figure 6.1: *(a) A cut is made in a stress free configuration and the atoms of the configuration are linearly displaced in the direction of the small side of the rectangle. (b) Initial configuration for an equilibrium Nosé-Hoover dynamics*

In a molecular dynamics simulation such a realistic situation might be modeled by dividing a rectangular sample into two zones, separated by a ellipse whose center is in the center of the rectangle (see Fig(6.2)). The atoms outside the ellipse, which are those close to the surface of the sample, move according to the Nosé-Hoover dynamics. In the Nosé-Hoover dynamics, which is a tool used to simulate a system at constant temperature, *every* atom is coupled with the heath bath via a viscosity (see Section. 4.3 on page 72), which can *locally* change the energy distribution, in order to drive the system towards a state of *globally* constant temperature. Using a Nosé-Hoover dynamics a temperature gradient is smoothed out as fast as possible. This is exactly the right dynamics for the atoms close to the surface of the sample, but is not appropriate for the atoms inside the ellipse, which move according to the Hamilton dynamics to allow for a temperature gradient close to the crack tip.

Chapter 7 is the first of the second part of this work, and it contains important results of the equilibrium molecular dynamics at constant temperature. The calculations of the surface energies, of the elastic constants and of the critical displacements in the Tübingen binary system are the original results exposed in the next chapter. These results have shown to be very useful to understand qualitatively the influence of dislocation emission on crack propagation observed during crack propagation at low loads and low temperatures.

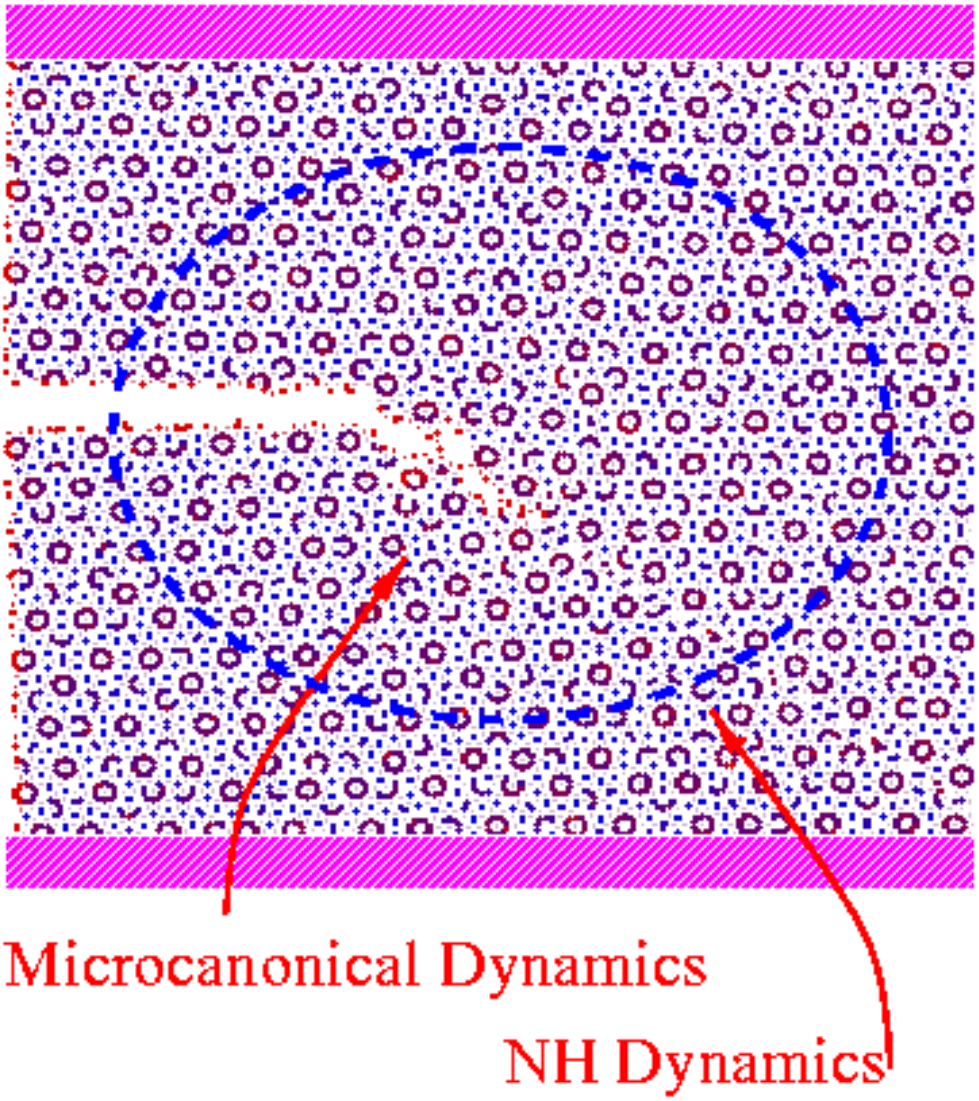

Figure 6.2: *Model for crack propagation in the presence of temperature. The rectangular sample is divided into two zones separated by an ellipse. The atoms outside the ellipse move according to the Nosé-Hoover dynamics. The atoms inside are subjected to Newton's law.*

Part II

NUMERICAL RESULTS

Chapter 7

RESULTS OF EQUILIBRIUM MOLECULAR DYNAMICS

In this chapter the results of the equilibrium molecular dynamics simulations performed on the Tübingen triangle lattice are presented.

The first part deals with the optimization of mass for the Nosé-Hoover thermostat. The second part contains the results of free energy calculations.

7.1 Temperature dependence of the Nosé-Hoover mass constant ν

In Section 4.5, the Eq. 4.30 on page 80 defines the value of the Einstein frequency ω_E for a system composed of a single atom type[1]:

$$\nu^2 = \omega_E^2 = \frac{< \mathbf{F}^2 >}{fKT} \tag{7.1}$$

which it is found to be the best value for the Nosé-Hoover mass ν. The value of ν depends on the mean value $< \mathbf{F}^2 >$ of the force $\mathbf{F}$ exerted on the atom. The question is now on which ensemble the mean value of Eq. 4.30 should be computed. If one aims at measuring the temperature dependence of ν the mean value of $\mathbf{F}$ should be computed in the canonical ensemble.

[1] If the system is composed of more atom types, the optimal value of ν is the mean value of the Einstein frequency of every atom type.

The problem is that there is so far no operatively working computational tool for computing averages on the canonical ensemble. The Nosé-Hoover dynamics is well suited for such a problem, provided that the right value of ν has been found, which is exactly the problem we have to tackle. A solution may be to use a Monte Carlo algorithm [82, 92, 73, 10] which is the standard alternative way to the molecular dynamics for simulation in the canonical ensemble. Another cheaper solution would be to compute the mean value of Eq. 4.30 in the microcanonical ensemble. It can be demonstrated that in the thermodynamic limit of infinite size, the mean value of an observable $< \mathcal{A} >_{NVE}$ in the microcanonical ensemble, and that $< \mathcal{A} >_{NVT}$ in the canonical, are equal [6]:

$$< \mathcal{A} >_{NVE} = < \mathcal{A} >_{NVT} \tag{7.2}$$

provided that the mean values of the total energy H are equal:

$$< \mathcal{H} >_{NVE} = < \mathcal{H} >_{NVT} \tag{7.3}$$

In the finite size case, which is the only case considered in the simulations, Eq. 7.2 should be corrected with terms of order $O(1/N)$, where N is the number of degrees of freedom. With a number of particles of the order of thousands these corrections are already negligible.

The iterative procedure which may be used for computing ν at a temperature T_0 looks as follows:

1) A set of initial positions is chosen.

2) The initial velocities for the Hamiltonian dynamics are sampled out of the Maxwell distribution at the temperature T_0.

3) The average values $< \mathcal{H} >_{NVE}$, $< T >_{NVE}$ and $< \mathbf{F}^2 >_{NVE}$ are computed.

4) A test value of $\hat{\nu}$ is calculated as:

$$\hat{\nu} = \frac{< \mathbf{F}^2 >_{NVE}}{fKT} \tag{7.4}$$

5) A Nosé-Hoover dynamics is started at the temperature T_0 using $\hat{\nu}$.

6) The equilibrium mean value $< \mathcal{H} >_{NVT}$ is computed.

7) If $| < \mathcal{H} >_{NVT} - < \mathcal{H} >_{NVE} | > \epsilon$, where ϵ is a chosen tolerance, the method starts back at 2), with a different initial temperature.
If $< V >_{NVT}$ is smaller than $< V >_{NVE}$, where V is the potential energy of the system, the starting temperature must be bigger than T_0, smaller otherwise.

In practice in a condensed matter system below the melting temperature, the differences of $< \mathcal{H} >_{NVT}$ and $< \mathcal{H} >_{NVE}$ of point (7) are normally not so big, and the value of $\hat{\nu}$ of Eq. 7.4 already at the first step is a good working value for ν.

The values of ν for a rectangular system with free boundaries of 4134 particles of a Tübingen triangle tiling have been measured in a range of temperatures below the melting temperature T_M, and are reported in Table 7.1. Values of ν for very small temperatures have been measured, too, even if the Nosé-Hoover thermostat for temperatures close to zero may not work. A system at a very low temperature moves around a local minimum of the potential, and therefore the potential energy becomes a sum of harmonic terms. Under such conditions even a very complicated chaotic potential becomes very simple, and the system may not anymore be ergodic (cf. Section 4.4).

The fit of the values of ν against the function $f(T) = a\sqrt{T}$ gives for the parameter a the value:

$$a = 22.2477 \pm 0.1004 \qquad (\pm 0.4512\%) \tag{7.5}$$

and the function:

$$\nu(T) = 22.2\,\sqrt{T} \tag{7.6}$$

reproduces the measured values very well (see Fig. 7.1).

The systems where crack propagation is investigated have typically no periodic boundary conditions, but nevertheless w_e seems still to be a good value of ν at which ergodicity is realized at a reasonable computing time.

T/T_M	ν
1.65e-10	1.078e-4
0.015	1.49
0.031	2.11
0.046	2.59
0.077	3.35
0.102	3.86
0.188	5.27
0.312	6.84
0.422	8.01
0.489	8.66
0.640	10.00
0.704	10.54
0.798	11.31
0.886	11.98
0.953	12.48

Table 7.1: *Values of ν for the Tübingen triangle tiling at different temperatures.*

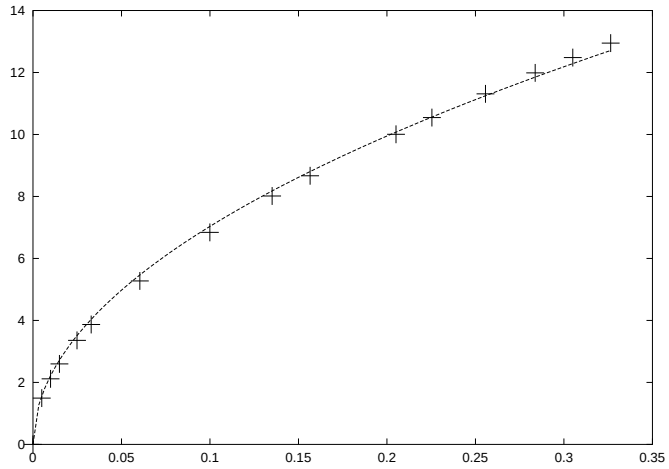

Figure 7.1: *Measured values of ν (points) with the function $\nu(T) = 22.2\sqrt{(}T)$, for different temperatures.*

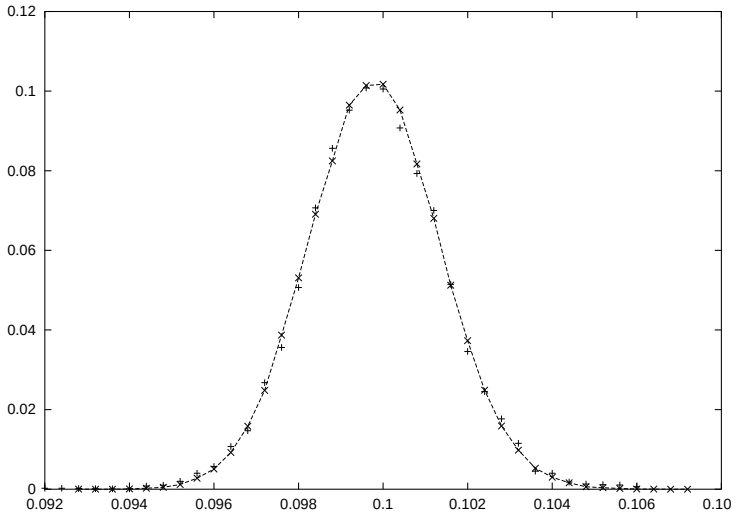

Figure 7.2: *Distribution of the temperature T for a quasi-crystalline system of 4134 Lennard-Jones particles at 30% of the melting temperature T_M of the system. The line represents the theoretical Maxwell distribution. The points represent the distribution out of 100.000 time steps of a Nosé-Hoover dynamics with $\nu = w_e$.*

This is mainly due to the fact that the value of ν is proportional to the mean force exerted on one atom, and this force depends strongly on the local arrangement of the atoms, weakly on the boundary conditions, and not at all on the system size. Fig. 7.2 represents the theoretical distribution of temperature and the distribution computed out of a Nosé-Hoover dynamics for a quasi-crystalline system of 4134 Lennard-Jones particles for $\nu = w_e$. The agreement of the computed and the theoretical distribution is satisfactory, and the system is ergodic already after some vibrational periods of the frequency w_e.

7.2 Critical displacement via free energy calculations.

7.2.1 An empirical formulation of the Griffith criterion.

The Griffith criterion of Section 3.3.4 can be reformulated in an empirical way, which is much more adequate for a molecular dynamics simulation than the definition by Eq. 3.32 on page 60.

Let us consider a stress free elastic body, which hereafter is called the *reference configuration*, and let us suppose to apply a force or a displacement field to the boundary or to a part of it. The direction of the force or displacement field is that of the outer normal, the intensity is constant and depends on a parameter Δ (see Fig. 7.3(a)). The body increases its elastic energy $E(\Delta)$ for non zero values of Δ, and the energy increase depends quadratically on Δ in the linear elastic regime.

Let us now suppose to gently cut the reference configuration along a line inside the body (see Fig. 7.3(b)) in such a way that the configuration with the cut is again a stress free elastic body[2]. This cutting transformation is not free, and some energy E_{cut} must be given to the system in order to form a new free surface.

The value of Δ_c at which $E(\Delta)$ is equal to E_{cut} is called the *critical value for crack propagation* of the parameter Δ. No crack propagates if the system is partially cut along the line, and meanwhile strained or loaded at values of Δ smaller than Δ_c, because in this case the elastic energy of the body is smaller than the energy needed to form a new surface (see Fig. 7.4). When Δ exceeds Δ_c, the elastic energy stored in the system is bigger than the energy needed to cut the body along the line. Therefore the system may find it convenient to release all its elastic energy excess to the formation of a new free surface, and to relax again to a stress free configuration which is a local minimum of the elastic energy, eventually converting some residual energy in elastic waves.

[2]If the cut is made too fast there can be some plastic effects coming about, like dislocation formation and so on.

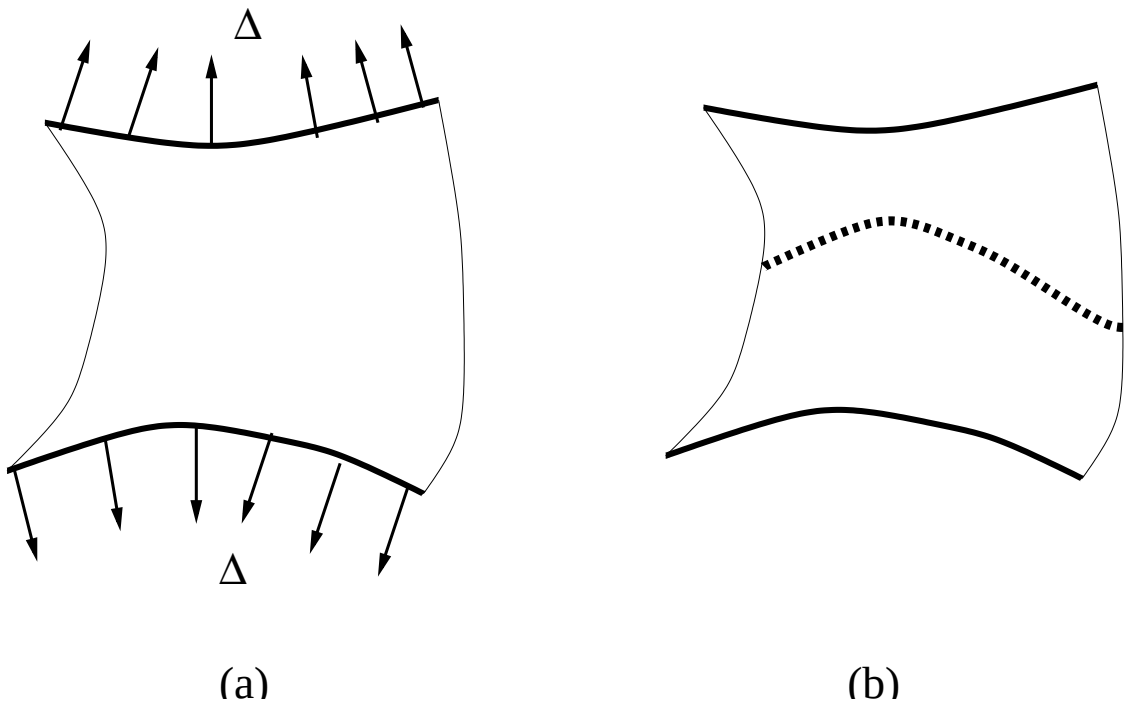

Figure 7.3: *a) Part of the boundary (thick line) of a stress free body is loaded with a constant displacement or a constant force, whose intensity depends on a parameter* Δ*. The rest of the boundary is free. b) A cut is made inside the body (dashed line).*

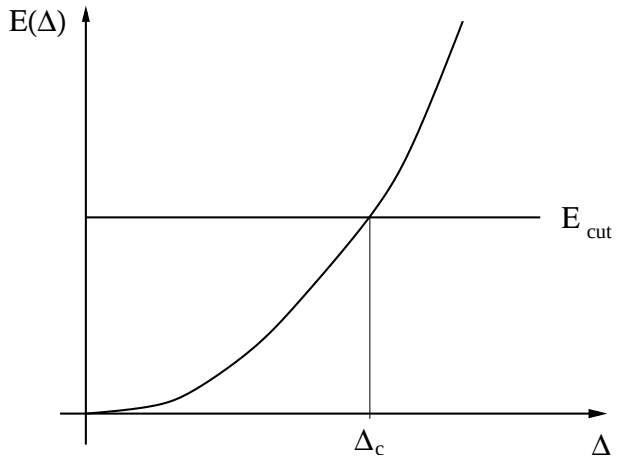

Figure 7.4: *The critical value Δ_c for crack propagation at which $E(\Delta)$ is equal to E_{cut}.*

7.2.2 The thermodynamical meaning of the elastic energy

In the preceding section an empirical formulation of the Griffith criterion has been given based on the comparison of elastic energies. The question now arises, what the elastic energy is and what its thermodynamical meaning is. Only by answering this question it is possible to bridge the gap between the continuum theory of elasticity and the molecular dynamics modeling of condensed matter at equilibrium.

The basic equations of the theory of elasticity do not require the existence of an elastic energy. The requirement that a body possesses a thermodynamically well defined macroscopic elastic energy is an additional very strong hypothesis on the system, and the materials which have an elastic energy are called *superelastic* [32]. In the following it is demonstrated that an elastic body at constant temperature has an elastic energy, and that the *differences* of elastic energy are the differences of free energy, even if in this case the elastic energy *is not* the free energy [67].

The theory of elasticity considers only two kinds of forces: the long range *body forces* and the short range *contact forces*. Mathematically the different interaction scale is expressed requiring that the body forces are acting on *volumes*, while the contact forces are acting on *surfaces*. Let $\mathbf{f} : R^3 \rightarrow$

$R^3, \mathbf{f} = \mathbf{f}(\mathbf{x}), \mathbf{x} \in R^3$ be the vector field of the body forces density. The force $\mathbf{F}$ acting on a punctual mass δm at a point $\mathbf{x}$ is defined as:

$$\mathbf{F}(\mathbf{x}) = (\delta m)\mathbf{f}(\mathbf{x}) \tag{7.7}$$

and for the density π of the surface forces a similar definition can be used.

Let V be the closed volume occupied by an elastic body possessing a mass density $\rho : V \to R, \rho = \rho(\mathbf{x})$, and let $\mathbf{u}(t) : V \times R \to R^3, \mathbf{u}(t) = \mathbf{u}(\mathbf{x}, t), \mathbf{x} \in V$ be the displacement field expressing the deformation undergone by the body at time t. During the deformation the external forces acting on the volume (the body and the contact ones) are performing a work, the kinetic energy of the body is changing and the system is exchanging heat with the surrounding: the system is undergoing a thermodynamic transformation. We will express the differential of some thermodynamic properties of interest *only* as the differential of the time.[3]

The differential of the body forces $\mathbf{f}$ density is the 1-form [4]:

$$df = f_i(\mathbf{x})dx_i. \tag{7.10}$$

The 1-form df on each curve $\mathbf{u}(\mathbf{x}, t)$, being $\mathbf{x}$ thought of as a fixed point of the volume V, is expressed by:

$$df = f_i(\mathbf{u}(\mathbf{x}, t))\frac{\partial u_i}{\partial t}dt \quad \mathbf{x} \in V \tag{7.11}$$

[3]This is always possible for every thermodynamic transformation. A thermodynamic transformation can be thought of as a curve in a phase space, being the time the parameter of the curve. The differential of a thermodynamic property is now involving only the differential of the time. For example, be $S = S(V, T)$ the entropy of a system defined only by its temperature and volume. The differential dS of S is the 1-form:

$$dS = \frac{\partial S}{\partial V}dV + \frac{\partial S}{\partial T}dT \tag{7.8}$$

whose pull-back defined by a generic thermodynamic transformation $\gamma(t) = (V(t), T(t))$ is:

$$dS = (\frac{\partial S}{\partial V}\frac{dV}{dt} + \frac{\partial S}{\partial T}\frac{dT}{dt})|_\gamma dt. \tag{7.9}$$

[4]The convention of summation over repeated indexes is assumed.

Under the hypothesis that the deformation is small, we can assume that the force density and the mass density remain equal to their values on the initial volume V. For this reason Eq. 7.11 can be rewritten as:

$$df = (f_i(\mathbf{x})\frac{\partial u_i}{\partial t})dt \quad \mathbf{x} \in V \tag{7.12}$$

and by integration on the volume V it can be obtained the differential dF of the work of the body forces:

$$dF = (\int_V \rho(\mathbf{x}) f_i(\mathbf{x})\frac{\partial u_i}{\partial t} dv)\, dt \tag{7.13}$$

For the work $d\Pi$ of the contact forces a similar expression can be written, where now the integration must be performed on the surface:

$$d\Pi = (\int_S \rho \pi_i \frac{\partial u_i}{\partial t} ds)\, dt \tag{7.14}$$

dropping in Eq. 7.14 the explicit dependence of ρ and π on $\mathbf{x}$. From $\pi = \boldsymbol{\sigma}\mathbf{n}$, being $\boldsymbol{\sigma}$ the stress tensor and $\mathbf{n}$ the outer normal to the surface, we can write:

$$d\Pi = (\int_S \sigma_{ij} n_j \frac{\partial u_i}{\partial t} ds)\, dt \tag{7.15}$$

and using the symmetry of $\boldsymbol{\sigma}$ and the Stokes theorem:

$$d\Pi = (\int_S n_j \sigma_{ji} \frac{\partial u_i}{\partial t} ds)\, dt \; = (\int_V div(\sigma_{ji}\frac{\partial_t u_i}{\partial t}) dv)\, dt \tag{7.16}$$

Writing in indexes the integrand in Eq. 7.16:

$$\begin{aligned} div(\sigma_{ji}\partial_t u_i) &= \partial_j(\sigma_{ji}\partial_t u_i) \\ &= (\partial_j \sigma_{ji})\partial_t u_i + \sigma_{ji}\partial_t \partial_j u_i \\ &= div(\boldsymbol{\sigma})\partial_t \mathbf{u} + \frac{1}{2}(\sigma_{ji}\partial_t\partial_j u_i + \sigma_{i,j}\partial_t \partial_i u_j) \\ &= div(\boldsymbol{\sigma})\partial_t \mathbf{u} + \boldsymbol{\sigma}\partial_t \boldsymbol{\epsilon} \end{aligned}$$

where again use has been made of the symmetry of $\boldsymbol{\sigma}$. The expression of $d\Pi$ becomes then:

$$d\Pi = (\int_V (div(\boldsymbol{\sigma})\partial_t \mathbf{u} + \boldsymbol{\sigma}\partial_t \boldsymbol{\epsilon})dv)dt \tag{7.17}$$

Under the hypothesis that the deformation of the volume remains at any time small, we can express as a first approximation the kinetic energy per unit of volume as[5]:

$$\rho_T = \rho\frac{1}{2}(\partial_t^2 u_i)^2 \tag{7.18}$$

and by integrating over the volume we obtain the differential of the kinetic energy:

$$dW_T = (\int_V \frac{d\rho_T}{dt}dv)\, dt = (\int_V \rho\partial_t^2 u_i \partial_t u_i dv) \quad dt \tag{7.19}$$

Let us consider now the first principle of thermodynamics. In the continuum approximation the internal energy can be written as:

$$U = \int_V (T + V)dv \tag{7.20}$$

where T is the kinetic energy per unit of volume, and V is the potential energy per unit of volume. It is not possible to give an analytic expression for V, but we assume this function to exist. The differential form of the first principle is:

$$dU = \delta Q + \delta W \tag{7.21}$$

Expressing all the differential quantities involved as time differentials, we can write Eq. 7.21 as:

[5]If the deformation were not small, the density would change as well.

$$\overbrace{\int_V (\rho \partial_t^2 u_i \partial_t u_i dv) \quad dt}^{\text{kinetic energy}} + \overbrace{\int_V dV dv}^{\text{potential energy}} = \overbrace{\delta Q}^{\text{heat}} + \underbrace{(\int_V (div(\boldsymbol{\sigma})\partial_t \mathbf{u} + \boldsymbol{\sigma}\partial_t \boldsymbol{\epsilon}) dv) dt}_{\text{work of the contact forces}} + \underbrace{(\int_V \rho(\mathbf{x}) f_i(\mathbf{x}) \frac{\partial u_i}{\partial t} dv) dt}_{\text{work of the body forces}} \tag{7.22}$$

using the fundamental equation of the theory:

$$div(\boldsymbol{\sigma}) + \rho \mathbf{f} = \rho \frac{\partial^2 \mathbf{u}}{\partial t^2} \tag{7.23}$$

we arrive at the final formula:

$$(\int_V \boldsymbol{\sigma} \partial_t \boldsymbol{\epsilon} dv) dt = \int_V dV dv - \delta Q \tag{7.24}$$

The differential of the 0-forms ϵ_{ij}, which are the components of strain, can be approximated as:

$$d\epsilon_{ij} = \partial_k \epsilon_{ij} dx_k + \partial_t \epsilon_{ij} dt = \partial_t \epsilon_{ij} dt \tag{7.25}$$

because the terms $\partial_k \epsilon_{ij} dx_k$ in the linear approximation are set to zero, and Eq. 7.23 becomes then:

$$\int_V \boldsymbol{\sigma} d\boldsymbol{\epsilon} dv = \int_V dV dv - \delta Q \tag{7.26}$$

Let us now distinguish two cases.

If the system performs an *adiabatic transformation*, δQ is zero, the 1-form $\int_V \boldsymbol{\sigma} d\boldsymbol{\epsilon} dv$ is equal to an exact form, and therefore it is itself an exact form.

If the system performs an *isothermal reversible transformation*, δQ is an exact differential equal to TdS where S is the entropy of the system. In this case Eq. 7.26 can be written as follows:

$$\int_V \boldsymbol{\sigma} d\boldsymbol{\epsilon} dv = \int_V dV dv - T dS \tag{7.27}$$

In both cases there must exist a 0-form W defined on V so that :

$$\int_V dW = \int_V \boldsymbol{\sigma} d\boldsymbol{\epsilon} dv \tag{7.28}$$

and for this last equation to hold it must be:

$$\frac{\partial W}{\partial \epsilon_{ij}} = \sigma_{ij} \tag{7.29}$$

By direct integration of the forms defining the elastic energy, we can identify W, apart from a gauge transformation, for an adiabatic and for an isothermal transformation respectively as:

$$W = V \tag{7.30}$$

and

$$\int_V W dv = \int_V V dv - TS \tag{7.31}$$

The energy defined in Eq. 7.31 *is not* the free energy of the system. The free energy is defined as:

$$F = U - TS \tag{7.32}$$

where on the right hand side of Eq. 7.31 there is TS, but instead of the internal energy there is only the potential one. Nevertheless the differences of the elastic energy in Eq. 7.31 are the differences of the free energy if the temperature is constant.

7.2.3 Modeling the system

We want now to face the problem of how to compute the critical parameter δ_c of Section 7.2.1 via a molecular dynamics simulation.

The system we consider is a rectangle, in which we want to compute the critical parameter δ when the longest sides are displaced and a cut is made along a straight line (see Fig. 7.6 on page 120). The dimension of the longest side is a and of the smallest is b. The experiment we want to make is depicted is Fig. 7.7. A stress free reference configuration undergoes two thermodynamic transformations, on which the free energy difference between the final configurations and the reference configuration is computed. On one transformation the reference configuration is reversibly pulled by slowly changing the value of δ. On the second transformation a *reversible* straight cut is made inside the material.

The reference configuration Technically a stress free reference configuration at a given temperature is easily realized. It is sufficient to run a Nosé-Hoover dynamics with the appropriate value of ν for a sufficiently long time to obtain an equilibrated configuration, which is also stress free.

The pull transformation In a molecular dynamics simulation a pull transformation is realized by moving at every time step two strips of atoms lying on the longest sides (see Fig. 7.6) so as to displace at the end of the simulation the longest sides of the rectangle to the wanted amount. The atoms on the strip are not allowed to move during the dynamics, and at every time step the strip is moved by a quantity $\Delta(t)$ with respect to its initial position. If $\Delta(t)$ reaches a maximum value Δ_f which is some percentage of the smallest side of the rectangle, the transformation is quasistatic, and reversibility is realized. It should be emphasized that the atoms of the strips do not enter the dynamics of the system, their presence only modifies the potential of the nearby atoms. No dynamical quantity involves their positions, and therefore their presence induces no temperature gradient in the system.

The cut transformation It is not easy to make a reversible cut in a molecular dynamics simulation. The first very simple idea one could have is to make a little cut in the system, to displace it till a crack starts to propagate and cuts the material. Such a transformation is obviously not a quasistatic one, and under such conditions no thermodynamic quantity can

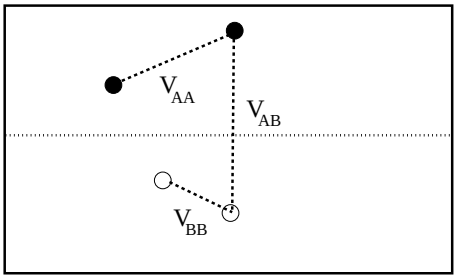

Figure 7.5: *Interaction potentials in a cut experiment. The reference configuration is divided in two zones, A and B. The interaction potentials are V_{AA} and V_{BB} accounting for the interaction between particles belonging to the same zone, and V_{AB} for particles of different zones..*

be computed. Another possibility would be to prepare a configuration with the cut, to relax it, and to draw up the two lips of the crack as to restore the original configuration. If the two parts are drawn up very slowly one may expect to realize a reversible transformation. Unfortunately in practice when the distance of the two free surfaces reaches a critical value, suddenly the cut heals very fast. What is observed is essentially a fracture propagating backwards instead of forwards. A good possibility to realize a reversible cut is to add a time-varying term in the potential. The reference configuration is divided in two zones, A and B, ideally divided by the cut line (Fig. 7.5). Each interaction potential V_{AA} and V_{BB} for the particles belonging to the same zone is the potential V of the system, and does not depend on time. The interaction of the particles of different zones is modulated in time through an explicit time dependence of the potential $V_{AB}(t)$. At the beginning of the transformation the potential is equal to V and goes gradually to zero when the time of the dynamics reaches to final time t_{end} . The general form for $V_{AB}(t)$ is:

$$V_{AB}(t) = \kappa(t)V \tag{7.33}$$

where $\kappa(t)$ is a function sufficiently smooth and differentiable (see next Sections) defined as:

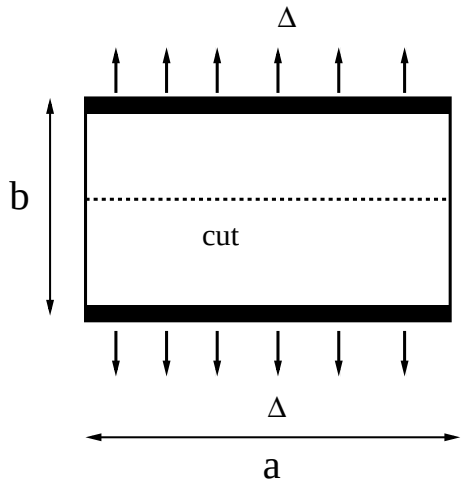

Figure 7.6: *A rectangle in which the longest sides are displaced and a cut is made along a straight line. The atoms in the black strip are kept fixed during the molecular dynamics simulation.*

$$\begin{aligned} \kappa(0) &= 1 \\ \kappa(t) &< 1 \qquad 0 < t < t_{end} \\ \kappa(t_{end}) &= 0 \end{aligned} \tag{7.34}$$

7.2.4 Results via a Nosé-Hoover dynamics.

In this section we present the results of the pull and cut simulations performed in a system of 3889 atoms out of a Tübingen triangle tiling at a temperature $T = 30\%T_M$, where T_M is the melting temperature of the system. The free energy differences are computed using a Nosé-Hoover dynamics (see Section 4.6.1).

The following operating procedure has been implemented to compute free energy differences. A stress free reference configuration has been taken as initial condition of a Nosé-Hoover equilibrium dynamics. Every N_{eq} time steps, and for N_{tot} times[6], the actual positions and velocities of the atoms

[6] N_{tot} is the M defined in Section 4.6.1

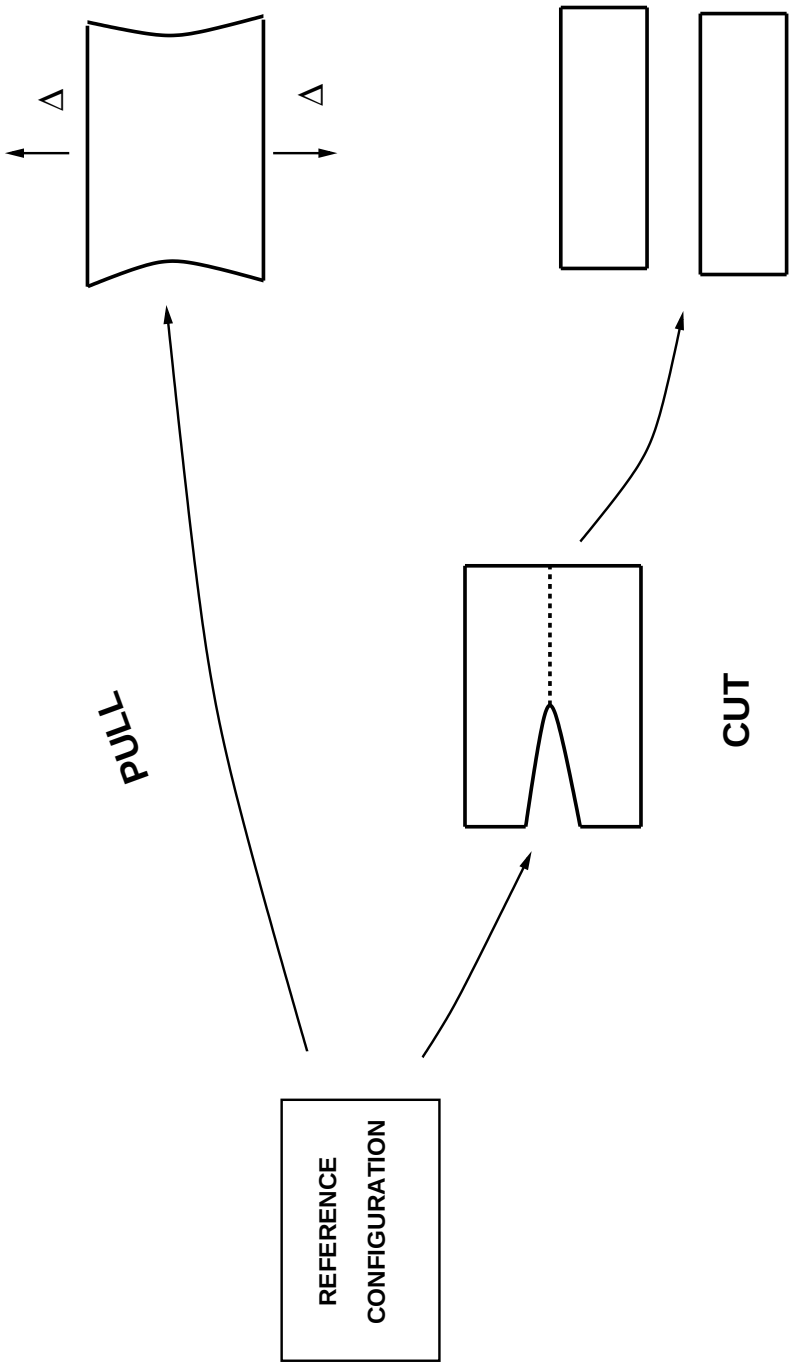

Figure 7.7: *Cut and pull experiment. A stress free reference configuration is pulled and cut.*

are taken as initial condition of a Nosé-Hoover dynamics in which either V_{AB} changes as defined in Eq. 7.33 or the system is pulled. The transformation takes N_{prod} time steps to reach the duration time t_{end}. The transformation velocity v_{prod} is defined as:

$$v_{prod} = \frac{1}{\Delta t N_{prod}} \tag{7.35}$$

where Δt is the simulation time step. When the transformation has finished the system is relaxed over an equilibrium Nosé-Hoover dynamics for further N_{relax} time steps. The N_{tot} values of $\eta(t)$ are collected not only on the N_{prod} steps, but for the entire $\Xi_N = N_{eq} + N_{prod} + N_{relax}$ steps. The entropy difference ΔS per particle over the entire transformation can now be approximated as (see Eq 4.38 on page 83):

$$\Delta S = S(t) - S(0) = -2K\nu \frac{1}{N_{tot}} \sum_{i=1}^{N_{tot}} \int_0^t \eta_i \tag{7.36}$$

and the entropy difference ΔS is expected to have the following behavior:

- It should be zero on the first N_{eq} steps.
- It should change on the next N_{prod} steps.
- It should remain constant on the last N_{relax} steps.

The physical meaning of the N can be summarized as follows:

- N_{eq} is the frequency at which the initial conditions of the transformation dynamics are sampled out of the equilibrium Nosé-Hoover dynamics. N_{eq} should be given a not too small value if one wants to have statistically uncorrelated initial configurations.
- N_{prod} is the crucial parameter tuning the transformation velocity. If N_{prod} is given a too little value the dynamics may become too fast loosing the quasistaticity and consequently the transformation is not anymore reversible.

- N_{relax} is the number of relaxation time steps. N_{relax} should be given a large enough value to detect oscillation on ΔS which may be due to non reversible effects occurring in the transformation.

- N_{tot} is the number of trajectories on which ΔS is computed, and the larger N_{tot} the better is the statistics on ΔS.

The cut simulation

In the cut simulation the influence of the transformation velocity and of the different expressions for the function κ have been investigated.

Linear A linear form of κ:

$$\kappa(t) = -\frac{t}{N_{prod}} + 1 \qquad\qquad t \in [0, N_{prod}] \tag{7.37}$$

has been used in the simulations for different values of N_{prod} corresponding to different transformation velocities. In Fig. 7.8 are shown the entropy S, free energy A and potential energy V in a cut simulation for different values of N_{eq},N_{prod},N_{relax} and N_{tot}. First of all it should be noticed that the entropy is two order of magnitude smaller than the potential energy, and therefore in a cut simulation the free energy is substantially the potential energy. The entropy in Fig. 7.8(a), Fig. 7.8(c) and Fig. 7.8(e), has been calculated for progressively decreasing values of the transformation velocity. In Fig. 7.8(a), which is relative to a value $v_{prod} = 0.00142 w_E$, where w_E is the Einstein frequency, the entropy starts to oscillate at the beginning of the relaxation steps with an amplitude which is much bigger than the statistical error. The entropy of Fig. 7.8(e) has been calculated on a process three times slower than the slowest of Fig. 7.8(a), but nevertheless there are residual oscillations in the relaxation regime. This oscillating behavior indicates that the transformation is too fast and non reversible. The reason of the nonreversibility lies not in the velocity of the cut process, but depends on the analytical form of κ. For a linearly decreasing potential the cut transformation is *always* non reversible, independently from its velocity.

Quadratic The quadratic form of κ:

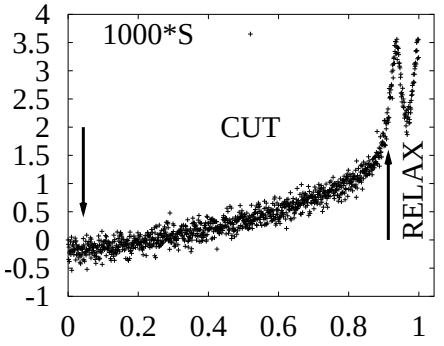

(a)
$v_{prod} = 0.00142 w_E$ $N_{tot} = 1600$

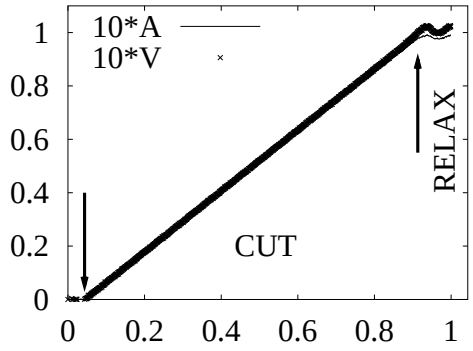

(b) Same as in (a)

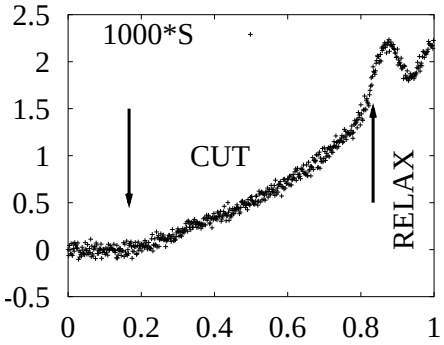

(c) $v_{prod} = 0.00118 w_E$ $N_{tot} = 700$

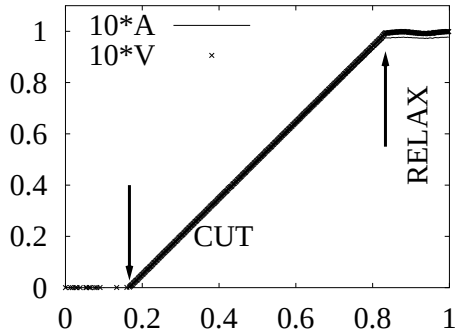

(d) Same as in(c)

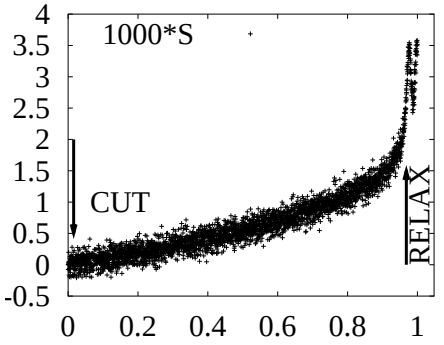

(e) $v_{prod} = 0.00039 w_E$ $N_{tot} = 1600$

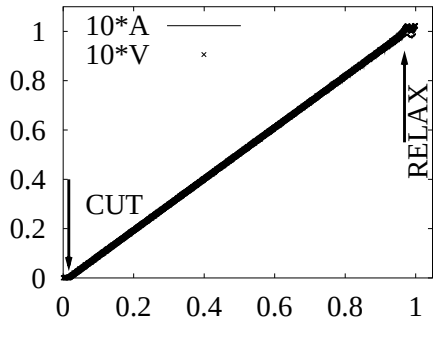

(f) Same as in (e)

Figure 7.8: *Entropy S, free energy A and potential energy V in a cut simulation for a linear decrease of κ and for different values of v_{prod} and N_{tot}. The x axis is in Ξ_N units.*

$$\kappa(t) = \frac{1}{N_{prod}^2}t^2 - \frac{2}{N_{prod}}t + 1 \qquad t \in [0, N_{prod}] \tag{7.38}$$

has been chosen to test the permanence of the oscillations detected in the linear case.

Even if in the relaxation regime the oscillations of the entropy, calculated at the highest velocity, are smaller (see Fig. 7.9.(a)), they are nevertheless present, and the quadratic form of κ does not seem to eliminate the irreversible behavior.

A nine degree polynomial A polynomial of nine degree:

$$\begin{aligned} \kappa(t) &= 1 - \tau^5(70\tau^4 - 315\tau^3 + 540\tau^2 - 420\tau + 126) \\ \tau &= \frac{t}{N_{prod}} \qquad t \in [0, N_{prod}] \end{aligned} \tag{7.39}$$

already used in other similar free energy calculations [80], has given very satisfactory results.

The entropy of Fig. 7.9.(c), which has been calculated at the same highest velocity of Fig. 7.8.(a), has a much smoother behavior. The entropy increases very mildly at the beginning of the transformation, and reaches its plateau value already before the beginning of the relaxation phase.

The pull transformation.

Like for the cut case, also in the pull simulation the influence of the transformation velocity and of different expressions of the function Δ have been investigated.

Linear A linear form for Δ has been tested:

$$\Delta(t) = \frac{t}{N_{prod}}\Delta_f \tag{7.40}$$

for $\Delta_f = 2.047\%b$, and where b is the longest side of the rectangle (see Fig. 7.6). At the very high velocity $v_{prod} = 0.00237 w_E$ the system shows already a reversible behavior even for a linearly decreasing pulling function $\Delta(t)$ (see Fig(7.10)).

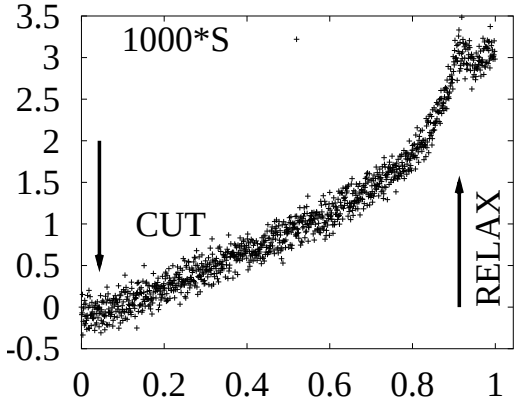

(a) $v_{prod} = 0.00142 w_E$ $N_{tot} = 1600$

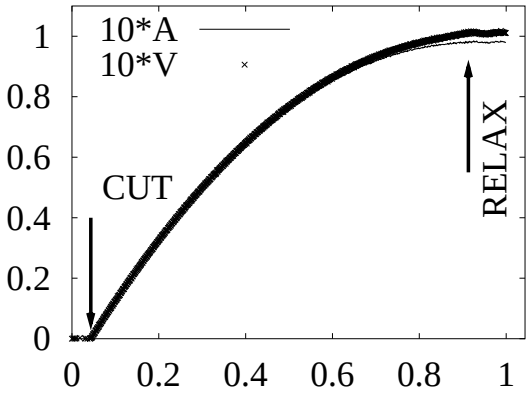

(b) Same as in (a)

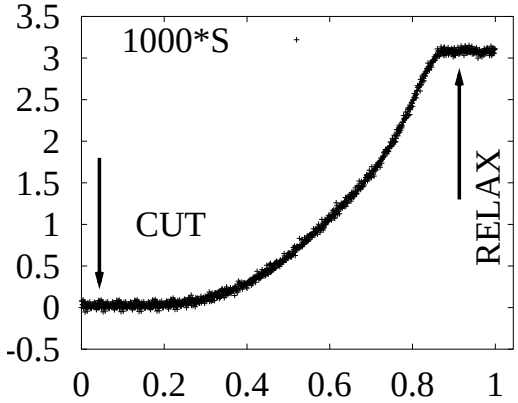

(c) $v_{prod} = 0.00142 w_E$ $N_{tot} = 1600$

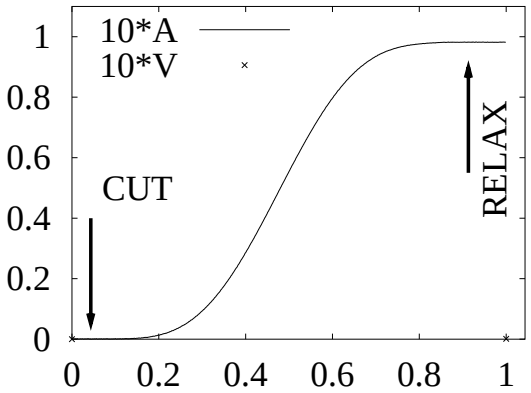

(d) Same as in (c)

Figure 7.9: *Entropy S, free energy A and potential energy V in a cut simulation for a parabolic ((a) and (b)) and a nine degree polynomial ((c) and (d)) decrease of κ, and for different values of v_{prod} and N_{tot}. The x axis is in Ξ_N units.*

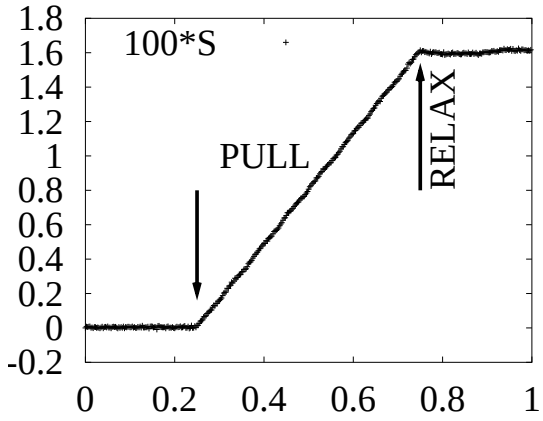

(a) $v_{prod} = 0.00237 w_E$ $N_{tot} = 1600$

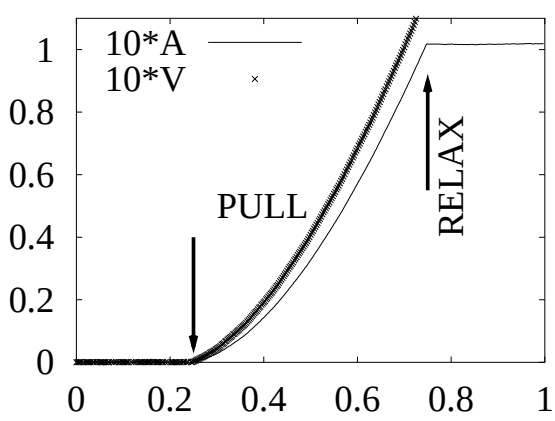

(b) Same as in (a)

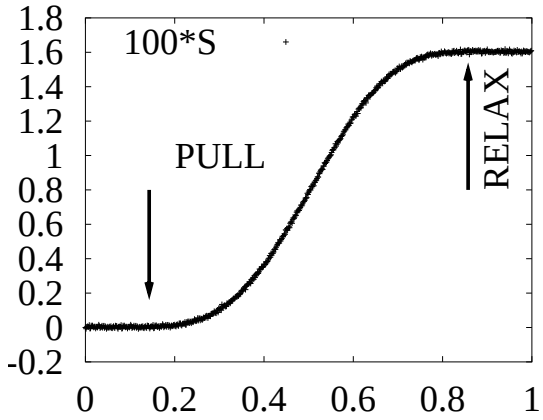

(c) $v_{prod} = 0.00237 w_E$ $N_{tot} = 1600$

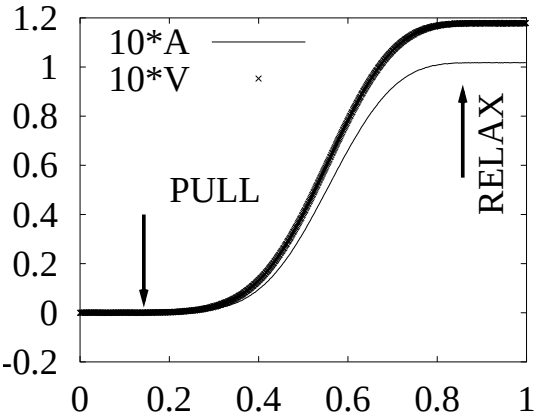

(d) Same as in (c)

Figure 7.10: *Entropy S, free energy A and potential energy V in a pull simulation for a linear ((a) and (b)) and a nine degree polynomial pulling function Δ ((c) and (d)), and for different values of v_{prod} and N_{tot}. The x axis is in Ξ_N units.*

A nine degree polynomial The nine degree polynomial:

$$\begin{aligned} \Delta(t) &= \tau^5(70\tau^4 - 315\tau^3 + 540\tau^2 - 420\tau + 126)\Delta_f \\ \tau &= \frac{t}{N_{prod}} \qquad t \in [0, N_{prod}] \end{aligned} \tag{7.41}$$

used to pull the sample gives essentially the same results of the linear pulling function (see Fig(7.10)). In the pull simulation the system shows a reversible behavior already for very fast velocities and independently from the analytical form of $\Delta(t)$.

7.2.5 Results via an umbrella sampling.

In this section the results of the simulations performed in the same system and temperature of Section 7.2.4 are presented. The free energy differences are computed using an umbrella sampling.

The umbrella sampling method for computing free energy differences is intrinsically different from a method based on a Nosé-Hoover dynamics. In the umbrella sampling the system is *always at equilibrium* (cf Section 4.6.3). There is neither production dynamics, nor a relaxation phase. The only free variable is the number of points in which the variation domain of the thermodynamic parameter can be subdivided. Therefore there are no problems due to the non reversibility of the process, but eventually only to a lack of statistics if the discretization is too coarse grained.

The following operating procedure has been implemented to compute free energy differences for both the cut and pull simulation. The variation domain of the thermodynamic parameter is divided into N points. In the cut simulation this is equivalent to choose N values for κ between 0 and 1:

$$\begin{gathered} 0 \leq \kappa_i \leq 1 \qquad \kappa_i < \kappa_{i+1} \qquad i = 1, \cdots, N \\ \kappa_1 = 0 \qquad \kappa_N = 1 \end{gathered} \tag{7.42}$$

and for Δ in the pull:

$$\begin{gathered} 0 \leq \Delta_i \leq 1 \qquad \Delta_i < \Delta_{i+1} \qquad i = 1, \cdots, N \\ \Delta_1 = 0 \qquad \Delta_N = \Delta_f \end{gathered} \tag{7.43}$$

A stress free reference configuration has been taken as initial condition of a Nosé-Hoover equilibrium dynamics, on which the thermodynamic parameter assumes the N values of Eq. 7.42 and Eq. 7.43. As soon as the thermodynamic transformation has made the new step i, with $1 \leq i \leq N$, the dynamics runs for $N_{tot} = N_{out} + N_f N_{prod}$ time steps. The system is given a sufficient number of N_{out} time steps to equilibrate. Then for N_{prod} times and every N_f time steps the energy difference of Eq. 4.50 on page 86 is computed on the actual values of positions and velocities by only giving the free parameter the next $(i+1)$th value. In the pull simulation this is equivalent to calculate the energy difference on a equilibrated configuration of positions and velocity at a displacement Δ_i, with the configuration obtained by displacing **only** the atoms of the strip to the next value of Δ_{i+1}. The N_{prod} energy differences ΔH_k are used to approximated the free energy difference of Eq. 4.52:

$$\Delta A_{i,i+1} = A_{i+1} - A_i = -KT \log(\frac{1}{N_{prod}} \sum_{k=1}^{N_{prod}} \exp(-1/KT\Delta H_k)) \qquad (7.44)$$

All the $N-1$ contributions of Eq. 7.44 are summed up to give the free energy difference on the entire transformation:

$$A_N - A_1 = \sum_{i=1}^{N-1} \Delta A_{i,i+1} \qquad (7.45)$$

where A_N is the free energy of the configuration cut, or displaced of Δ_f, and A_1 is the free energy of the stress free configuration.

The statistical meaning of N, N_{out}, N_f and N_{prod} can be summarized as follows:

- The parameter N is the crucial parameter of the umbrella sampling. If N is given a too large value, the energies ΔH_k may become too high, and the free energy $\Delta A_{i,i+1}$ may become underestimated (cf. Section 4.6.3 on page 86).

- When the transformation enters the ith step the system should have enough N_{out} time steps to equilibrate.

- N_f is the frequency at which the energy difference ΔH_k is computed. If N_f is too small the values of the ΔH_k may be too correlated.

- N_{prod} is the number of independent and uncorrelated energies ΔH_k. The bigger N_{prod}, the better becomes the statistics on the free energy difference of Eq. 7.44

Let us now analyze the numerical results of the umbrella sampling method.

The cut simulation In the cut simulation the free energy difference has been found to be practically the same for two values $N = 50$ and $N = 100$ (see Fig. 7.11.(a)).

The pull simulation In the pull simulation the free energy difference has been calculated using three values $N = 50$, $N = 100$ and $N = 200$. The free energy in this case is affected by the number of the points in which the thermodynamic free parameter is divided (see Fig. 7.11.(b)).

7.2.6 Comparison of the two methods.

The methods based on the Nosé-Hoover dynamics and on the umbrella sampling for the calculation of the free energy of Section 7.2.4 and Section 7.2.5 give numerically equivalent results (see Fig. 7.12).

Computationally the Nosé-Hoover free energy calculation is much more expensive than the umbrella method. In Table 7.2 the time for the pull and cut simulations for the two different methods are reported. The umbrella sampling for such calculations should be doubtless preferred to a Nosé-Hoover method, which may nevertheless find a good and competitive applicability in all the situations where one aims at computing the entropy on a transformation where the temperature is a varying parameter. In such a case an umbrella sampling method, which has been defined under the assumption that the temperature is constant, cannot be applied, meanwhile in deriving the expression of the entropy in the Nosé-Hoover method no restrictions on the temperature have been made.

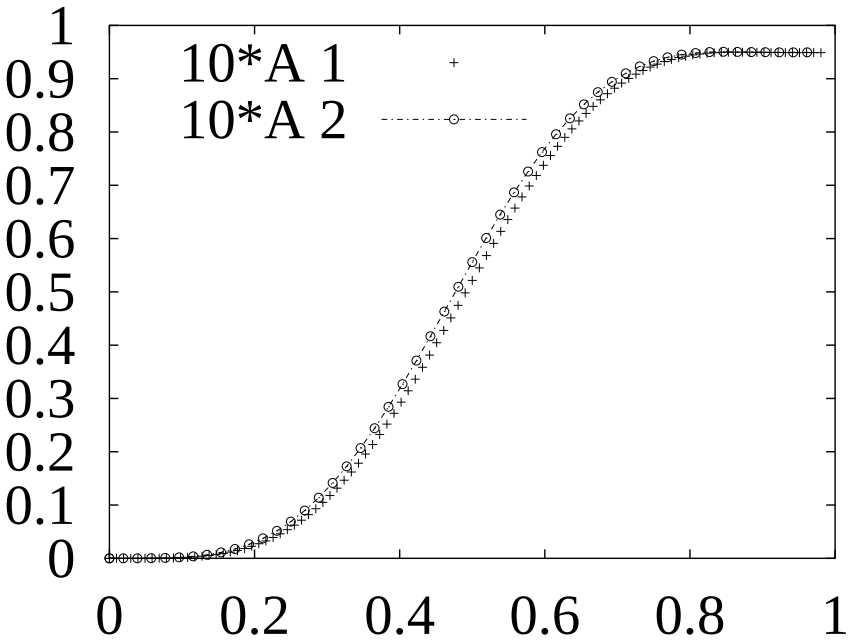

(a) $N = 100$ (A1), $N = 50$ (A2)

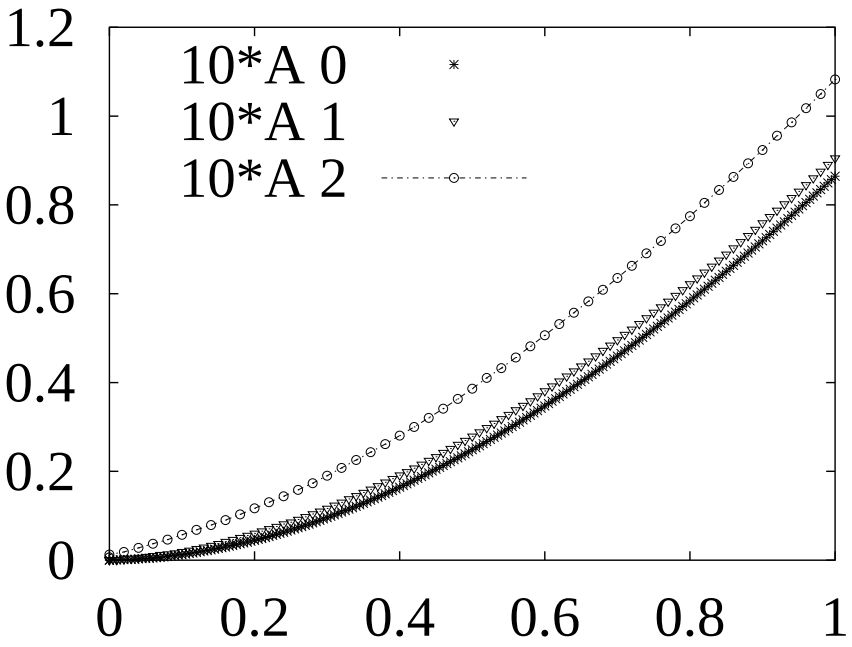

(b) $N = 200$ (A0),$N = 100$ (A1),$N = 50$ (A2)

Figure 7.11: *Free energy computed with the umbrella sampling in the cut (a)*

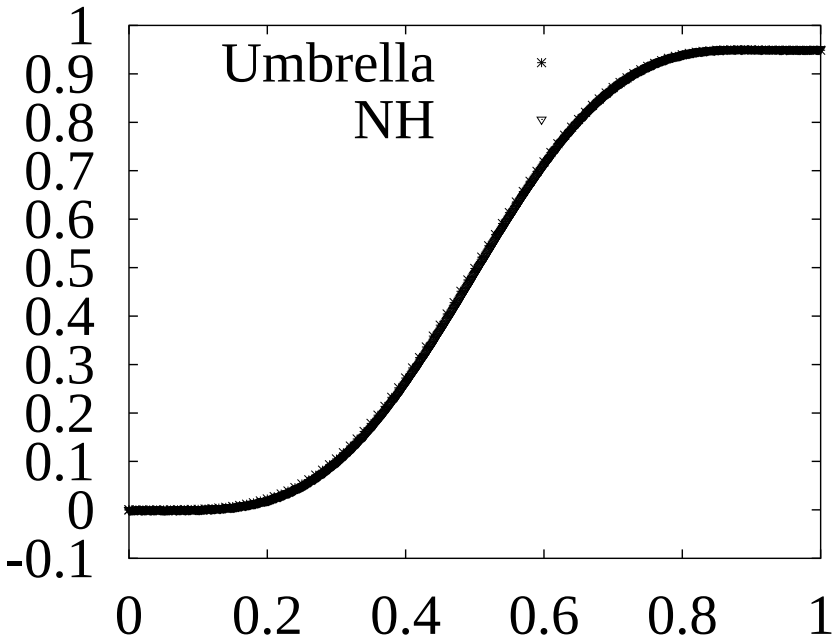

(a) Pull

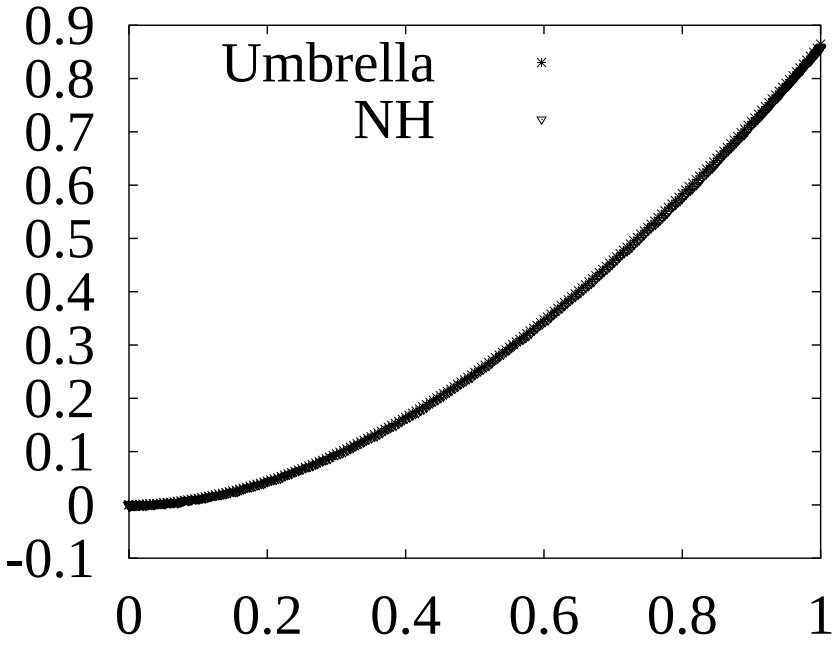

(b) Cut

Figure 7.12: *Free energy computed with the umbrella sampling and the Nosé-*

	NH dynamics (hours)	Umbrella (hours)	NH/Umbrella
CUT	95.35	4.51	21.14
PULL	60.67	8.25	7.35

Table 7.2: *Timing in hours of the pull and cut simulation for the two free energy simulations performed with a Nosé-Hoover method and an umbrella sampling.*

7.3 Results at various temperatures

In this section we present the results of the simulations for the estimation of the surface free energy, the pull energy and the elastic constants in a binary system of 4134 atoms derived from a Tübingen triangle tiling. The simulations have been performed at various temperatures below the melting temperature T_M of the system. All the free energies have been computed using the umbrella sampling.

7.3.1 Surface energies

In two dimensions the surface energy γ of a line L inside a material is one half[7] the energy per unit length necessary to make a cut along L, and it can be measured with a cut simulation. In a cut simulation the free energy difference ΔA_{cut} of a system cut along L with respect to the reference configuration can be measured. If l is the length of the line L the surface energy γ is:

$$\gamma = \frac{1}{2}\frac{\Delta A_{cut}}{l}. \tag{7.46}$$

The dimensions of γ are those of a force, and γ is actually the force the material offers when it is cut along L. The free energy difference ΔA_{cut} can be viewed as the work an external force $\mathbf{F}_{cut}$ has to perform on the system to make the cut. If the material is homogeneous and the cut is straight ΔA_{cut} depends linearly on the length of the cut. In this case the force $\mathbf{F}_{cut}$ is constant, has the direction of the line but it opposes to the creation of a free surface. The value of $\mathbf{F}_{cut}$ is then:

[7]One half because two free surfaces are formed in a cut, and each of them contributes in equal part to the energy variation of the system.

$$\mathbf{F}_{cut} = -2\gamma \tag{7.47}$$

which is the same force of Eq. 3.31 on page 60.

Four cut simulations have been performed in the quasicrystal along the lines 1,2,3 and 4 of Fig. 5.3. The last three lines are easy lines for dislocation emission, and the first is the line connecting the centers of the ten atoms clusters. The values of γ per particle on the different lines and at various temperatures are reported in Table 7.3 and in Fig. 7.13.

The surface energy on the line 1 connecting the clusters is the biggest. It costs more energy to make a cut breaking the clusters than opening a surface between them. The lowest surface energy is on the line 4, which is in the middle of the biggest separation between lines of type 1, i.e. it costs the lowest energy to open a surface remaining the farthest away from the dense packed clusters.

On the same line a linear dependence of γ:

$$\gamma = \alpha \frac{T}{T_M} + \beta \tag{7.48}$$

has been fitted against the data of Table 7.3, giving a good agreement with relative errors of at most 5%. The results of the fit are collected in Table 7.3.

The surface energy on the same line decreases with temperature, even if the temperature dependence is not strong. The surface energy at the highest temperature is always around 12% less than the energy at the lowest temperature.

7.3.2 The elastic constants

In the *linear* theory of elasticity the density of energy in two dimensions per unit of volume stored in a material is:

$$2W = (\lambda + 2\mu)\left[\left(\frac{\partial u}{\partial x}\right)^2 + \left(\frac{\partial v}{\partial y}\right)^2\right] + \mu\left(\frac{\partial u}{\partial y} + \frac{\partial v}{\partial x}\right)^2 + 2\lambda\left(\frac{\partial u}{\partial x}\right)\left(\frac{\partial v}{\partial y}\right) \tag{7.49}$$

$\gamma/10^{-4}$	line 1	line 2	line 3	line 4
$15\%T_M$	6.2447	6.0338	5.6838	5.1834
$31\%T_M$	6.0787	5.8804	5.5413	5.0319
$47\%T_M$	5.9647	5.7719	5.4470	4.9604
$63\%T_M$	5.8163	5.6409	5.2824	4.8134
$78\%T_M$	5.6556	5.4625	5.1230	4.6763
$94\%T_M$	5.4355	5.3557	4.9371	4.5781
$\alpha/10^{-5}$	-9.9907	-8.73159	-9.42215	-7.75369
$\beta/10^{-4}$	6.41229	6.16842	5.85109	5.29795

Table 7.3: *Surface energy γ per particle for various temperatures and on different lines.*

where u and v are respectively the x and y components of the displacement field.

The elastic constants can be calculated using the analytical expression of the elastic energy fitted against the free energy in a pull and in an expand experiment.

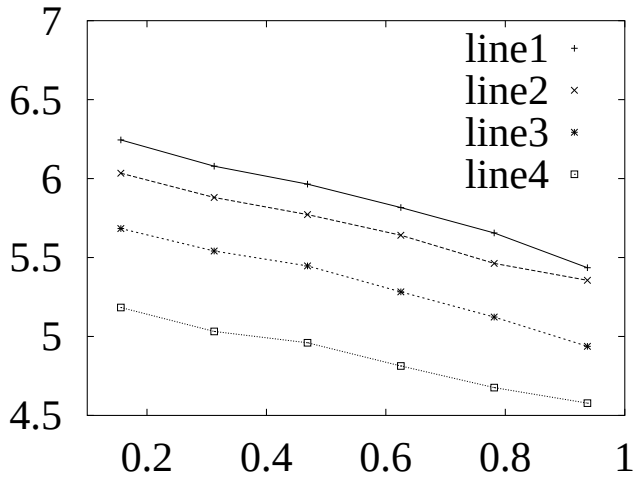

Figure 7.13: *Surface energies on different lines versus T/T_M.*

Pull experiment

The displacement components in a pull experiment, where the longest sides of the rectangle in Fig. 7.6 are displaced by an amount Δ, read:

$$\begin{aligned} u &= x\frac{\Delta}{b} \\ v &= 0 \end{aligned} \tag{7.50}$$

where b is the length of the shortest side of the rectangle. The density of Eq. 7.49 integrated over the volume V of the rectangle gives the elastic energy E stored in the sample:

$$E = \frac{1}{2}(\lambda + 2\mu)(\frac{\Delta}{b})^2 V. \tag{7.51}$$

In a pull experiment the free energy, whose differences are at constant temperature the elastic energy of Eq. 7.51, can be measured as a function of the displacement Δ.

In Fig. 7.14 is depicted the elastic energy $E/V * 10^6$ per particle versus Δ/b. The elastic energy stored in the sample when it is pulled of the same amount Δ/b decreases with increasing temperature. A material becomes softer when its temperature is increased, therefore it must be more strained to load the same elastic energy. A quadratic dependence of E on Δ/b has not well fitted the experimental data. A third degree polynomial function:

$$E/V = \alpha(\frac{\Delta}{b})^2 + \beta(\frac{\Delta}{b})^3 \tag{7.52}$$

describes very well the elastic energy for the values of α and β reported in Table 7.4. The value of the displacement Δ_{anela} beyond which the quasicrystal elastic energy has not any more the linearized form of Eq. 7.51 can be found by imposing that:

$$E/V = \alpha(\frac{\Delta}{b})^2 + \beta(\frac{\Delta}{b})^3 = \alpha(\frac{\Delta}{b})^2 \left(1 + \frac{\beta}{\alpha}\frac{\Delta}{b}\right) \approx \alpha(\frac{\Delta}{b})^2 \tag{7.53}$$

which in terms of Δ_{anela} means:

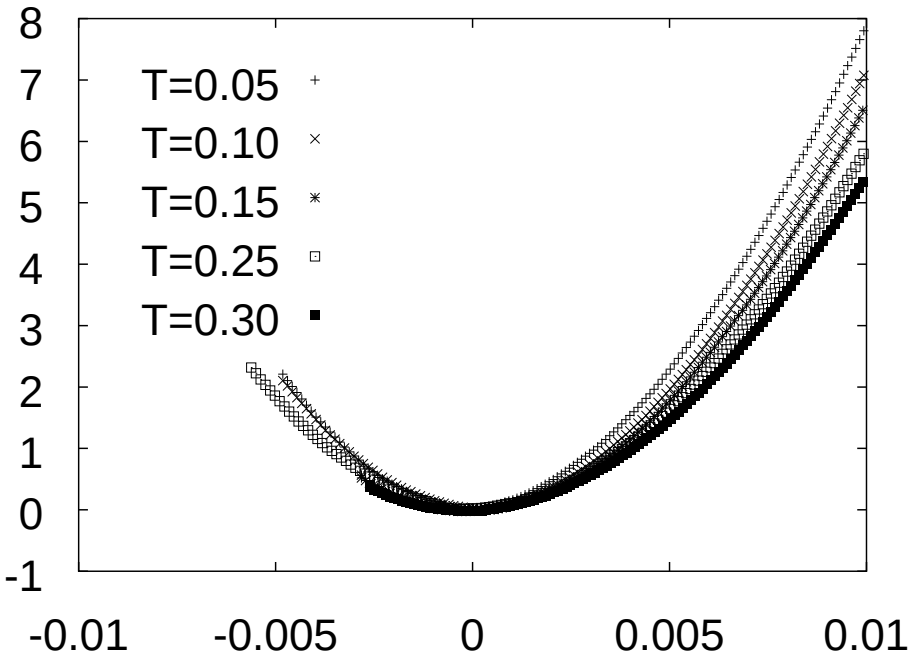
8
7
6
5
4
3
2
1
0
-1
-0.01
-0.005
0
0.005
0.01
T=0.05
T=0.10
T=0.15
T=0.25
T=0.30

(a)

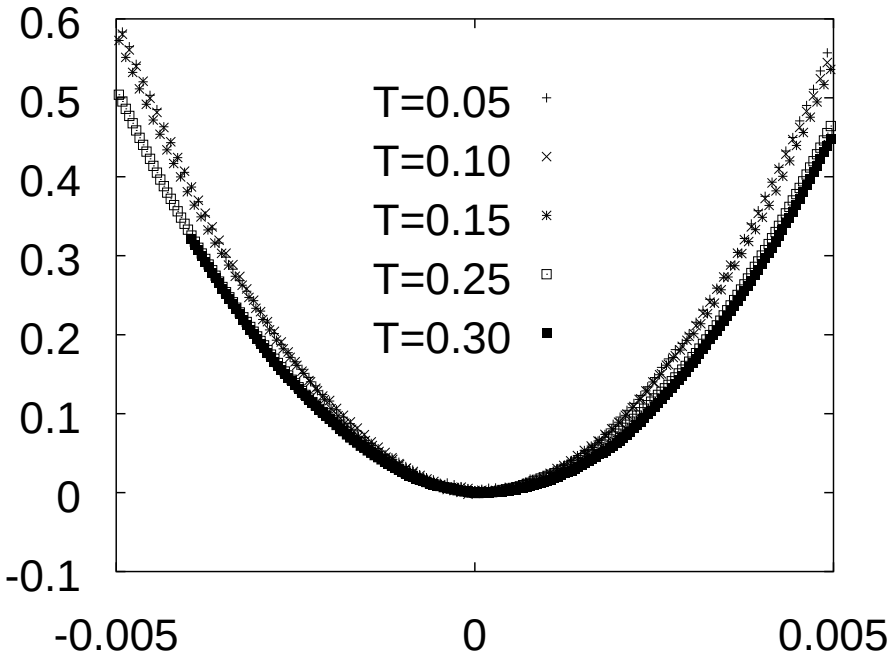
0.6
0.5
0.4
0.3
0.2
0.1
0
-0.1
-0.005
0
0.005
T=0.05
T=0.10
T=0.15
T=0.25
T=0.30

(b)

	$\alpha * 10^2$	$\Delta\alpha * 10^2$	$\beta * 10^2$	$\Delta\beta * 10^2$	Δ_{anela}/b
$15\%T_M$	9.02415	0.0216 (0.2394%)	-1.15558	0.0124 (1.078%)	0.007809
$31\%T_M$	8.08589	0.0124 (0.1534%)	-0.92758	0.0071 (0.771%)	0.008717
$47\%T_M$	7.43432	0.0082 (0.1107%)	-0.81061	0.0055 (0.682%)	0.009171
$63\%T_M$	7.12151	0.0121 (0.1706%)	-0.83107	0.0090 (1.095%)	0.008569
$78\%T_M$	6.72678	0.0100 (0.1500%)	-0.83568	0.0060 (0.726%)	0.0080494
$94\%T_M$	6.25072	0.2179 (0.3486%)	-0.82345	0.0218 (2.653%)	0.007590

Table 7.4: *Coefficients α and β with relative errors.*

$$\frac{\beta}{\alpha}\frac{\Delta}{b} \approx \epsilon \qquad \epsilon << 1. \tag{7.54}$$

In Table 7.4 the values of Δ_{anela} for various temperatures and for $\epsilon = 0.1$ are reported. The quasicrystal enters the anelastic regime even for relatively small values of the displacement Δ/b. The cubic term in the elastic energy becomes important already when Δ is around 1% of the dimension along which the material is strained . It should be stressed that the material has undergone *no plastic* deformation, for no dislocation has appeared somewhere in the sample during the transformation.

The shear experiment

With a simple pull experiment it is possible to measure the sum of the elastic constants λ and μ. A second deformation is needed in order to separate the contributions of the two constants in the elastic energy. The value of μ can be measured in a *shear* experiment, where the two longest sides of the rectangle are shifted by the same amount Δ with respect to each other (see Fig. 7.15).

The displacement field for this transformation reads:

$$\begin{aligned} u &= 0 \\ v &= \frac{2x}{b}\Delta \end{aligned} \tag{7.55}$$

where b is the shortest side of the rectangle[8]. The elastic energy per unit of

[8]It would be theoretically equivalent to keep one side fixed and to shift the other by 2Δ. Numerically such a transformation might produce too high shears in the sample and can easily induce dislocation emission.

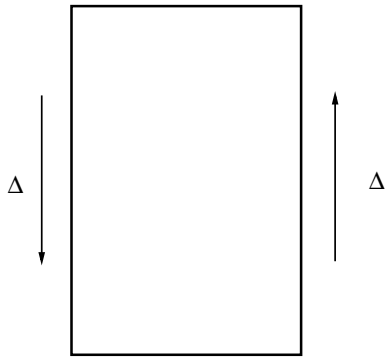

Figure 7.15: *In a shear transformation the two longest sides of the rectangle are shifted by the same amount* Δ *with respect to each other*

volume depends only on the elastic constant μ:

$$E/V = 2\mu \left(\frac{\Delta}{b}\right)^2 \tag{7.56}$$

The elastic energy per unit of volume and per particle of Eq. 7.56 has been measured as a function of Δ at different temperatures, and is depicted in Fig. 7.14(b). Once again the elastic constant μ decreases upon increasing the temperature. The elastic energy has been fitted against the third degree polynomial:

$$E/V = \sigma(\frac{\Delta}{b})^2 + \varsigma(\frac{\Delta}{b})^3 \tag{7.57}$$

and the values of the fit parameters with the relative errors are reported in Table 7.5.

It is reasonable that the value of Δ_{anela}, beyond which the anelastic contribution to the elastic energy becomes important, is much bigger than in the pull experiment. In a shear experiment the relative distance between the atoms changes less with Δ than when the sample is compressed or expanded of the same amount. Therefore the system must be more sheared to enter the same anelastic zone of the potential which accounts for the anelastic contribution to the energy of Eq. 7.57.

	$\sigma * 10^2$	$\Delta\sigma * 10^2$	$\varsigma * 10^2$	$\Delta\varsigma * 10^2$	Δ_{anela}/b
$15\%T_M$	2.32313	0.001803 (0.0776%)	-3.81895	0.2203 (5.768%)	0.060831
$31\%T_M$	2.26713	0.002576 (0.1136%)	-6.90823	0.3147 (4.555%)	0.032817
$47\%T_M$	2.21787	0.002039 (0.0919%)	-5.65358	0.2491 (4.407%)	0.039229
$63\%T_M$	2.15920	0.001511 (0.0699%)	-7.19595	0.1846 (2.565%)	0.030005
$78\%T_M$	1.93986	0.001257 (0.0648%)	-5.89387	0.1540 (2.613%)	0.032913
$94\%T_M$	1.71668	0.006326 (0.3212%)	-3.06499	0.1313 (4.282%)	0.006426

Table 7.5: *Coefficients α and β with relative errors.*

	μ	$\Delta\mu$	λ	$\Delta\lambda$
$15\%T_M$	45.1730	0.035039	611.553	1.75
$31\%T_M$	44.0841	0.050090	540.749	1.06
$47\%T_M$	43.1266	0.039628	491.989	1.71
$63\%T_M$	41.9856	0.029361	469.938	2.99
$78\%T_M$	37.7205	0.024422	447.767	1.82
$94\%T_M$	33.3804	0.123009	419.416	2.44

Table 7.6: Elastic constants λ and μ at different temperatures.

The elastic constants

The values of the elastic constants λ and μ at different temperatures can be easily calculated from the values of the coefficients α and σ in the Table 7.5 and Table 7.4, and are reported in Table 7.6.

A linear dependence of λ and μ versus T/T_M (see Fig. 7.16) does not fit the measured data. It should be necessary to thicken the measures of the elastic constants versus the temperature to gain a more precise idea of their analytical temperature dependence. A full extensive analysis of the temperature dependence of the elastic constants is not the primary objective of this work, and it might be the subject of a future work.

7.3.3 The critical displacement

The critical displacement Δ_C is the value of Δ at which the elastic energy of Eq. 7.52 equals the energy necessary to cut the sample along a line:

$$E(\Delta_C) = \Delta A_{cut} \tag{7.58}$$

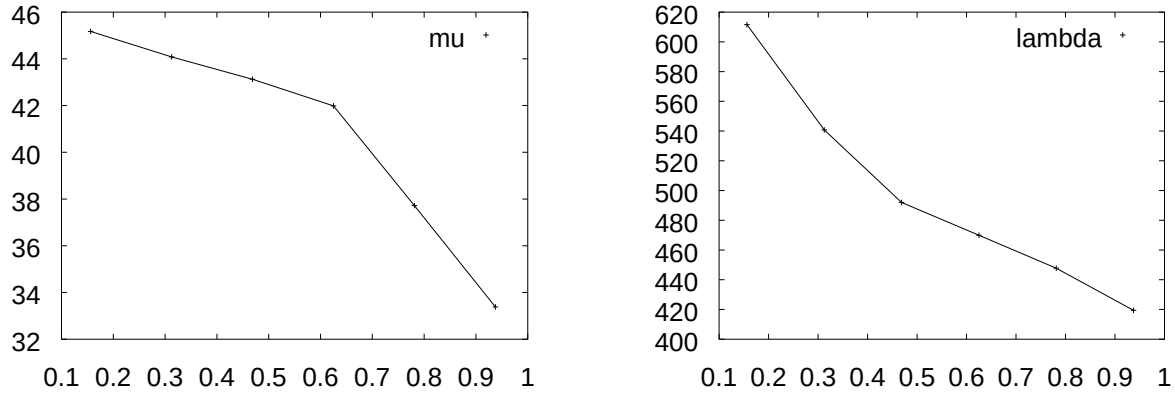

(a) (b)

Figure 7.16: *Elastic constants μ and λ (in (a) and (b)) versus T/T_M*

where A_{cut} is the free energy of Eq. 7.46 on page 133. The critical displacement can be found by solving numerically the equation:

$$V\left(\alpha\left(\frac{\Delta_C}{b}\right)^3+\beta\left(\frac{\Delta_C}{b}\right)^2\right)=2\gamma l \tag{7.59}$$

where V is the volume of the sample, α and β are the coefficients of E in Eq. 7.52 on page 136, γ is the surface energy and l is the length of the cut (see Section 7.3.1 on page 133).

The Eq. 7.59 has been solved for the various temperatures at which the surface energy and the coefficients α and β have been computed. The values of Δ_C/b for the lines 1,2,3 and 4 are reported in Table 7.7, and in Fig. 7.17 is depicted the critical displacement on the different lines as a function of temperature.

A linear dependence of Δ_C/b on the temperature:

$$\frac{\Delta_C}{b}=\varsigma\frac{T}{T_M}+\chi \tag{7.60}$$

has been fitted against the values reported in the table, and has given a satisfactory accord within 5%. The values of ς and χ are reported in Table 7.7.

	line 1	line 2	line 3	line 4
$15\%T_M$	0.021563	0.021111	0.020355	0.019256
$31\%T_M$	0.022138	0.021702	0.020946	0.019788
$47\%T_M$	0.022787	0.022344	0.021589	0.020434
$63\%T_M$	0.023371	0.022936	0.022038	0.020842
$78\%T_M$	0.024176	0.023649	0.022717	0.021474
$94\%T_M$	0.025150	0.024904	0.023614	0.022501
ς	0.0045043	0.0046442	0.0040332	0.0039663
χ	0.0207342	0.0202345	0.0196708	0.0185467

Table 7.7: *Values of Δ_C/b, ς and χ on different lines versus T/T_M.*

It is reasonable that the critical displacement increases with the increase of temperature. A material at high temperature becomes softer, and a bigger load is needed to store in the system the same amount of elastic energy (see Section 7.3.2 on page 134). Conversely the surface energy does not depend much on temperature, and therefore the sample has to be more loaded in order to reach the same amount of elastic energy needed to form the cut.

7.3.4 Numerical check of the critical displacement

The critical displacement computed in the previous section has been numerically checked on the system where it has been computed.

Two simulations of a long Nosé-Hoover dynamics at $T = 15\%T_M$ have been performed. In both simulations a crack has been put in the system using the procedure of Section 6.1 on page 97. In the first simulation the crack lies on the line 4 and the atoms on the longest side of the rectangular sample have been displaced at the critical displacement on line 4. In the second simulation the crack lies on line 1 and the atoms on the upper and lower boundary have been displaced at the critical displacement of line 1.

In Fig. 7.18(a) the final configuration of the crack lying on line 4 shows that the crack is in equilibrium. The crack does not propagate further, and *no dislocation* has been emitted.

In Fig. 7.18(b) the final configuration of the crack shows that also in this case the crack is in equilibrium. The crack does not propagate further, but from the crack tip a dislocation has been emitted, in accord with the expectations of the linear theory of elasticity (see Section 8.2.2 on page 147).

The next chapter contains the results of the simulations of fracture propagation at different temperatures performed in a sample of many atoms (74210). For each temperature, crack propagation has been investigated in detail at different loads. In Chapter 8 by means of numerical elastic estimates based on the results of this chapter, for the first time an explanation of the mechanisms of dislocation emission and crack propagation in the range of low loads and low temperatures is being proposed.

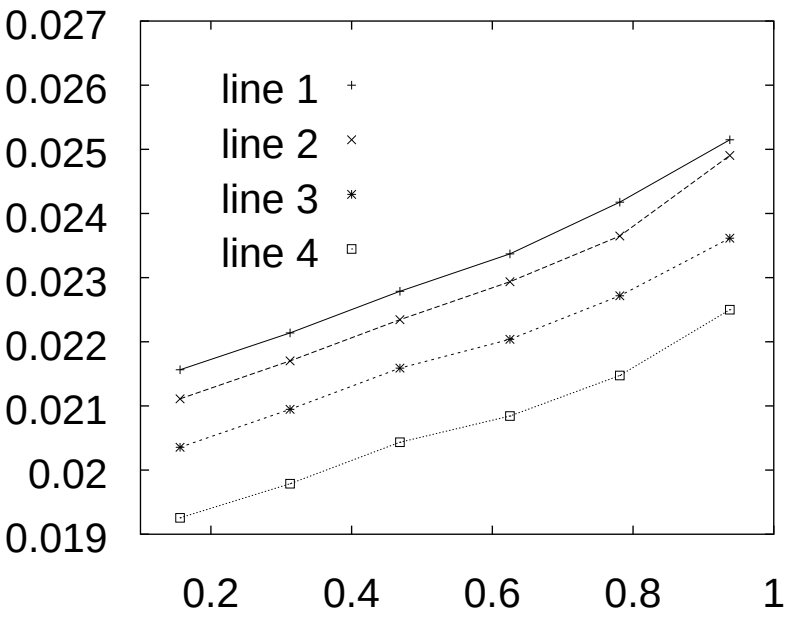

Figure 7.17: *Values of Δ_C/b on the different lines versus the temperature.*

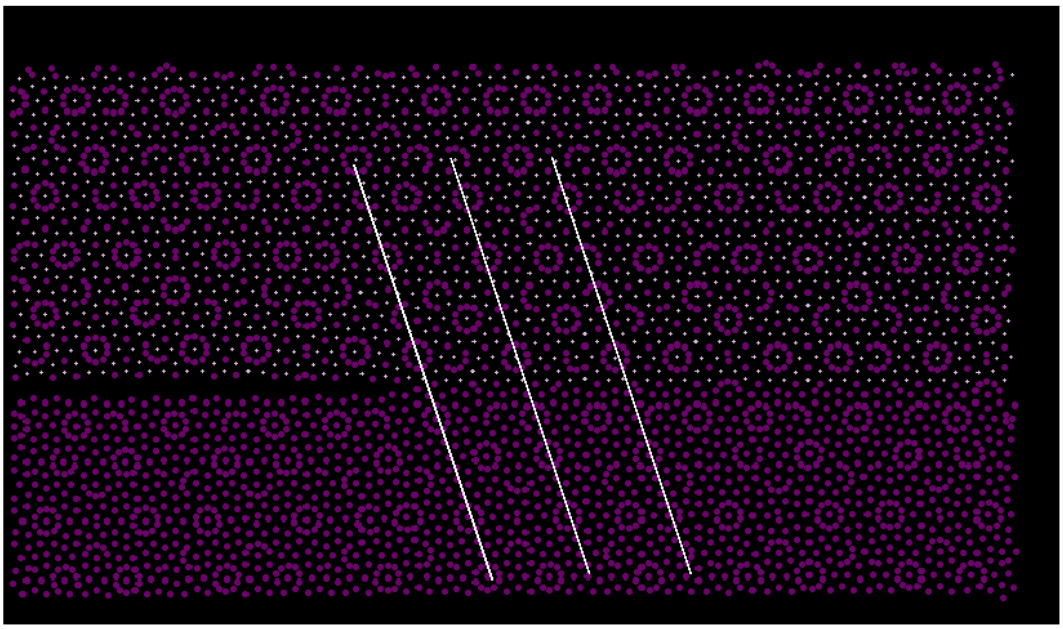

(a)

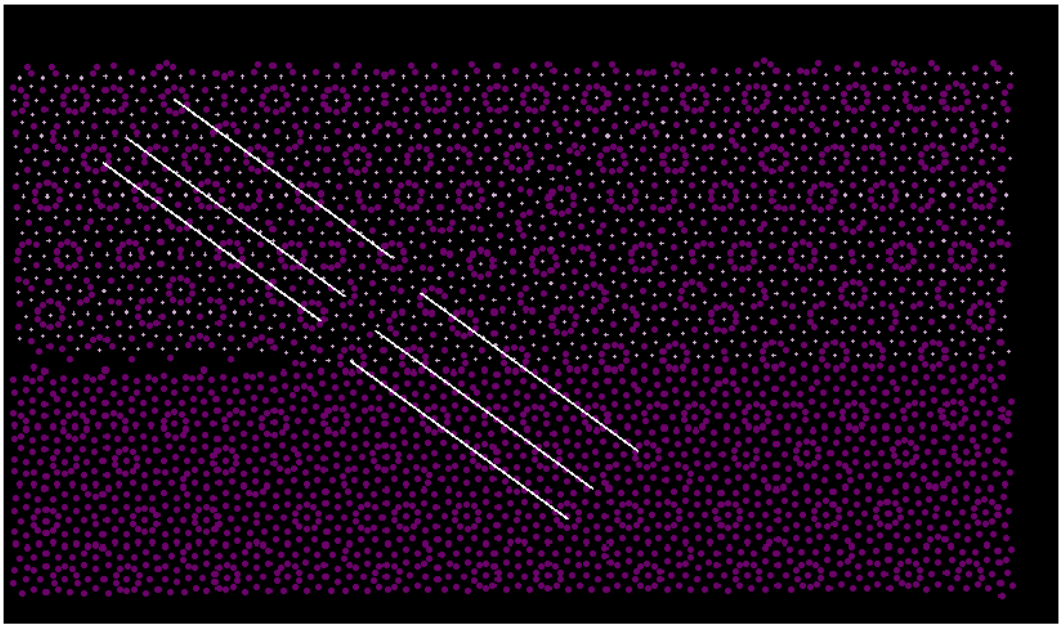

(b)

Figure 7.18: *(a) Crack at the critical displacement on line 4 (a) and on line 1 (b). In (a) the lines connecting the clusters in front of the crack tip are intact, and therefore no dislocation has been emitted from the crack tip. In (b)the lines connecting the clusters in front of the crack tip are broken and shifted. A dislocation has been emitted from the crack tip.*

Chapter 8

RESULTS IN A BIG SAMPLE

8.1 Introduction

In this chapter we will present the results of the crack propagation simulations performed at different temperatures below the melting temperature T_M of a sample of 74210 atoms out of a Tübingen triangle tiling.

The chapter is divided into two parts: a preliminary part devoted to the peculiarities of dislocation emission in quasicrystals, and one containing the simulations performed at low and high temperatures.

The division in low, intermediate and high temperatures comes from the characteristic of crack propagation in this three regimes.

For low temperatures crack propagation takes place with much ease. At temperatures below $T = 41\%T_M$ a crack always propagates when it is loaded beyond its critical load. The dynamics can be composed by lot of effects, which are the subject of the next section, but the brittleness of the material always supports crack propagation.

When the temperature goes beyond $T = 41\%T_M$ the material suddenly shows a high toughness. At certain temperatures propagation takes place with much difficulty because the crack tip emits a dislocation at any load beyond the critical one and stops. When the temperature becomes very high the crack prepared with the procedure of Section 6.1 on page 97 never propagates, for any value of the applied load, and under these circumstances it is even difficult to justify the existence of a critical load.

8.2 Dislocation emission and crack propagation in quasicrystals

8.2.1 Influence of dislocation emission on crack propagation

Dislocation emission generally plays an important role in crack propagation (cf. Chapter 3). In quasicrystals dislocation emission has a peculiar influence on crack propagation due to the very special quasicrystalline structure.

A dislocation moving in a periodic lattice leaves behind a perfectly reconstructed lattice, and therefore the lattice structure around the crack tip which has emitted a dislocation is intact. The crack and the tip interact only through their elastic fields, but the direction of crack propagation may be in general different from that of dislocation emission.

In a quasicrystal the situation is completely different. A dislocation gliding through a quasicrystal leaves behind a *phason wall*, which possesses a surface energy lower than that of any of the easy lines 3 and 4 defined in Section 5.2 on page 93 [77]. Thus the direction of propagation of a crack in a quasicrystal will be that of the phason wall of the dislocation emitted from the crack tip.

The only kind of a dislocation emitted from the tip of a crack propagating in the Tübingen triangle tiling during the simulation of crack propagation, is depicted in Fig. 8.1[1]. In Fig. 8.1(a) and Fig. 8.1(b) the tiling with no crack and no dislocation is represented. The atoms A, B, C and D of Fig. 8.1(b) lie on one of the easy lines for dislocation emission. In Fig. 8.1(c) the tip of a crack has emitted a dislocation. The slip plane of the dislocation is the easy plane for dislocation emission on which the atoms A, B, C and D lie, and the dislocation core is close to atom E. The atoms A, B, C and D during dislocation emission have moved to new positions. In Fig. 8.1(d) the movements of the quasicrystal atoms are represented which would locally reconstruct the original structure before dislocation emission. All the atoms A, B, C and D should be shifted by the same amount on the slip plane, meanwhile the atoms of the cluster close to the crack tip should be rotated as indicated in figure. Therefore the Burgers vector $\mathbf{b}$ of the emitted dislocation has only a component on the slip plane, and has a positive value.

[1] In all the figures the big atoms are depicted as small atoms and viceversa for sake of clarity.

The force due to the interaction of the dislocation with the crack in Mode I of Eq. 3.28 on page 59 is thus repulsive.

8.2.2 Numerical elastic estimates for dislocation emission in quasicrystals

In Section 3.3.5 on page 61 elastic estimates have been given under which a crack loaded at the critical load either emits a dislocation or propagates.

The value of the stress intensity factor K_{IE} by which spontaneous emission takes place involves the values of the Burgers vector b, of the dislocation core radius r_c, and of angle θ formed by the slip line with the cleavage direction (see Eq. 3.34 on page 62).

The value of the Burgers vector b for this kind of dislocation has been computed elsewhere [76], and reads:

$$b = \sqrt{2 - 4\cos(\frac{2\pi}{5})} \tag{8.1}$$

It might be not so easy to give a value to the dislocation radius r_c. In Fig. 8.2(a) a dislocation emitted from the tip of a crack is represented. The dislocation core is somewhere between the atoms A, B, C, and D, which form a rhombus in the tiling. The dislocation core might be better localized in one of the triangles which form the rhombus (see Fig. 8.2(b)), and to the dislocation radius r_c might be given the value of the radius of the circumference inscribed in the triangle. The dislocation radius can be easily calculated and has the value:

$$r_c = \frac{\sin(\frac{\pi}{5})\cos(\frac{\pi}{5})}{1 + \cos(\frac{\pi}{5})}. \tag{8.2}$$

Dislocations are emitted during propagation preferably on the easy lines for dislocation emission, which form an angle $\theta = \frac{\pi}{5}$ with the direction of crack cleavage.

In Table 8.1 the values of K_{IE} and of K_{IC} of Eq. 3.34 on page 62 are reported for different temperatures and on the lines on which the surface energy γ has been computed.

It is worth to remark that the values of K_{IE} and K_{IC} give only a criterion for the *statics* of the crack. For example, the value of the critical

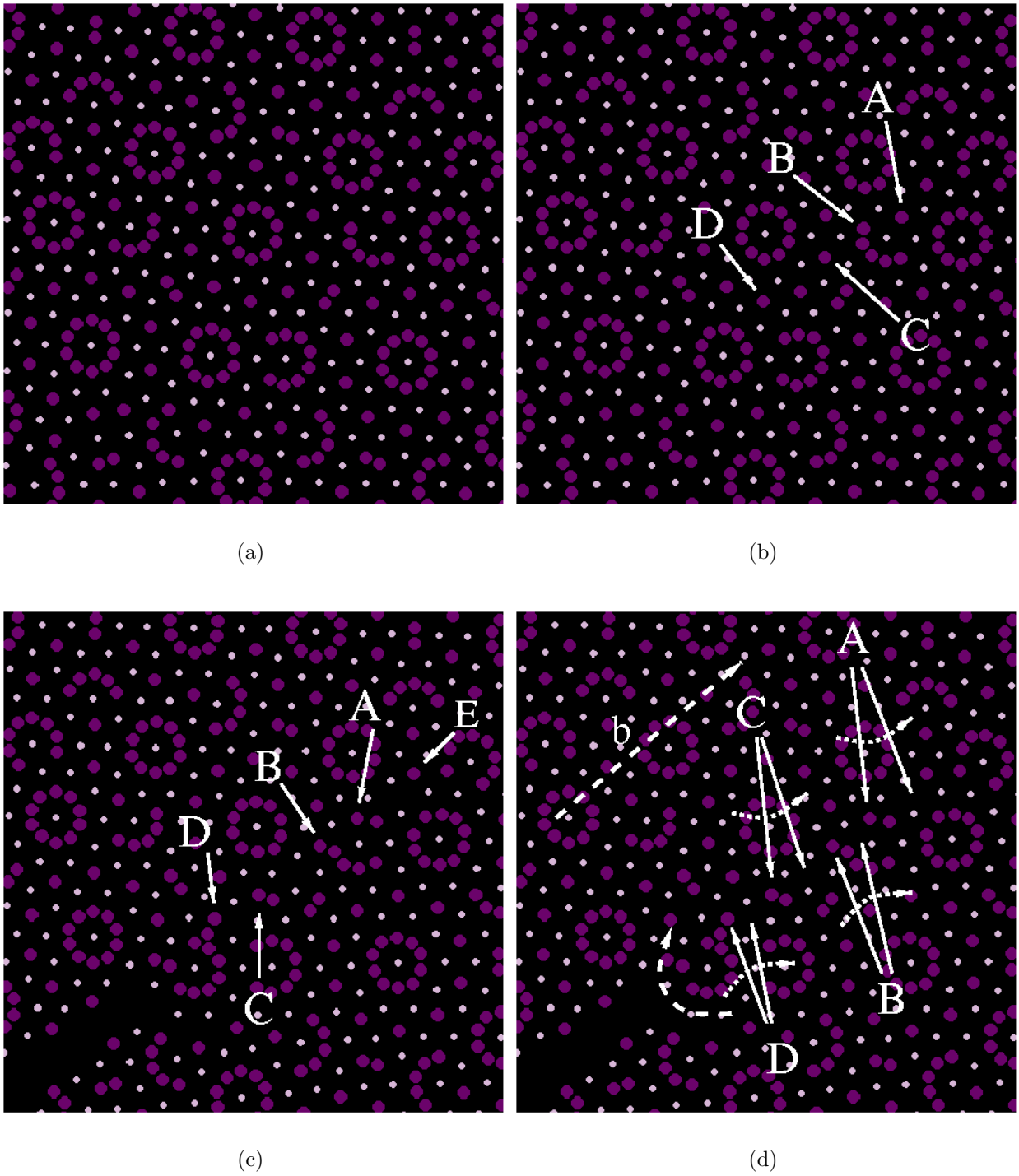

Figure 8.1: *(a) and (b) Tübingen triangle tiling with no crack and no dislocation. The atoms A, B, C and D lie on one of the easy lines for dislocation emission. (c) The tip of a crack has emitted a dislocation. The atoms A, B, C and D during dislocation emission have moved to new positions. The dislocation core is close to atom E. (d) Movements of the quasicrystal atoms which would locally reconstruct the original structure before dislocation emission.*

	K_{IE}	K_{IC}							
		line 1		line 2		line 3		line 4	
$15\%T_M$	7.0739	7.5155	❖	7.3875	❖	7.1701	❖	6.8472	≻
$31\%T_M$	7.5187	7.6445	❖	7.5188	❖	7.2988	≻	6.9552	≻
$47\%T_M$	7.8263	7.7259	≻	7.6000	≻	7.3830	≻	7.0455	≻
$63\%T_M$	7.7434	7.5887	≻	7.4734	≻	7.2320	≻	6.9035	≻
$78\%T_M$	6.6169	6.9174	❖	6.7982	❖	6.5836	≻	6.2900	≻
$94\%T_M$	5.5764	6.2255	❖	6.1796	❖	5.9332	❖	5.7134	❖

Table 8.1: *Values of K_{IE} and K_{IC} at different temperatures and on the lines on which the surface energy has been computed. The symbols ≻ and ❖ indicate respectively propagation and dislocation emission.*

stress intensity factor K_{IC} at the temperature $T = 15\%T_M$ on a line 4 is smaller the K_{IE} at the same temperature. Thus a quasicrystal cut on a line 4 strained just above the critical displacement would rather propagate than emit a dislocation. Conversely the same crack at the much higher temperature of $T = 94\%T_M$ would rather emit a dislocation than propagate. At temperatures T bigger than a transition temperature T_D, which can be roughly estimated to be:

$$T_D = 89.27\%T_M \tag{8.3}$$

the value of K_{IE} becomes smaller than K_{IC} on all the lines. In this ranges of temperatures and at any load bigger than the critical one the stress intensity factor is bigger than K_{IC}, because K increases linearly with the load (see Section 3.2.5 on page 53), and therefore no more propagation is possible and only dislocation emission can take place. The value of T_D could be a rough estimate of a brittle-ductile transition. In the simulations the value of the temperature at which no propagation is observed anymore is much smaller than T_D.

The values of K_{IE} and K_{IC} collected in Table 8.1 can be helpful to understand qualitatively crack propagation at low temperatures.

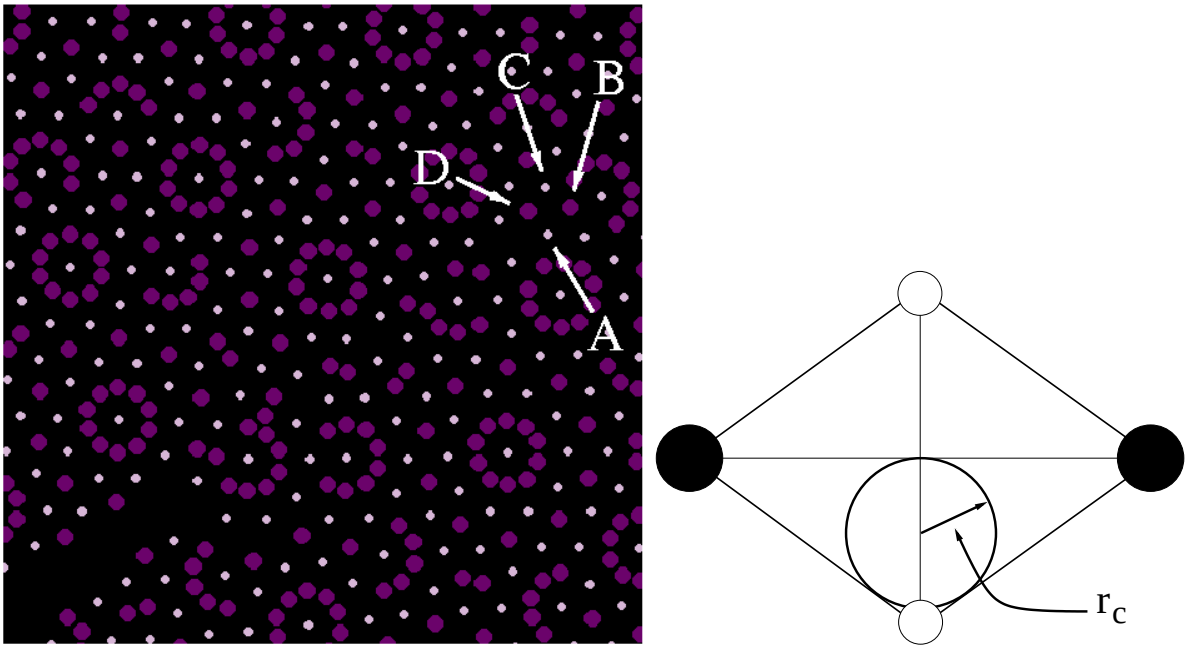

(a) (b)

Figure 8.2: *Dislocation emitted from the tip of a crack (a). The dislocation core is between the atoms A, B, C, and D, which form a rhombus. The dislocation core might be more precisely located in one of the triangles which form the rhombus (b).*

8.3 Low temperatures

8.3.1 Crack length and crack velocity

In this section we present the results of the simulations performed at $T < 31\%T_M$ for different loads $\Delta = e\Delta_c$ above the critical load Δ_c. For each value of the load the length of the crack and the crack velocity have been computed.

In Fig. 8.3, Fig. 8.4 and Fig. 8.5 the crack length in LJ units is depicted versus the time step of the simulation for different values of e and temperature. In Table 8.2 the crack velocities are collected and the relative errors

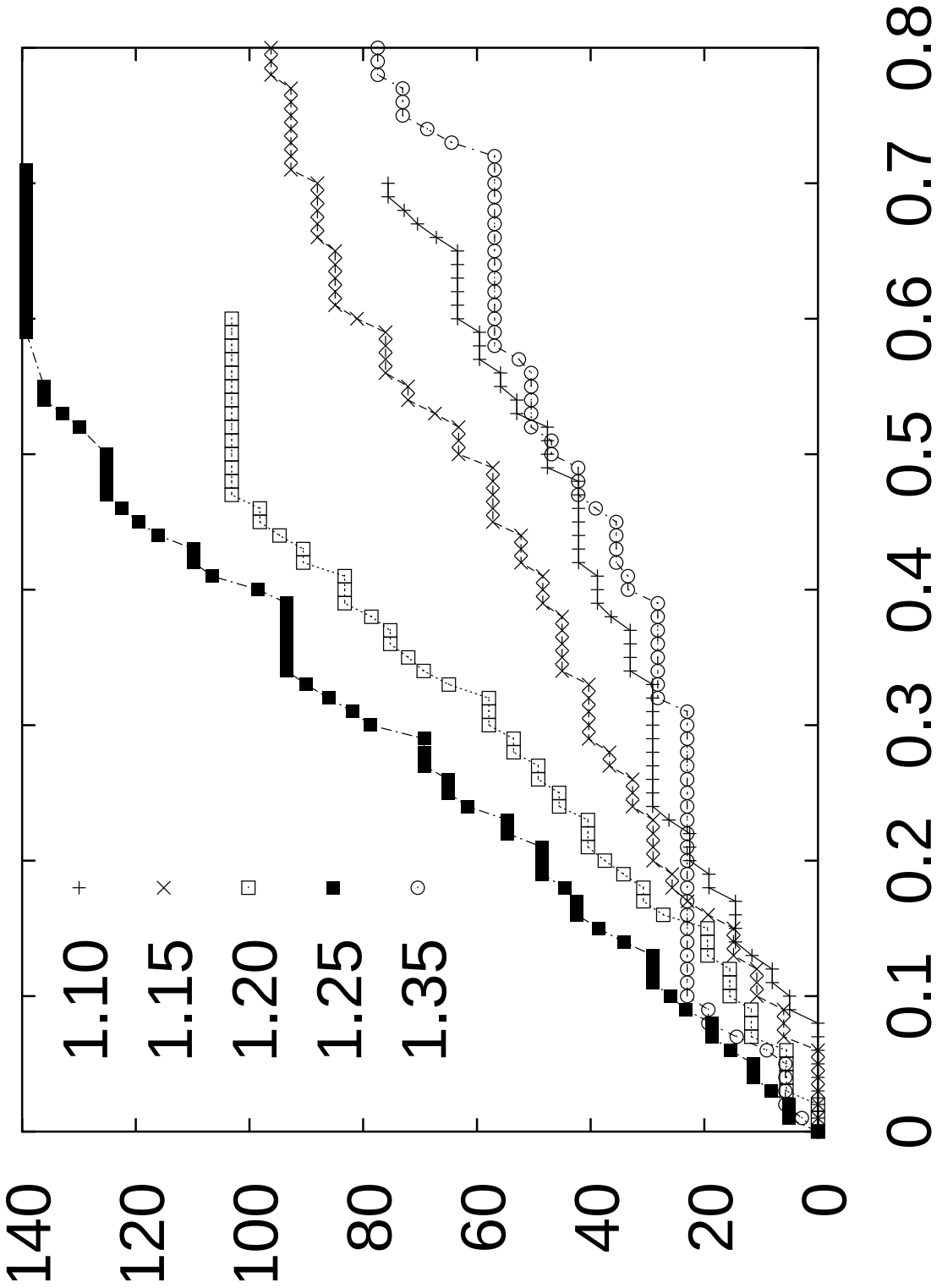

Figure 8.3: *Crack length in LJ units versus the simulation time for different values of* e *at* $T = 18\%T_M$.

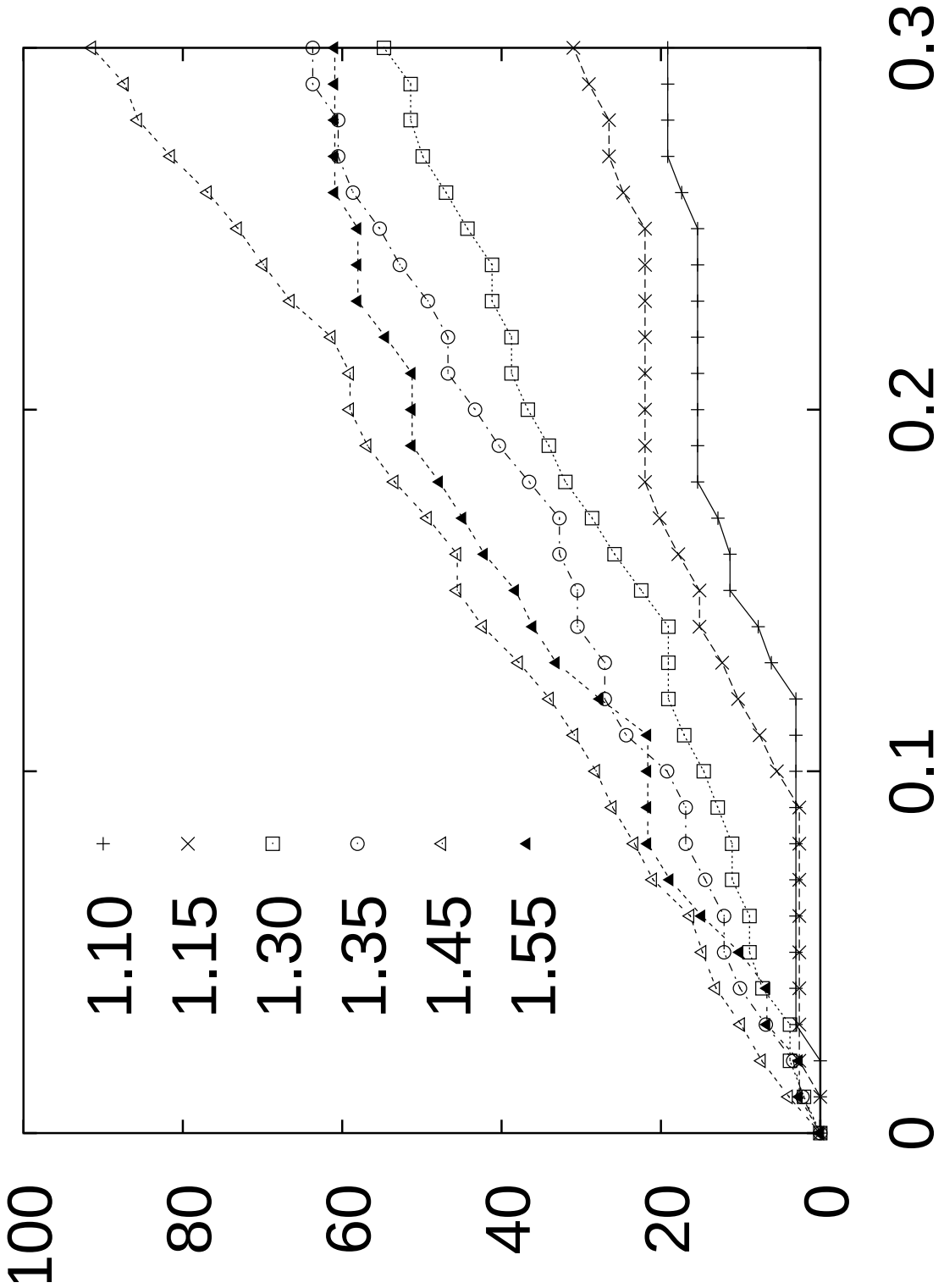

Figure 8.4: *Crack length in LJ units versus the simulation time for different values of e at* $T = 25\%T_M$.

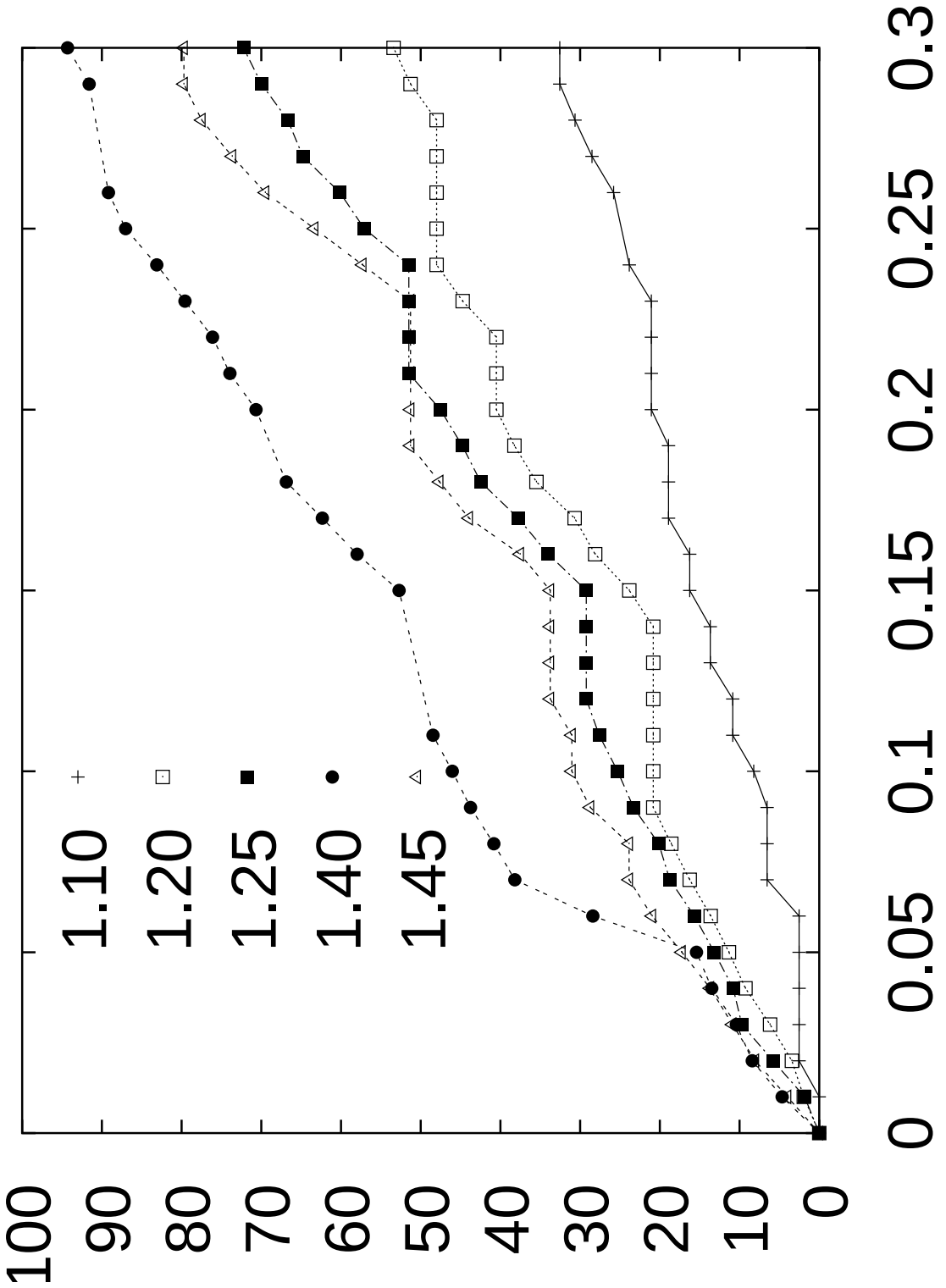

Figure 8.5: *Crack length in LJ units versus the simulation time for different values of e at $T = 31\%T_M$.*

computed by fitting the crack length l_C versus the time of the simulation using the linear function:

$$l_C = v_C\ t \tag{8.4}$$

where v_C is the crack velocity.

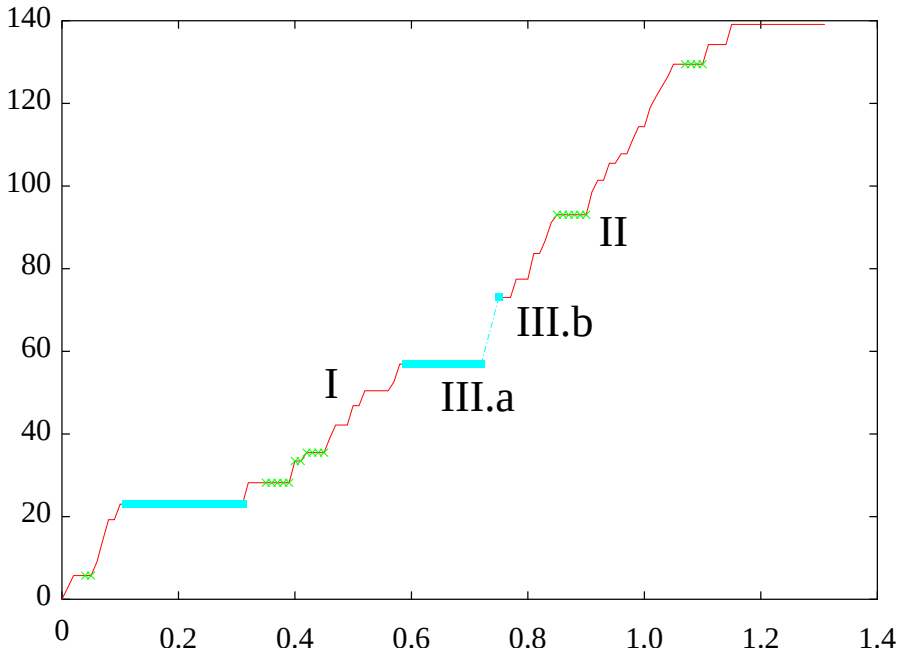

Figure 8.6: *Crack length in LJ units versus the simulation time in the low dislocation emission regime at a load* $\Delta_c = 1.15\Delta_C$. *The three modes of crack propagation. Mode I: the steady state. Mode II: The crack propagates emitting a dislocation which is immediately followed by the crack. Mode III: The crack emits a dislocation which covers a big distance and stops for a long time.*

8.3.2 Low and high dislocation emission regimes

Dislocation emission plays a crucial role in the dynamics of a crack, and may influence strongly the crack velocity. A close inspection to Fig. 8.3 and

$T = 18\%T_M$		
e	v_C	$\pm\Delta v_C$
1.10	103.354	1.12 (1.09%)
1.12	131.021	1.34 (1.02%)
1.20	162.521	1.11 (0.68%)
1.25	222.419	1.64 (0.73%)
1.30	256.979	1.81 (0.70%)
1.30	**108.447**	1.06 (0.98%)

$T = 25\%T_M$		
e	v_C	$\pm\Delta v_C$
1.10	63.99	1.13 (1.77%)
1.15	97.94	1.74 (2.07%)
1.20	151.21	2.50 (2.34%)
1.25	121.72	2.05 (1.85%)
1.30	146.43	2.85 (1.94%)
1.35	215.29	4.92 (1.82%)
1.40	244.80	4.46 (2.11%)
1.45	295.80	4.46 (2.11%)
1.50	**256.59**	5.00 (1.949%)
1.55	**235.53**	3.83 (1.627%)

$T = 31\%T_M$		
e	v_C	$\pm\Delta v_C$
1.10	110.116	1.54 (1.42%)
1.15	145.538	1.28 (0.81%)
1.20	181.035	1.68 (0.93%)
1.25	243.843	2.01 (0.85%)
1.30	242.093	2.26 (0.93%)
1.40	314.32	9.52 (3.03%)
1.45	**258.51**	2.37 (0.91%)

$T = 41\%T_M$		
e	v_C	$\pm\Delta v_C$
1.25	0.99101	0.011 (1.228%)
1.30	0.65697	0.019 (2.154%)
1.35	1.54972	0.016 (1.167%)
1.40	1.50780	0.016 (1.190%)
1.45	1.04407	0.022 (2.434%)
1.50	1.06873	0.024 (2.385%)

Table 8.2: *Crack velocities in LJ units/time of the s imulation. In boldface are the loads at which the the crack is in the high dislocation emission regime.*

Table 8.2 shows that the crack velocity and the crack length increase with an increasing load for values of Δ below $\Delta = 1.30\Delta_C$. In these load values range the dynamics of the crack behaves like one would expect by intuition. The common sense would find reasonable that the more a crack is loaded, the longer is the distance it can cover in the same time. And this is exactly what is measured in the simulations for values of the load below $\Delta = 1.30\Delta_C$. As soon as the load becomes too large, as for the value $e = 1.35$ in Fig. 8.3, the crack behavior becomes less intuitive because the crack velocity suddenly drops to a value which is much smaller than the expected one. This behavior is present in every crack propagation simulation at low temperature, and at high loads dislocation emission prevails over crack propagation. The number of dislocations which are emitted from the crack tip is such that they are able of taking away much more energy than a single dislocation could do, and they may damp crack propagation.

The number of emitted dislocations justifies the division of the crack dynamics into two regimes, a *low dislocation emission regime* (LDER), and a *high dislocation emission regime* (HDER). The peculiarities of dislocation emission and crack propagation at low and high loads are analyzed in detail in the next two sections.

Low dislocation emission regime

In the LDER the distance covered by the crack (see for example Fig. 8.3) is not a continuous function of time. At any load the crack starts to move, stops, waits for a certain time, moves and stops again. The movement of the crack is made of a sequence of stop and go steps. This *intermittent* regime of crack propagation has already been observed in simulations performed at zero temperature [77, 63], and is alway present in the LDER at all the low temperatures. The intermittent behavior of crack propagation is mainly due to dislocation emission. During propagation the crack may emit from its tip *only one* dislocation on one of the easy lines for dislocation emission and stops. If the distance of the dislocation core and the crack tip does not become too large, because for example the dislocation has hit an obstacle which cannot be bypassed, suddenly the crack may start to propagate again along the phason wall left by the dislocation. The process made of:

1. dislocation emission
2. stop

3. propagation along the phason wall

forms the intermittent regime. If the dislocation succeeds in reaching a big distance from the crack tip crack propagation stops definitively.

Crack propagation in the LDER can be subdivided essentially in three modes, depicted in figure as phase I, phase II, and phase III.

Phase I. Steady motion In phase I the crack propagates in a steady state without emitting any dislocation on one of the horizontal lines 4, and essentially does not change its direction of propagation. This is qualitatively in good agreement with the theory of elasticity, which predicts that the force on a crack in Mode I has only a component in the positive direction (see Eq. 3.25 on page 57). The distance covered by the crack tip is almost a linear function of time, and the only underlying mechanism of propagation is the classical snapping of bonds connecting neighboring atoms (see Fig. 8.7).

The crack during its motion on one line 4 may meet some inhomogeneities which may locally increase the toughness and thus make the crack deviate. When the crack has changed direction it enters the phase II or III.

Phase II. "Zero temperature" like dislocation emission In phase II the crack tip is suddenly on one of the lines 1 or 2 [2]. The crack propagates emitting a dislocation of the same kind of the dislocations observed in the simulations performed previously at zero temperature [77]. The emitted dislocation remains close to the crack tip (See Fig. 8.9) and within little time it is followed by the crack, which, aided by the dislocation emission, is able to change its direction of propagation to that of the easy line on which the emission takes place. The path covered by the emitted dislocation is very short, and therefore the crack stops only for a short time.

The mechanisms of dislocation emission might be qualitatively understood by elastic means.

When the crack has just changed direction of propagation the elastic field around the crack tip is not the one predicted by the linear theory of elasticity of Section 3.2 on page 46, the so called k-field, because the region close to the crack has not relaxed yet. The k-field is a solution of the linear theory of elasticity, and thus, at least at low loads, the k-field is a minimum of the

[2] It is not possible for the crack to reach a line 3 from a line 4 without passing through lines 1 and/or 2

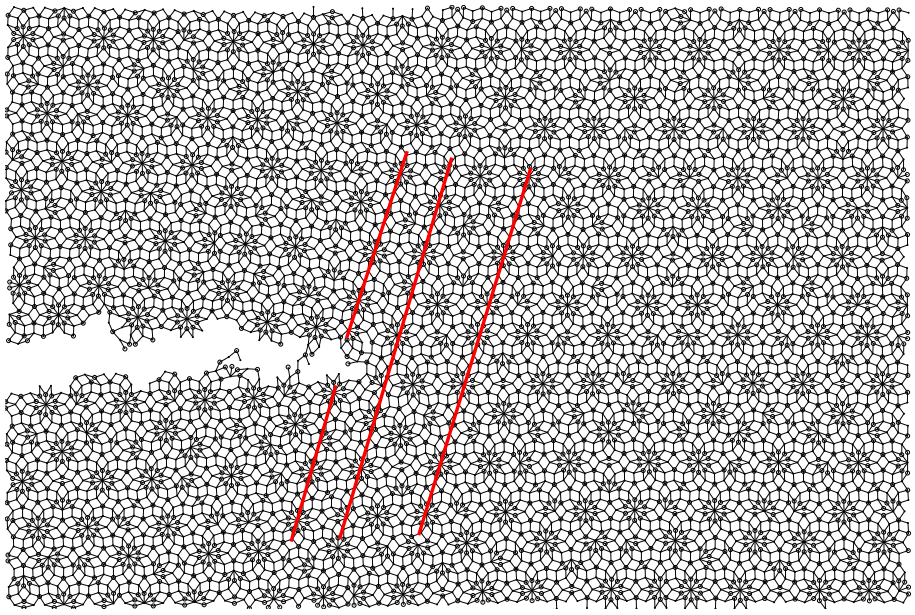

Figure 8.7: *Bond representation of a crack in a steady state of propagation. The lines connecting the centers of the rings lying on a line perpendicular to an easy line for dislocation emission are intact, and therefore no dislocation has been emitted from the crack tip. The crack propagates only by snapping atom bonds.*

free energy. For that reason the crack, also during its motion, tries to realize a pure k-field around its tip, and to relax to an equilibrium configuration of a crack alone. The stress intensity factor raises from zero to the value $K(\Delta)$, which is the value predicted by the theory of elasticity when the sample is strained at Δ above Δ_C. There is no theory which gives the quantitative dependence of K on Δ, and thus the exact value of the crack intensity factor is unknown. Only the critical values K_{IC} on the different lines are known from Table 8.1. The question whether $K(\Delta)$ is bigger or smaller than the corresponding equilibrium value K_{IC} can be easily answered. When Δ is equal to the critical displacement Δ_C of Table 7.7 on page 142 the stress intensity factor K_{IC} on the different lines assumes the values collected in Table 8.1 on page 149. When Δ is bigger than Δ_C the intensity factor K increases, because K depends linearly on the applied load (see Section 3.2.5 on page 53). In all our simulations crack propagation has been studied for

values of Δ bigger than $1.1\Delta_C^{line4}$, where Δ_C^{line4} is the critical displacement on the line 4 [3]. In Fig. 8.8 is represented $1.1\Delta_C^{line4}/\Delta_C^{line1}$, where Δ_C^{line1} is the critical displacement on line 1, computed using the linear dependence of Δ_C on T of Eq. 7.60 on page 141. At any temperature already the smallest value of $\Delta = 1.1\Delta_C^{line4}$ at which crack propagation has been studied is bigger than the critical displacement on the line 1, which is the biggest among all the critical displacements (see Fig. 8.8). The stress intensity factor K of the crack will always be bigger than K_{IE}, and thus when the crack changes direction of propagation crossing one of the lines 2, 3 or 4, it emits a dislocation.

In phase II after emission the dislocation does not cover a long distance from the crack tip and it is immediately stopped by an obstacle (see Fig. 8.9). The stress intensity factor K of the crack in the quasicrystal is certainly changed by dislocation emission. The theory of elasticity predicts that when a dislocation reaches a big distance from the crack tip the reciprocal influence of the crack and of the dislocation goes to zero. Quantitatively this means that the crack stress intensity factor K, which would be shielded by the presence of a dislocation with positive Burgers vector (see Eq. 3.19 on page 52), raises again to the value of the crack with no dislocation. Thus, when the dislocation is far away enough from the crack tip, either crack propagation begins again, or a new dislocation is emitted. In a quasicrystal the situation is different because the dislocation leaves behind a phason wall. The phason wall changes the quasicrystal structure in the vicinity of the crack tip and consequently also the stress distribution around the crack. The stress intensity factor K of a crack which has emitted a dislocation in a quasicrystal might not be that of Eq. 3.19 on page 52, and the deviation of K from the theoretical value might depend on the crack-dislocation distance. From the simulations it is doubtless clear that when the dislocation remains close to the crack tip K reaches at least the value necessary to propagate along the phason wall.

Phase III. Long dislocation path and stop time In phase III the crack emits a dislocation which covers a relatively long distance from the crack tip, and it is stopped on its motion by an obstacle lying on the easy line of emission far away from the crack tip (Fig. 8.10(a)). The crack stops for a long time (see phase III.a in Fig. 8.7), and suddenly starts to propagate again (phase III.b and Fig. 8.10(b)). These dislocations, which cover a long

[3] At smaller values of Δ lattice trapping has inhibited crack propagation.

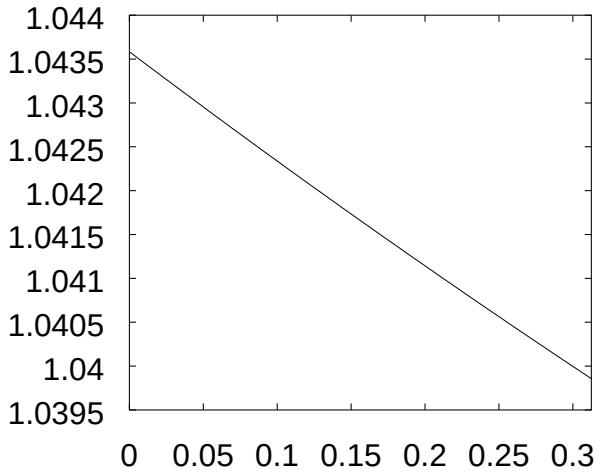

Figure 8.8: *Value of* $1.1\Delta_C^{line4}/\Delta_C^{line1}$ *versus* T/T_M *for* $T < 31\%T_M$.

distance and nevertheless aid crack propagation, are a new feature of crack propagation in the presence of temperature. In the simulations performed at zero temperature only dislocations of the kind observed in phase I are present, and if a dislocation was able to reach a long distance then crack propagation was definitively stopped.

The dislocation emission in phase III takes place for the same reasons like in phase II, with the difference that in phase III the obstacle stopping the dislocation lies away from the crack tip. The long stop time cannot be easily explained, and only a guess can be hazarded. The intermittency behavior might be a feature characteristic of a quasicrystal. The simulations show that when the dislocation covers a big distance from the tip the stress intensity factor drops to a value smaller than the one needed to propagate along the phason wall, and crack propagation stops definitively. On the contrary when the distance crack-dislocation remains bounded the crack stops for a long time and then propagates again. It might be that some time is needed for the system in order to settle down to a relaxed configuration, where K reaches again a big enough value so that the crack may propagate further. This time needed by the system to relax might be the origin of the intermittent behavior.

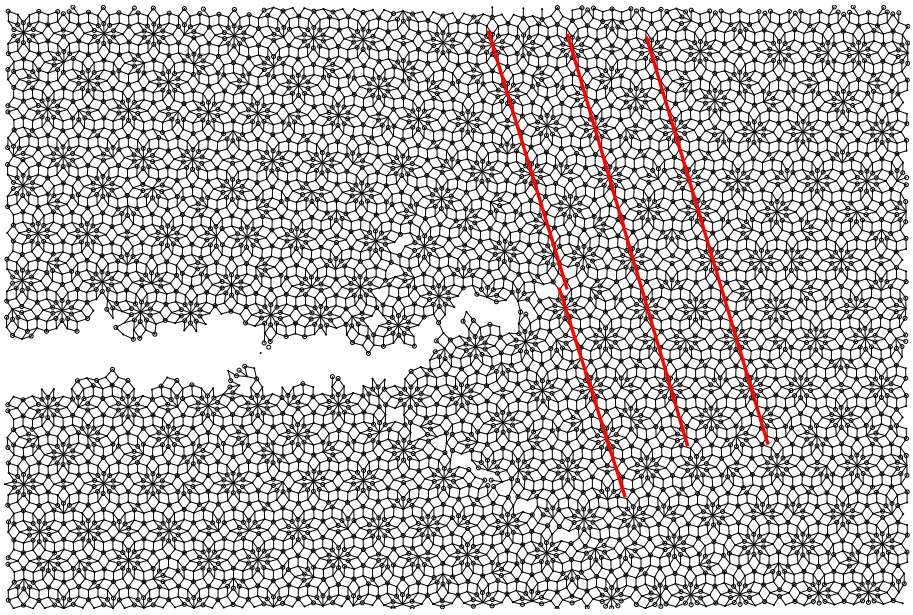

Figure 8.9: *Bond representation of a crack emitting a "zero like" dislocation. One of the lines connecting the centers of the rings lying on a line perpendicular to a easy line for dislocation emission immediately close to the crack tip is broken. The crack tip emits and immediately follows a dislocation on one of the easy lines for dislocation emission. The dislocation is immediately stopped by an obstacle.*

High dislocation emission regime

The characteristics of crack propagation in the high dislocation emission regime cannot be so easily and clearly classified. This regime is highly unstable, and the analysis of the crack dynamics is complicated by the overlapping of many effects which take place simultaneously. When the load reaches high values many dislocations may be emitted from the crack tip because the stress intensity factor becomes more and more bigger than K_{IE}. After dislocation emission the crack propagates further because K remains bigger than the minimal values necessary for propagation. The main feature of crack propagation at high loads is the presence in the sample of many dislocations which are emitted from:

- the crack tip, but never in number bigger than three

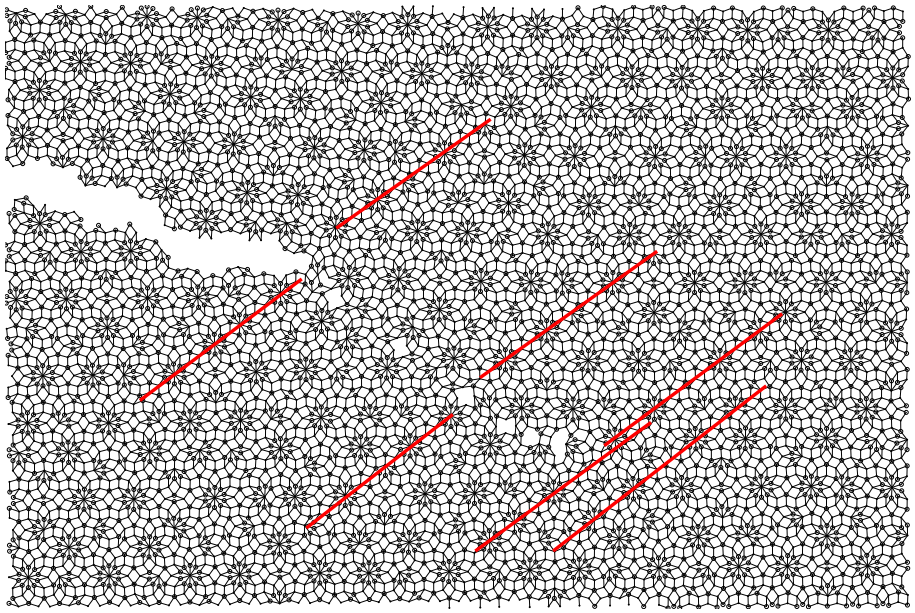

(a)

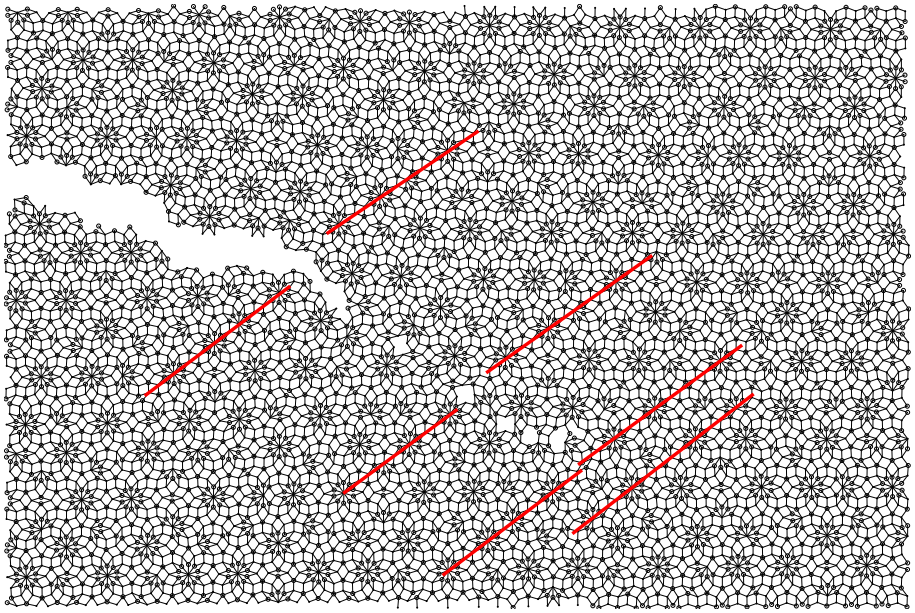

(b)

Figure 8.10: *Bond representation of a crack in phase III of propagation. In (a) a dislocation has been emitted from the crack tip, and it covers a relatively long distance before stopping. In (b) the crack follows the dislocation along the phason wall.*

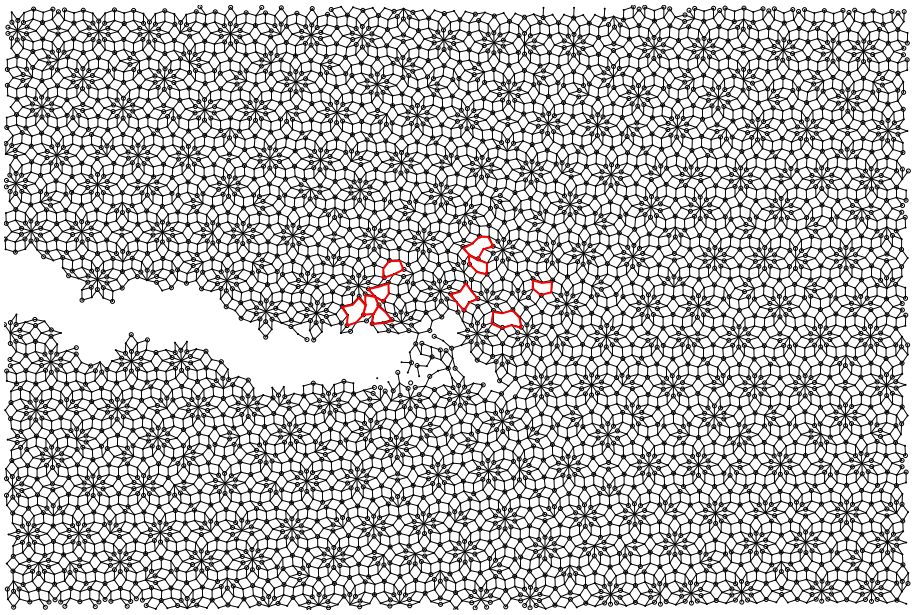

Figure 8.11: *Bond representation of a crack loaded at very high loads which emits many dislocations (regions marked in figure). Two dislocations have been emitted from the crack tip, and three from the crack surface.*

- the crack free surface
- the edges of the rectangle.

At not too high loads the emission of numerous dislocations is still initiated only from the crack tip and from the crack free surface (see Fig. 8.11). The dislocations emitted from the crack tip take lot of energy away from the tip and account for an immediate slowing down of the crack velocity (see Fig. 8.3 for $e = 1.35$). At these loads the only dislocations responsible for a crack dynamics dumping are those emitted from the crack, and therefore it is still possible to define and measure a crack velocity.

At higher values of the load dislocations may be emitted from the edges of the rectangle, and these dislocations are able to travel inside the material. From the core of a dislocation which has stopped, often a new crack is initiated (see Fig. 8.12). The formation of a new crack releases a lot of energy and generally inhibits further crack propagation.

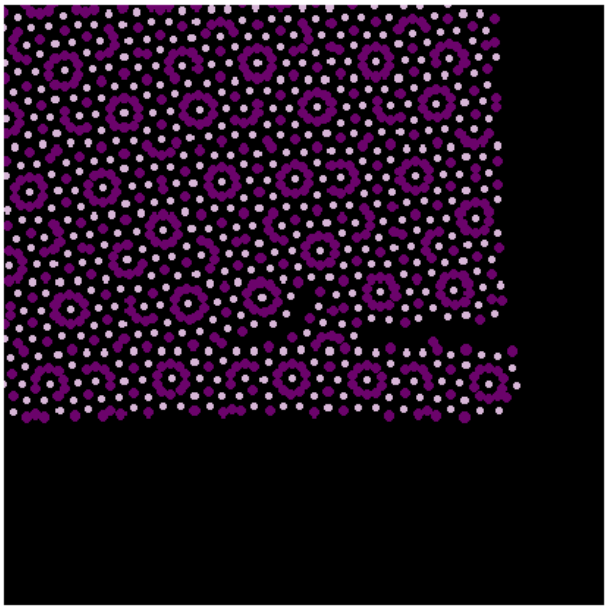

Figure 8.12: *A dislocation emitted from the edges of the rectangle has stopped and nucleated a new crack from its core.*

It is very hard to characterize quantitatively the dynamics of a crack in this regime. The many dislocations in the sample and the eventual formation of new cracks strongly influence the crack velocity, which is not anymore characteristic of a plain crack dynamics, but is the result of the influence of those independent side effects. The only crack propagation we can try to analyze is in the low dislocation emission regime, where bonds are broken and few dislocations are emitted under very well reproducible conditions, but at so high loads it becomes very difficult to distinguish whether a crack has stopped because a dislocation has been emitted from its tip, or conversely because a new crack has formed somewhere in the sample. Under these working conditions it becomes very hard to define where the "crack tip" is, and thus it is practically impossible to define a crack velocity.

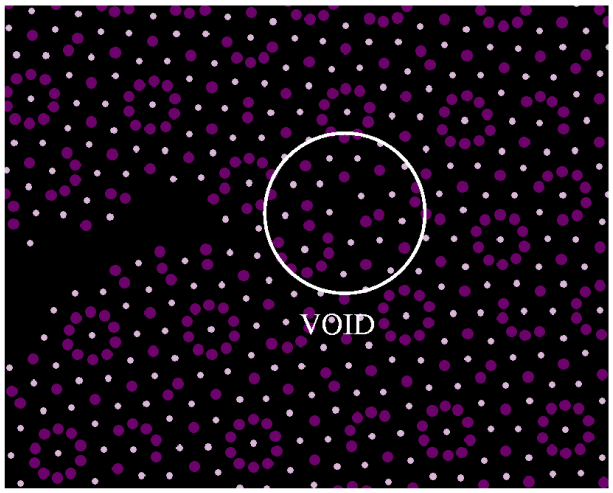

Figure 8.13: *At $T = 41\%T_M$ and at low loads a defect is formed in front of the crack tip. The void relaxes the elastic energy around the tip and inhibits crack propagation.*

8.4 Intermediate temperatures

The simulations performed at the intermediate temperature of $41\%T_M$ have shown a very peculiar behavior of crack propagation, and it is worth to analyze them in detail.

8.4.1 Low loads

For values of $\Delta = 1.05, 1.10, 1.15, 1.20\%\Delta_C$ no crack propagation takes place. The lack of propagation is very clearly not due to lattice trapping effects. As soon as the crack is displaced above Δ_C in front of the crack tip a void is formed (see Fig. 8.13). The void does *not* come from the core of a dislocation, but it is on the contrary a well defined defect which relaxes the elastic energy around the tip and inhibits propagation.

8.4.2 High loads

At higher loads the crack starts to propagate. In Fig. 8.16 is depicted the crack length for values of Δ above $1.25\%\Delta_C$. The crack velocities are

collected in Table 8.2.

At this intermediate temperature the crack velocity is around one hundredth of the velocity at low temperatures. There is no relation anymore between crack velocity and applied load. When the load increases the crack does not move necessarily faster. The crack length is still made of a collection of stop and go movements. But there are important differences to the propagation at lower temperatures:

1. The crack may stop for a long time, and the stop is *rarely* due to dislocation emission.

   The *intermittent* behavior at this temperature, which has been observed at every load, finds its origin in a completely new effect. In contrast to the low temperature intermittency, no dislocation is emitted from the tip. In front of the crack the same kind of void observed at low loads is formed (Fig. 8.14), and the crack does not move for a long time. The behavior of the crack seems to be completely analog to what happens at low loads, but with the difference that the crack in this load regime has only temporarily stopped.

2. No dislocation is emitted anymore to make the crack change its direction of propagation.

   In contrast to the low temperature case the crack is able of changing its direction of propagation without emitting a dislocation. In Fig. 8.15(a) and Fig. 8.15(b) the crack propagates beside one of the clusters. The new crack surface is not formed by following a dislocation along the phason wall left by dislocation behind, but by the coming unstuck of the atoms around the cluster.

3. If a dislocation is emitted it is followed. In contrast to the low temperature case the entire phason wall and the dislocation core are separating by the formation of voids.

   When a dislocation is emitted the crack still follows it. In contrast to the low temperatures, where the propagation was due to a consecutive snapping of bonds from the crack tip to the dislocation core, at this temperature the crack is made propagate further by voids which are formed on the phason wall and in the dislocation core (Fig. 8.15(c) and (d)).

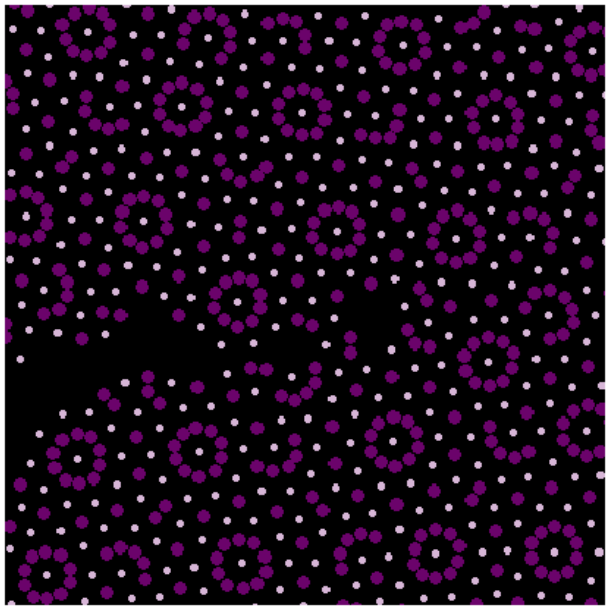

Figure 8.14: *At $T = 41\%T_M$ the crack emits a void in front of the tip and stops for a long time.*

4. During propagation often in front of the tip a void is formed, which becomes the new crack surface. The old crack may occasionally stop, and a bridge is formed between the crack surfaces.

   The formation of voids in front of the tip seems to be one of the most important propagation workings at this temperature (Fig. 8.17(a) and (b)). Occasionally at low loads a dislocation may still be emitted, which covers a very short distance and is immediately followed by the crack, like the low loads and low temperature case. But this mechanism disappears as soon as the load is increased to make place to the formation of voids. The extension of the voids depends on the load. The bigger the load the more extended are the defects.

5. The crack may stop by emitting a dislocation or forming a void.

8.4.3 Some remarks

Theory of elasticity predicts that at the intermediate temperature around $41\%T_M$ almost no dislocation emission should take place, and only propagation is favored (see Table 8.1 on page 149). The simulations show that at this temperature the formation of voids seems to be more favored than crack propagation. The theory of elasticity fails in predicting the formation of such defects because a void is not anymore a topological defect to which it is possible to associate an elastic field. At this temperature we are far beyond the limit of applicability of the continuum model.

8.5 High temperatures

The simulations performed at temperatures T higher than $52\%T_M$ have shown practically always the same behavior. In this regime of temperature almost no crack propagation takes place. At high temperatures the quasicrystal shows even no critical load at all.

8.5.1 $T = 52\%T_M$

The system at this temperature still possesses a critical load. There exists a value of the load Δ_c defined in Section 6.1 on page 97 where the crack does not propagate, the system is in a minimum of the free energy, and *no dislocation is emitted from the crack tip.* The behavior of crack propagation is analyzed at different loads.

$\Delta_C < \Delta < 1.25\Delta_c$ When the crack is strained beyond the critical load and under $\Delta = 1.25\Delta_C$, the crack tip emits immediately *one dislocation and stops* (see Fig. 8.18).

$1.25\Delta_C < \Delta < 1.30\Delta_c$ At the value $\Delta = 1.30\Delta_C$ the crack propagates for a very short distance, emits *two* dislocations, and stops. From the core of one dislocation a new crack surface is initiated. The new crack covers a very short distance and stops again (Fig. 8.20).

$\Delta > 1.30\Delta_c$ For values of Δ bigger than $1.30\Delta_C$ the quasicrystal shows a glass like behavior for crack propagation. In front of the crack tip a new

crack is nucleated and, contrary to propagation in glasses, the crack does not advance anymore (see Fig. 8.19). At high loads it has been observed the formation of new crack surfaces from the core of dislocations emitted from the rectangle edges.

Some remarks

Even at this temperature the elastic theory predicts a plain crack propagation regime with no dislocation emission at all (see Table 8.1 on page 149). On the contrary the system shows something similar to a ductile behavior, at least at loads $\Delta < 1.40\Delta_C$.

8.5.2 $T = 87\%T_M$

At the very high temperature of $T = 87\%T_M$ no crack propagation takes place, and there does not exist even a critical load anymore. The configuration of step 3 in Section 6.1 on page 97 never propagates at any value of the displacement Δ_c. No dislocations are emitted, neither from the crack tip nor from the rectangle edges. The crack simply relaxes its exceeding energy by forming voids in front of its tip. Under these circumstances it is very difficult to justify the existence of a critical load. The system is much mollified, but does not exhibit a ductile behavior. There is no dislocation emission at all, and dislocation emission is the primary way for a ductile crack to dissipate its energy and stop. It seems that the temperature is so high that the system has enough energy to rearrange the atoms close to the crack tip in a minimum of the free energy instead of emitting a dislocation.

8.6 Comparison with experimental results

Mainly two results of the numerical simulations of crack propagation collected in this chapter are qualitatively in accord with the experiments reported in Section 3.5 on page 67.

Firstly the relation between crack propagation and dislocation emission. Crack propagation on surfaces of an icosahedral $Al_{70}Pd_{23}Mn_7$ single quasicrystal takes place along directions parallel to planes of crystallographic symmetry. The propagation pattern of a crack moving on a surface of fivefold symmetry shows strong meandering with angles of $n \times 36^o$ between the parts

of the crack. Wollgarten et al. [70] in straining experiments performed in the same quasicrystal have found that the planes of crystallographic symmetry correspond also to planes of dislocation motion. Thus in this quasicrystal the planes of crack propagation are the planes on which dislocations glide. This experimental evidence is qualitatively confirmed by our simulations. Our results show at any temperature that the propagation pattern of a crack moving in a two-dimensional quasicrystal is piecewise, and most of the pieces of the crack pattern are on the easy planes for dislocation emission. Unfortunately the dislocation free path predicted by the computer simulations is less than or equal to a nanometer [77], and thus the authors of [23] cannot observe a direct relation between dislocation emission and change of crack propagation direction. This effect could be a characteristic of fracture propagation in quasicrystals predicted by the simulations but not measurable in real experiments.

At intermediate temperatures (cf. Section 8.4 on page 165) the formation of voids seems to be the underlying mechanism for crack propagation. When the applied load is high on a phason wall of an emitted dislocation lot of voids are forming contemporary (Fig. 8.15(c) and (d)), which are responsible for further crack propagation. In the experiments a similar behavior has been observed. When applying high indentation forces on the quasicrystal surface hundreds of craters nucleate along a crack path and partially grow together, finally causing the sample to break into pieces [23].

The next chapter contains the conclusions of this work. It summarizes the main results obtained so far, and outlines the topics of future developments of this work.

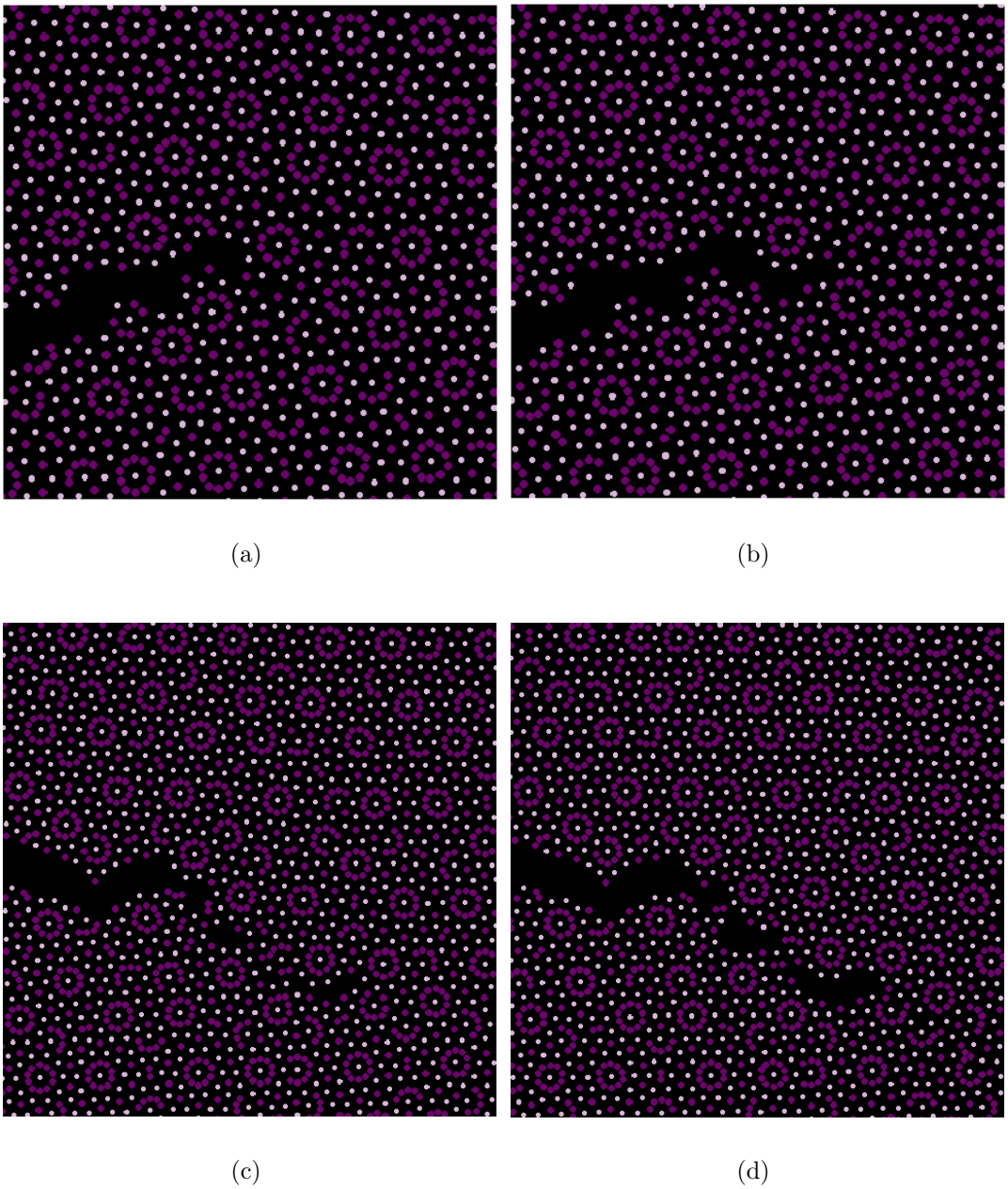

(a) (b)

(c) (d)

Figure 8.15: *At $T = 41\%T_M$ the crack changes its direction of propagation without emitting a dislocation (a) and (b). The crack has emitted a dislocation. On the phason wall and in the dislocation core voids are formed which make the crack propagate further (c) and (d).*

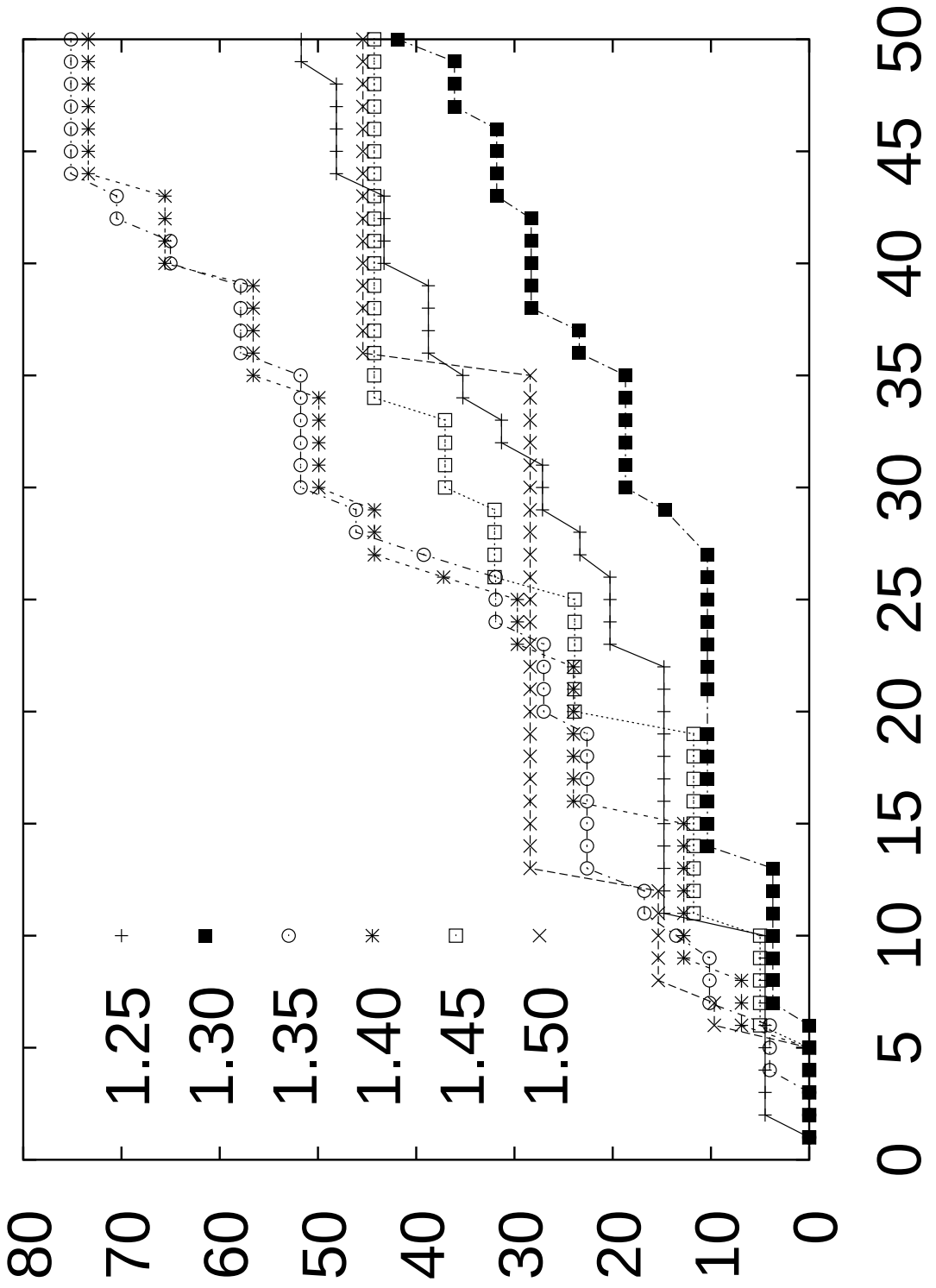

Figure 8.16: *Crack length in LJ units versus the simulation time for different values of e at* $T = 41\%T_M$.

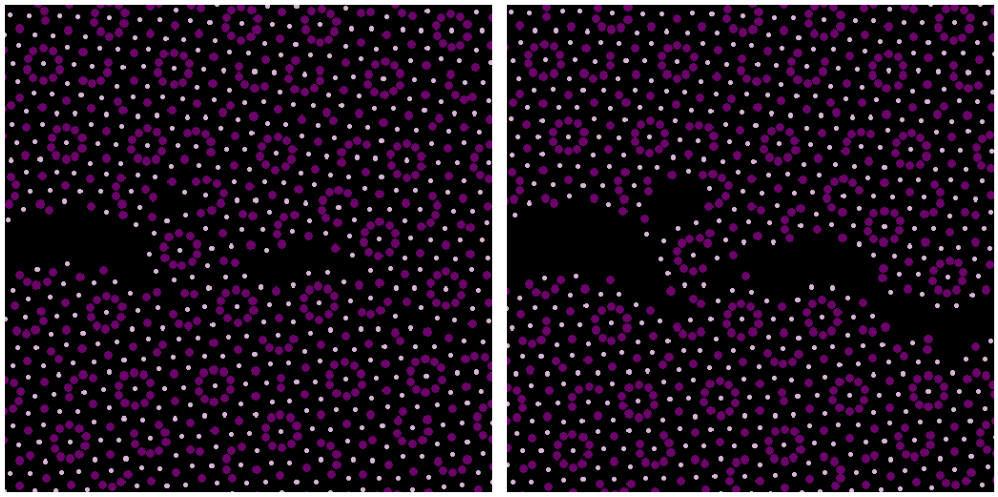

(a) (b)

Figure 8.17: *At $T = 41\%T_M$ the crack propagates by forming voids in front of the tip. A bridge is left behind the crack.*

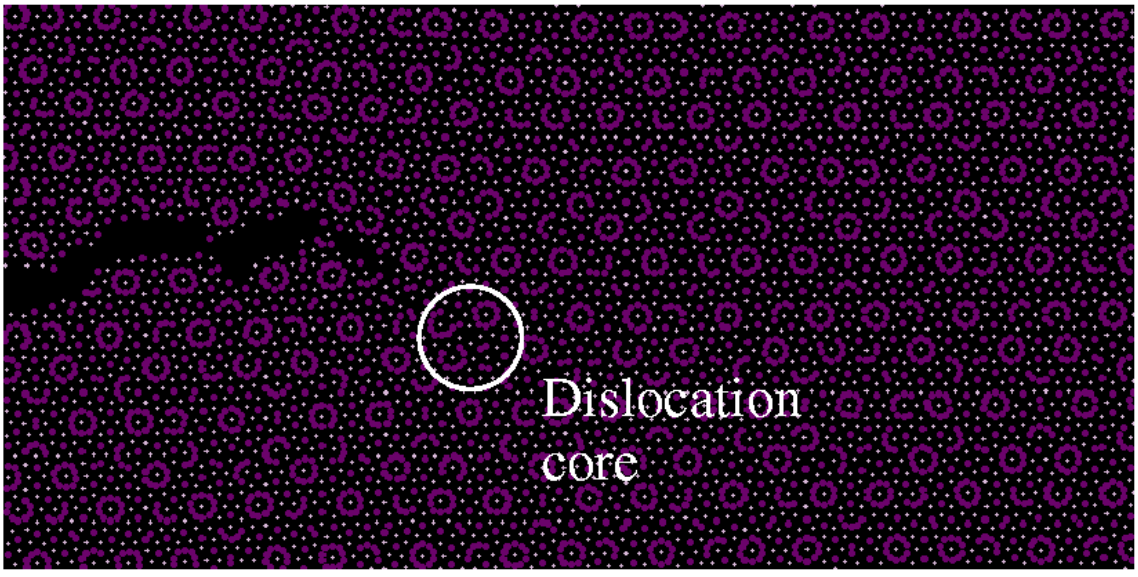

Figure 8.18: *A dislocation is emitted from the crack tip at $T = 52\%T_M$ and remains close to the tip for values of the load $\Delta_C < \Delta < 1.25\Delta_c$.*

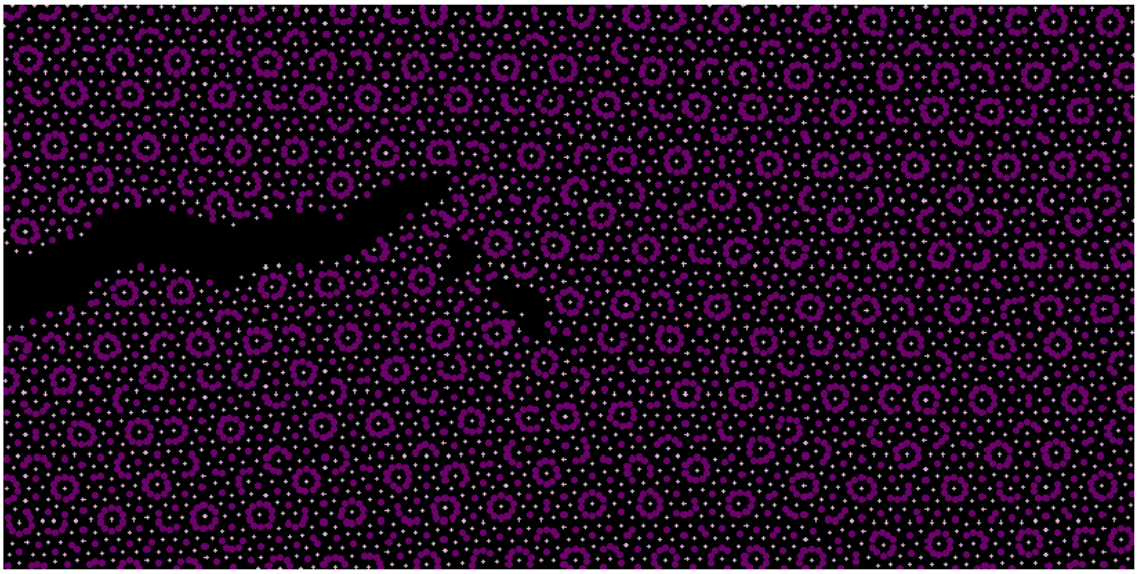

Figure 8.19: *A new crack surface is formed in front of the crack tip at* $T = 52\%T_M$ *and* $\Delta > 1.40\Delta_c$.

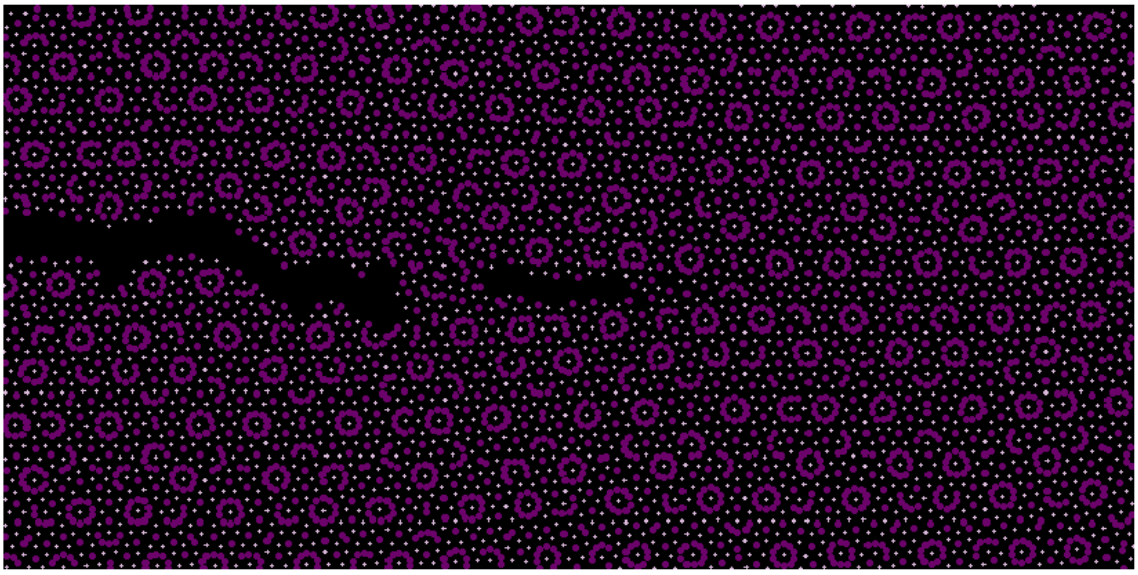

Figure 8.20: *A new crack surface is formed from the core of a dislocation emitted from the tip of a crack at* $T = 52\%T_M$ *and* $\Delta = 1.30\Delta_C$.

Chapter 9

Conclusions

The numerical results of this work deal with the computation of the **equilibrium** properties and with the **crack propagation** in the Tübingen triangle tiling.

Equilibrium properties

In this work much effort has been devoted to the calculation of the equilibrium properties in the Tübingen triangle tiling, which have shown to be important for the qualitative understanding of crack propagation in the presence of temperature.

Temperature dependence of the Nosé-Hoover ν The temperature dependence of the Nosé-Hoover thermostat mass ν has been measured. The Nosé-Hoover dynamics has shown to successfully reproduce the canonical statistics with the computed values of ν (Section 7.1 on page 105).

Free energy difference calculation Two different methods for computing free energy differences have been applied for the first time to the calculation of static properties of cracks. The two methods have been compared, and the free energy calculations based on the phase space compressibility of the Nosé-Hoover dynamics have been proved to be numerically equivalent to the classical umbrella sampling.

The umbrella sampling is much faster than the phase compressibility method, and it has to be preferred in constant temperature calculations

(Section 7.2 on page 110), whereas the second may be still competitively used in entropy differences calculations at non constant temperature.

Surface energies, elastic constants, and critical displacements The umbrella sampling has been used to calculate the surface energies, the elastic constants, and the critical displacements of a quasicrystal at various temperatures (Section 7.3 on page 133), which have allowed to calculate the stress intensity factor of a crack both for a pure Griffith propagation, and for a spontaneous dislocation emission (Section 8.2.2 on page 147).

Crack propagation

Modeling crack propagation in the presence of temperature An original model of crack propagation in the presence of temperature has been proposed. The sample in which propagation takes place is ideally divided by an ellipse into two zones. The atoms inside the ellipse, which contains the crack tip as well, move accordingly to the Hamilton dynamics to allow for a temperature gradient, while the atoms outside are kept at constant temperature by means of a Nosé-Hoover dynamics.

Crack propagation has been studied in a big sample and in a range of temperatures below the melting temperature T_M of the system.

Low temperatures

At low temperatures ($T < 41\%T_M$) crack propagation takes place with ease. In this temperatures range the number of dislocations emitted during propagation justifies the division of the crack dynamics into two regimes, a *low dislocation emission regime* (LDER), and a *high dislocation emission regime* (HDER).

Low dislocation emission regime In the LDER crack propagation takes place by means either of a pure snapping of bonds or of the emission of *one dislocation*. When a dislocation is emitted crack propagation shows an intermittent behavior, which has been observed also in the simulations performed at zero temperature. In this regime of propagation an explanation of the dislocation emission based on elastic estimates has been proposed (Section 8.3.2 on page 156).

High dislocation emission regime In the HDER the characteristics of crack propagation cannot be easily and clearly classified. This regime is highly unstable, and the analysis of the crack dynamics is complicated by the overlapping of many effects which take place simultaneously (Section 8.3.2 on page 161).

Intermediate temperatures

Crack propagation at the intermediate temperature of $41\%T_M$ has shown a very peculiar behavior (Section 8.4 on page 165).

Low loads At low loads no crack propagation takes place, because in front of the crack tip a *void* is forming, which does not come from the core of a dislocation.

Higher loads At higher loads the crack starts to propagate very slowly, compared to the typical velocities at lower temperatures. Still an intermittent regime is present, but the role of the dislocation is taken by the void. The crack is able of changing its direction of propagation without emitting a dislocation.

At this temperature the material seems to be much mollified but still brittle, because there is a range of loads at which the crack propagates, and the formation of voids seems to be a new underlying mechanism of propagation.

High temperatures

At high temperatures crack propagation does not take place anymore.

$T = 52\%T_M$ The system at the temperature $T = 52\%T_M$ has shown a typical *ductile* behavior. At low loads beyond the critical one, the crack emits immediately a dislocation and stops. When the load increases the crack still opposes to the propagation by emitting two dislocation or forming a new crack surface from a dislocation core. At high loads it has been observed the formation of new crack surfaces from the core of dislocations emitted from the rectangle edges, and in front of the crack tip a new crack is nucleated. At this temperature the material might have become ductile, because at *low*

loads dislocation emission prevails over propagation. Crack propagation at high loads does not contradicts the ductile evidence at low loads. There is obviously always a load regime beyond which even a ductile material breaks down, because no material can bear a too huge strain.

$T = 87\%T_M$ At the very high temperature of $T = 87\%T_M$ there does not exist a critical load anymore. Even at high loads no crack propagation takes place, and the material seems to be very much mollified.

Future developments

The numerical results of this work have opened many directions in which the investigation of crack propagation in quasicrystals might be intensified.

Dislocation emission in the LDER

At low temperatures and in the LDER the dislocation emission has been explained by means of elastic estimates. Two points should be further investigated.

Dependence of the surface energy on the length of the cut On the lines 3 and 4, the dependence of surface energy on the length of the cut should be computed. This could explain whether the partially broken clusters which are placed on these lines are responsible for a local increase of surface energy with a consequent change of crack propagation.

Estimation of the dislocation radius r_c The second important point is a precise estimation of the dislocation radius r_c. The stress intensity factor K_{IE} at which dislocation emission takes place is very sensible to the dimensions of r_c, and a precise measure of r_c is the necessary condition under which the elastic estimates of Section 8.2.2 on page 147 might doubtless explain the dislocation emission phenomena.

The simulations of crack propagation at low temperatures and in the LDER have doubtless shown that crack propagation after dislocation emission takes place on a direction (the phason wall) which is forbidden by the linear theory of elasticity.

This effect could have essentially two origins.

Fluctuations on the phason wall A less likely possibility is that some fluctuations casually induce the break of some bonds on the phason wall, allowing for a further crack propagation.

Stress intensity factor for quasicrystals Another possibility is that the phason wall of a dislocation in a quasicrystal *changes* the stress intensity factor of a crack in a way which could not be predicted by the usual elasticity theory. A theory of elasticity suited for quasicrystals could take into account the presence of the phason wall, and could give a new expression of the stress intensity factor of a crack. The force on a crack might have a component along the phason wall, and this could explain why the crack follows the dislocation.

Void formation The voids, observed in the simulations performed at $T = 41\%T_M$, are completely new defects which support crack propagation. Their formation could be taken into account by a continuum model, if they were modeled as holes. Till now a continuum theory has been developed for a crack with a dislocation distribution, but none has given the expression of the stress intensity factors of a crack which coexists with holes. Such an analytical work could help in having an insight in these new effects observed in the simulations. It might be that at this temperature the elastic energy, i.e. the free energy, of a crack with holes is less than that of a crack with dislocations, and thus void formation could be preferred to dislocation emission.

Ductile transition The apparent ductile behavior observed at $T = 52\%T_M$ should be better investigated in order to understand whether the material has really undergone a ductile transition.

Acknowledgments

In the first place I thank Prof. Hans-Rainer Trebin for having given me the possibility of writing my PhD thesis at ITAP.

With Dr. Peter Gumbsch I had useful discussions, and he has helped me with ideas and suggestions.

The discussions with Christoph Rudhart, with whom I have worked to collect part of the results contained in the last chapter, have been very lively and very important for me. He shared the room with me for a long time and he had a lot of patience with me. It has not been easy, I know, and therefore I am really grateful to him. His friendship has given a very special and precious flavour to the development of our common scientific work.

With Falko Baier, Petra Schaaff and Christof and Cristine Horn I had many nice evenings. They have been very nice friends....

Special thanks are due to:

The family Kröner. I have to thank the family Kröner for all the very beautiful evenings together. Their warm and respectful friendship has made me fill at home in a foreign country. I have learnt some Physics during these years in Germany, and thanks to their example I feel I have for sure learnt a lot about how a human being should behave with the others.

The family Schauz. There are no words to say how much I am indebted to the family Schauz for all the support they have given me. They have treated me like a son, and they will forever be my second family.

Last but not least, I have to thank Rossana, Carlo Alberto, Massimo and Fabio Brunelli for their presence in my life.

Bibliography

[1] A. Baranyani and D.J. Evans. Calculation of equilibrium entropy differences from non-equilibrium molecular dynamics simulations. *Mol. Phys.*, 72, 1991.

[2] A. Baranyani and D.J. Evans. Comments on thermodynamic integration methods for the determination of non equilibrium entropy. *Mol. Phys.*, 74, 1991.

[3] A. Kelly, W. Tyson, and A.H. Cottrell. Ductile and brittle crystals. *Philos. Mag.*, 29, 1967.

[4] A. Kobayashi, N. Ohtani, and T. Sato. Phenomenological aspects of viscoelastic crack propagation. *J. Appl. Polymer Sci.*, 1974.

[5] A.A.Griffith. *Philos. Trans. R.Soc.London Ser. A*, 221, 1920.

[6] Allen, M.P. and Tildesley, D.J. *Computer simulation of liquids*. Oxford Science Publications, 1987.

[7] H.C. Andersen. Molecular dynamics simulations at constant temperature and/or pressure. *J. Chem. Phys.*, 72, 1980.

[8] Ashcroft and Mermin. *Solid State Physics*. New York:Holt, Rinehart and Winston, 1976.

[9] B. Budiansky and J.R. Rice. *J. Appl. Mech*, 40, 1973.

[10] B. Mehlig, D.W. Heermann, and B.M. Forrest. Hybrid monte carlo method for condensed-matter systems. *Phys. Rev. B*, 45(2), 1992.

[11] B. Wolf and P. Paufler. Mechanical properties of icosahedral almnpd probed by indentation at variable temperatures. *Phys. Stat. Sol. (a)*, 172, 1999.

[12] B. Wolf, S. Baunack, and P. Paufler. Hillock growth phenomena during post-indentation annealing of quasicrystalline almnpd. *Phys. Stat. Sol. (a)*, 172, 1999.

[13] Baake, M., Kramer, P. Schlottman, M., and Zeidler. D. Planar patterns with fivefold simmetry as sections of periodic structures in 4-space. *Int.J. of Mod. Phys.B*, 4, 1990.

[14] B.Bilby and J. Eshelby. *Fracture*, chapter 1, page 99. Academic Press, 1968.

[15] B.Bilby and J. Eshelby. *Fracture*, chapter 2, page 67. Academic Press, 1968.

[16] Bendersky. Quasicrystal with one-dimensional translational simmetry and a ten-fold rotation axis. *Phys. Rev. Lett.*, 55, 1985.

[17] Berger. *Lectures on Quasicrystals*. Les editions de physique. Les Ulis, 1994. C. Electronic properties of quasicrystals experimental. Lectures on Quasicrystals.

[18] B.L. Holian, A. Voter, and R. Ravelo. Thermostatted dynamics: how to avoid the toda demon hidden in the nosé-hoover dynamics. *Phys. Rev. E*, 52, 1995.

[19] B.L. Holian, W.G. Hoower, and H.A. Posch. The origin of irriversible behavior in reversible atomistic dynamics. *Phys. Rev. Lett.*, 59, 1987.

[20] J. Bohsung. Defekte in quasikristallen. Master's thesis, Universität Stuttgart, 1987.

[21] S.J. Chang. *int J. Fract.*, 16, 1980.

[22] Cottrell and J.Rice. Slightly curved or kinked cracks. *Int. J. Fract*, 16, 1980.

[23] D. Carsten, B. Wolf, and P. Paufler. On the orientation dependence of crack-like failure formation near indentations on an icosahedral al-pd-mn quasicrystal. *Phil. Mag. A*, 75:1171–1183, 1997.

[24] D. Gratias and E. Hippert. *Lectures on quasicrystals*. Hippert and Gratias, 1994.

[25] D.J. Bacon, D.M. Barnett, and R.D. Scattergood. *Prog. Mater. Sci.*, 23, 1980.

[26] D.J. Evans and B.L. Holian. The nose-hoover thermostat. *J. Chem. Phys.*, 1985.

[27] Dubois J.M., Kang S.S, Archambault P., and Colleret B. *J. Mater. Res.*, 8, 1993.

[28] J.D. Eshelby. *Solid State Phys.*, 3, 1956.

[29] Suck J.B et al., editor. *Introduction to Quasicrystals*. Springer Verlag, 1997.

[30] D.J. Evans. Computer experiment for nonlinear thermodynamics of couette flow. *J. Chem. Phys.*, 78, 1983.

[31] L.B. Freund. *Dynamic fracture mechanics*. Cambridge university press, 1990.

[32] Ciarlet Philippe G. *Three-dimensional elasticity*. North-Holland, 1988.

[33] Martin Gaub. Struktur und eigenschaften von binären quasikristallinen parkettierungen der ebene. Master's thesis, Universität Stuttgart, 1994.

[34] J.N. Gooodier. *Fracture*, chapter 2. Academic Press, 1968.

[35] P. Gumbsch. An atomic study of brittle fracture. *J. Mater. Res.*, 10, 1995.

[36] P. Gumbsch. Brittle fracture processes modelled on the atomic scale. *Zietschrift für Metallkunde*, 1996.

[37] P. Gumbsch. Response of dynamic cracks to increasing overload. *Mat. Res. Soc. Symp. Proc.*, 1996.

[38] Herrmann H.J. and Roux S., editors. *Statistical Models for the Fracture of Disordered Media*. North-Holland, 1990.

[39] T.L. Hill. *Principles of statistical Mechanics*. Dover, 1956.

[40] H.J. Berendsen, J.P.M. Postma, W.F. Gunsteren, A. Dinola, and J.R. Haak. *J. Chem. Phys.*, 81, 1984.

[41] B.L. Holian. Entropy evolution as a guide for replacing the liouville equation. *Phys. Rev. A*, 34, 1986.

[42] B.L. Holian. Entropy of a nonequilirbium system. *Phys. Rev. A*, 33, 1986.

[43] W.G. Hoover. Canonical dynamics: Equilibrium phase space distributions. *Phys. Rev. A*, 31, 1985.

[44] I.H. Lin and R. Thomson. *Acta Metallica*, 34, 1986.

[45] G.R. Irwin. *J. Appl. Mech*, 24, 1957.

[46] Ishimasa, Nissen and Y. Fukano. New order state beetwenn crystalline and amorphous in ni-cr particles phys. *Phys Rev. Lett*, 55, 1985.

[47] J. Bohsung and H.-R. Trebin. *Defects in quasicrystals*, chapter 2, page 183. Academic PRess Inc., 1989.

[48] J. Eshelby, W. Read, and W. Schockley. *Acta Metallica*, 1, 1953.

[49] J. Fineberg, S. Gross, M. Marder, and Swinney H. Instability in dynamic fracture. *Phys. Rev. Lett.*, 1991.

[50] J. Fineberg, S. Gross, M. Marder, and Swinney H. Instability in the propagation of fast cracks. *Phys. Rev. Lett.*, 1992.

[51] C. Janot. *Quasicrystals: A primer*. Oxford Press, 1992.

[52] Janot C. and Dubois J.M. *Les quasicristaux: Matiére á paradoxes*. Les editions de physique. Les Ulis, 1997.

[53] J.Hirth and R. Wagoner. *Int. J. Solids Struct.*, 12, 1976.

[54] G. Joos. *Theoretical Physics*. Dover, 1986. Pag. 182.

[55] J.P. Hirth and J. Lothe. *Theory of dislocations*. J. Wiley and Sons, 1982.

[56] J.Rice and R. Thomson. Ductile versus brittle behaviour of crystals. *Philos. Mag*, 29, 1974.

[57] J.Sinclair. *Nucl. Metall.*, 20, 1976.

[58] K. Ravi-Chandar and W.G. Knauss. An experimental observation into dynamics fracture. *Int. J. Fracture*, 1984.

[59] K. Takahashi, K. Matsushige, and Y. Sakurada. Precise evaluation of fast fracture velocity on acrylic polymers at the slow-to-fast transition. *J. Mater. Sci.*, 19, 1984.

[60] A.I. Khinchin. *Mathematical foundations of statistical mechanics*. Dover, 1949.

[61] J.G. Kirkwood. *J. Chem. Phys.*, 3, 1935.

[62] M. Kleman. Dislocations and disvections in aperiodic crystals. *J. Phys. France*, 2, 1992.

[63] F. Krul. Molekulardynamische simulationen von rissen in ebenen quasikristallen. Master's thesis, Universität Stuttgart, 1996.

[64] B. Lawn. *Fracture of Brittle Solids*. University Press, Cambridge, 1993.

[65] Levine D. and Steinhardt P.J. Quasicrystals: a new class of ordered structures. *Phys. Rev. Lett.*, 53, 1984.

[66] I.H. Lin. *J. Mater. Sci. Lett.*, 2, 1983.

[67] A.E. Love. *Treatise on the Mathematical Theory of Elasticity*. Dover, 1927.

[68] M. Boissieu, P. Guyot, and M. Audier. *Lectures on Quasicrystals*. Les editions de physique. Les Ulis, 1994. Quasicrystals: quasicrystalline order, atomic structure and phase transitions.

[69] M. Kléman and Ch. Sommers. Dislocations in a penrose lattice. *Acta Metallica*, 39, 1991.

[70] M. Wollgarten, M. Bartsch, U. Messerschmidt, M. Feuerbacher, R. Rosenfeld, R. Beyss, and K. Urban. *Phil. Mag. Lett.*, 71:99, 1995.

[71] Marder, M. and Gross, S. *J.Mech.Phys.Solids*, 43, 1195.

[72] D.D. Mason. *Phil. Mag.*, 39, 1979.

[73] M.E. Clamp, P.G. Baker, C.J. Stirling, and A. Brass. Hybrid monte carlo: an efficient algorithm for condensed matter simulation. *J. Comp. Chem.*, 12(18):838–846, 1994.

[74] M.F. Kakkinen and C. Popelar. *Advanced fracture mechanics*. Oxford University Press, 1985.

[75] R. Mikulla. Zur dynamik von verseztungen in qiasikristallen. Master's thesis, Universität Stuttgart, 1991.

[76] R. Mikulla. *Atomistische Studien zur Versetzungsbewegung in zweidimensionalen Quasikristallen*. PhD thesis, Universität Stuttgart, 1997.

[77] Mikulla,R, Krul, F., Stadler J., Trebin, H.-R., and Gumbsch, P. Crack propagation in quasicrystals. *Phys. Rev. Lett.*, 81, 1998.

[78] M.O. Peach and J.S. Kohler. *Phys. Rev.*, 80, 1950.

[79] Muskhelishvili. *Some Basic Problems in Mathematical Theory of Elasticity*. Noordhoff, 1952.

[80] M.Watanabe and W.Reinhardt. Direct dynamical calculation of entropy and free energy by adiabatic switching. *Phys. Rev. Lett.*, 65, 1990.

[81] Nabarro Frank R. N. *Dislocations in solids*. North-Holland, 1979-1980.

[82] N. Metropolis, A.W. Rosenblut, M.N. Rosenblut, A.H. Teller, and E. Teller. Equation of state calculations by fast computing machines. *J. Chm. Phys.*, 21, 1953.

[83] S Nosé. A molecular dynamics method for simulations in the canonical ensemble. *Mol. Phys.*, 52, 1984.

[84] S. Nosé. A unified formulation of the constant temperature molecular dynamics methods. *J. Chem. Phys.*, 1984.

[85] S. Nosé. *Molecular dynamics simulations at constant temperature and pressure*, chapter 2. Kluwer academic press, 1991.

[86] P.J. Steinhardt and S. Ostlund. *The physics of quasicrystals*. World scientific Publishing, 1987.

[87] R. Thomson, C. Hsieh, and V. Rana. Lattice trapping of fracture cracks. *J. Appl. Phys.*, 42, 1971.

[88] R. Thomson and J. Sinclair. *Acta Metallica*, 30, 1982.

[89] J. Rice. *Fracture*, chapter 2. Academic Press, 1968.

[90] J.R. Rice. *J. Appl. Mech*, 35, 1968.

[91] J.R. Rice. *Mech. Fract.*, 19, 1976.

[92] S. Duane, A.D. Kennedy, B.J. Pendleton, and D. Roweth. Hybrid monte carlo. *Phys. Let. B*, 195(2):216, 1987.

[93] Schechtman D., Blech I., Gratias D., and Cahn J.W. Metallic phase with long-range orientational order and no translational symmetry. *Phys.Rev.Lett*, 53, 1984.

[94] A.N. Stroh. *Philos. Mag.*, 3, 1958.

[95] A.N. Stroh. *J. Math. Phys.*, 41, 1972.

[96] R. Thomson. Physics of fracture. *Solid state Physics*, 39, 1986.

[97] M. Toda. *J. Phys. Soc.*, J 22, 1967.

[98] W. Döll and G.W. Weidmann. Transition from slow to fast crack propagation in pmma. *J. Mater. Sci. Lett.*, 11, 1976.

[99] T. Zoglauer. Methoden zur konstruktion quasikristalliner strukturen. Master's thesis, Universität Stuttgart, 1986.

List of Figures

List of Tables